Doctoral Thesis

Thesis Title

Analysis of Friction Mechanism of Rubber under Water Lubrication and Its Application to High Grip Sports Shoes

Department of Finemechanics

Graduate School of Engineering,

TOHOKU UNIVERSITY

Toshiaki NISHI

指　導　教　員	山口 健 准教授
研究指導教員	
審　査　委　員 （○印は主査）	○堀切川 一男 教授 1　祖山 均 教授　　2　厨川 常元 教授 3　小川 和洋 教授　　4　山口 健 准教授

TOHOKU UNIVERSITY
Graduate School of Engineering

Analysis of Friction Mechanism of Rubber under Water Lubrication and Its Application to High Grip Sports Shoes

（水潤滑下におけるゴムの摩擦機構の解明と耐滑スポーツシューズへの応用）

A dissertation submitted for the degree of Doctor of Philosophy (Engineering)

Department of Finemechanics

by

Toshiaki NISHI

July 9, 2021

Analysis of Friction Mechanism of Rubber under Water Lubrication and Its Application to High-Grip Sports Shoes

Toshiaki Nishi

Abstract

This thesis describes the systematic study on the development of rubber materials with high slip resistance for shoe outer soles. The principal results of the thesis are summarized as follows:

In Chapter 1, the background and the thesis purpose are described.

Chapter 2 explains an experimental method for observing the interface between rubber and glass. To achieve the development of rubber with high slip resistance even on a wet smooth floor, contact conditions between two substrates must be determined. Using an evanescent field formed in the total reflection method, the clearance between the two substrates can be measured based on the intensity of the reflected light in the total reflection method. Considering that the real contact distribution can be determined using light interferometry, it is concluded that the distributions of real contacts and clearance can be determined using both the total reflection method and light interferometry.

Chapter 3 demonstrates the real contact formation during contact based on the observation of the interface between a rubber hemisphere and a lubricated glass plate. Many real contacts were formed during contact, and each real contact continued to expand, even after the completion of the contact process. As explained in previous studies, once a real contact with sufficient size is formed between a soft material such as rubber and the floor, the real contact can be thermodynamically expanded. This phenomenon, the dewetting effect, is explained by the fact that the total energy decreases as the real contact expands because the loss of surface free energy is larger than the increase in strain energy for rubber. The real contact area is proportional to the 4/3 power of the product of the characteristic dewetting velocity (the ratio of spreading coefficient to lubricant viscosity) and time. The same dependency of these parameters on the real contact area was experimentally confirmed: a low spreading coefficient (parameter of wettability) and lubricant viscosity led to a large real contact area. In addition, the low contacting velocity, elastic modulus, and radius of curvature (rubber with a sharper edge) delayed the completion of the contact process, promoting real contact formation.

Chapter 4 explains the real contact formation and friction behavior of the rubber hemisphere on a lubricated glass plate. In addition to the parameters discussed in Chapter 3, the lubricant flow must be considered to understand real contact formation during sliding. Here, the decrease in the sliding velocity means the increase in the duration for the dewetting effect. As expected, the decrease in the sliding velocity promoted the real contact formation during the sliding process, and the friction coefficient increased with the real contact area.

In Chapter 5, the real contact formation and friction behavior of rubber was investigated using a rubber hemisphere with a hydrogel patch and a glass plate in water. Here, the nonuniform wetting states were formed between the two components using a hydrogel patch on the rubber bottom surface. The results indicated that real contacts were formed especially around the hydrogel patch, few real contacts were formed under the hydrogel patch, and the friction coefficient increased due to the addition of the hydrogel patch. These results indicate that water between the two substrates was localized under the hydrogel patch, and real contact formation was promoted around the hydrogel patch. The theory of the dewetting effect was also developed to explain the promotion of real contact area formation for nonuniform wetting states.

In Chapter 6, air and water were studied as hydrophobic and hydrophilic materials, respectively. While water droplets were placed at the interface between a rubber hemisphere and a glass plate for an unlubricated condition (in air) by adding a water-containing hydrogel patch on the rubber surface, air bubbles were formed between them for a water-lubricated condition (in water) by molding an air pocket (100-μm pore) on the rubber surface. Both cases corresponded to nonuniform wetting states and revealed high real contact area and friction coefficient in comparison with uniform wetting states. Note that the real contacts were surrounded by a small amount of

water for both nonuniform cases. Considering the negative pressure in the water meniscus, the theory of the dewetting effect was developed, and the promotion of real contact formation was theoretically explained.

In Chapter 7, the real contact formation and friction behavior of rubber with activated carbon or sodium chloride particles were investigated on the water-covered floor. Air bubbles were supplied to the interface between the rubber and floor because activated carbon is a porous material. In contrast, the sodium chloride particle on the rubber surface easily flowed, and air pockets were formed, which also formed the nonuniform wetting state (air bubbles in water). Further, a large real contact area and high friction coefficient were confirmed for the rubber hemisphere specimens with activated carbon and sodium chloride particles in comparison with the untreated rubber. The high friction effect was confirmed for the friction of the outer soles made of rubber with activated carbon or sodium chloride particles on a water-covered smooth tile. The shoe sole was found to decrease the slipping rate during the stepping motion on a wet floor.

Chapter 8 summarizes the results and main conclusions of the thesis. In conclusion, rubber with activated carbon or sodium chloride forms air bubbles at the rubber–wet floor interface, increasing the friction coefficient and reducing the slipping risk, which is important for the safety and design of shoe soles made of rubber.

Table of contents

Chapter 1

Introduction

1.1 Background

In the 1490s, Columbus reported that there were wild natural rubber trees (*hevea brasiliensis*) in Latin America (Fig. 1.1) and that Amazon Indians used its sap (natural rubber) for balls and religious statues [1–3]. In 1775, King Joseph of Portugal started a small rubber shoe industry at the mouth of the Amazon River [1]. In 1823, Charles Macintosh found the solubility of rubber in naphtha, leading to the development of rubber industries in England, France, and the United States. However, rubber products were sticky upon heating and brittle upon cooling [1]. In 1839, Charles Goodyear reported a

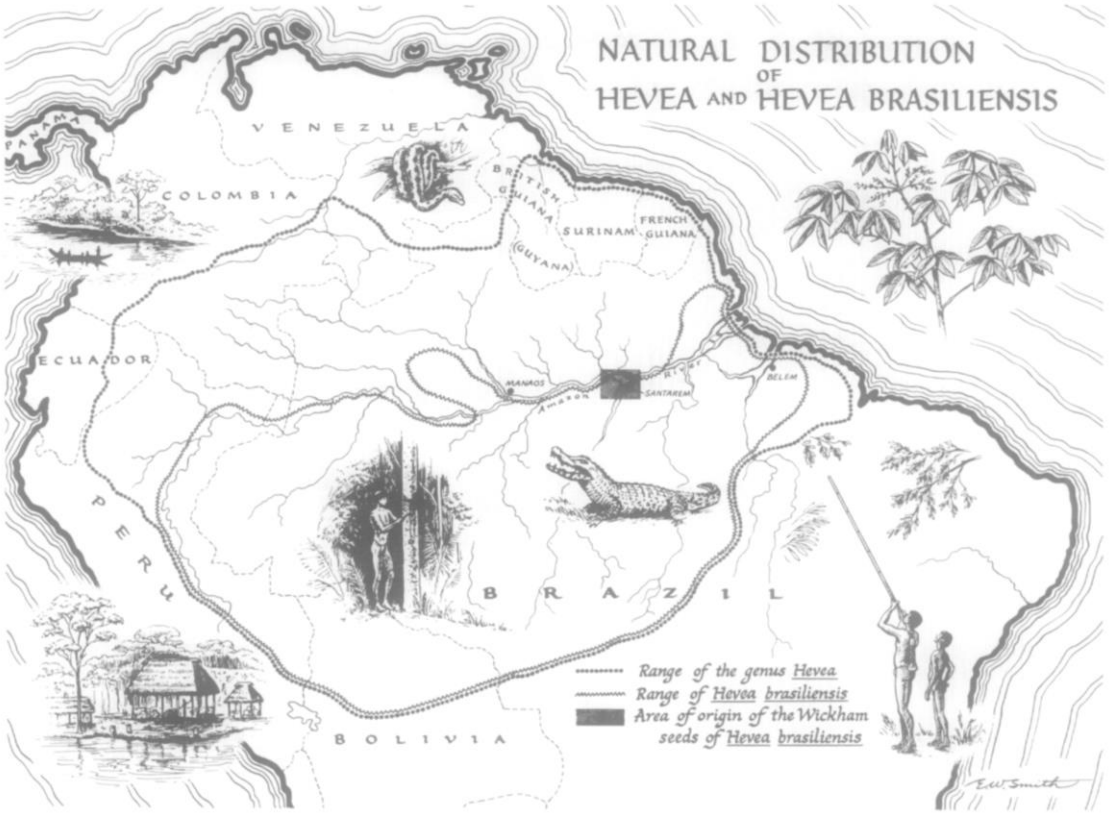

Fig. 1.1 Natural distribution of *hevea brasiliensis* in Latin America [1]

vulcanization technique in which a mixture of rubber and sulfur was heated [1–3]. Vulcanized rubber is not sticky but elastic, which improves the physical properties of rubber [1]. Based on this innovative technique, the rubber industry expanded, and rubber has been used for shoe soles, vehicle tires, rainwear, balls, and impact absorbers [1–3]. Due to the great increase in rubber use, in 1876, East India Company started to plant *hevea brasiliensis* in Southeast Asia, forming the present rubber plantation in the region [1,2]. As the demand for natural rubber increased, synthetic rubber technology was established to compensate for the shortage of natural rubber for vehicle tires in World War I and developed during World War II [4]. After the world wars, natural and synthetic rubber industries have become increasingly diverse, and the molecular structures of rubber (isoprene rubber, butadiene rubber, and styrene butadiene rubber (SBR) [2]) and additives (reinforcing filler [2,3,5–12], plasticizing agent [5,13–15], silane coupling agent [5,13,16,17], vulcanizing agent/accelerator [5,13,18–20], antioxidant [5,13,21,22], foaming agent [5,13,23], processing aid [5,13,24,25], and pigment [13]) have been eagerly studied to improve their properties.

Rubber has many applications in daily life, i.e., shoe soles, vehicle tires, floors, handgrips, and packing materials [26]. Rubber softness enables high slip resistance and sealing performance, which improves safety; for example, the slip resistance of shoe soles, especially on a wet floor, helps to prevent slip and fall accidents [27–31], while the sealing performance of the packing material used in faucets is linked to the reduction of water leaks [32]. Hence, to improve the quality of life, it is meaningful to establish a design guide for the properties of rubber, especially in the case of lubricated conditions. In this study, we mainly focused on the slip resistance of rubber outer soles.

1.2 Literature review

1.2.1 Slip resistance requirements for shoes

In daily activities such as touching, pushing, drawing, clutching, walking, running, and jumping, human movements are supported by external forces because hands and/or feet have contact with external objects: door, floor, and so on [33,34]. Since human is a bipedal animal, the interface between

the feet and floor can be very important. It has been reported that shoes have been used for 5500 years to prevent injuries from stepping on sharp stones or branches [35]. Currently, shoes are used for not only preventing incised wounds but also performing various functions, such as cushioning, stability, flexibility, slip resistance, durability, breathability, light weight, and comfort [34,36]. To optimize these properties for intended purposes (running shoes, volleyball shoes, football spikes, working shoes, and so on), shoes comprise many parts made of various polymers, as shown in Fig. 1.2 [37]. The friction and wear properties of the outer sole relate to the slip resistance and durability of shoes, respectively [34,38]. It has been reported that the fatality rate of slip and fall accidents has increased, especially with the increase in the aging population [27,39–42]. As shown in Fig. 1.3., the risks of slip and fall accidents can be high on wet floors [39]. Thus, the slip resistance of the outer sole must be accurately designed to prevent these accidents.

The friction between the outer sole and floor has been studied for decades. To prevent slip and/or fall during walking, the friction coefficient between the outer sole and floor (μ) must exceed a specific value, depending on the circumstances [43]. Grönqvist et al. tested the friction between the outer sole and floor [28] and reported that μ must be more than 0.25 for preventing fall and that the minimum range of μ to prevent slip is 0.30–0.35 [29]. Daniel et al. also reported that μ between the outer sole and floor must be more than 0.41 for walking without slip and fall [31]. In addition, the influence of

Fig. 1.2 Materials used in running shoe components [37]

the outer sole friction on running performance has been reported [44–46]. Pedroza et al. reported that the running speed in an agility maneuver increases with μ = 0.3–0.5 but remains constant at μ = 0.5–0.7 [44]. Yamaguchi studied the distribution of the friction force on the outer sole and floor during walking and reported that μ under the lateral heel and toe must be more than 0.6 to prevent slip [47].

The required value of μ for preventing slip and fall during straight walking depends on the step length, step width, and walking speed [48,49]. During walking without/with turning, as shown in Fig. 1.4, Yamaguchi et al. reported that the required value of μ between the outer sole and floor for preventing slip and fall is determined by the inclination angles of the line connecting the whole body center of mass (COM) to the center of pressure (COP) (COM–COP angle), as shown in Fig. 1.5 [48–53]. Here, the COM–COP angle relates to the body height, step length, step width, walking speed, and turning angle. The step length, step width, and walking speed can change with aging [52,53].

As explained above, it is important to increase μ, especially on the wet floor, for preventing slip and fall accidents and improving performance. Thus, tread patterns and the outer sole material have been studied [30,33]. Regarding the macroscopic design of tread patterns, the influences of direction, width, length, and depth of grooves have been studied by friction tests [54–58] and numerical simulations [59]. Fig. 1.6 shows an example of tread pattern design [57]. It has been reported that μ between the outer sole and floor can increase with the real contact area (A_r), which can be determined by the deformation of tread patterns during friction [60]. The deformation of tread patterns is

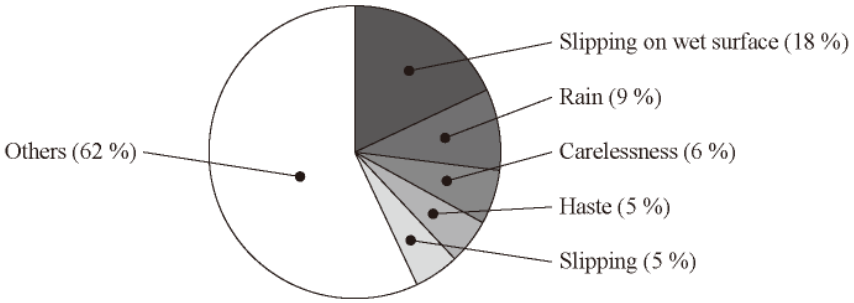

Fig. 1.3 Causes of slip and fall accidents

described as the sum of two deflection modes based on bending and deformation, as shown in Fig. 1.7 [61]. Fig. 1.7 shows that as the deflection increases, the contact area expands because the deflection by bending makes only the edge of tread contacting the floor [57,61,62]. Considering that the

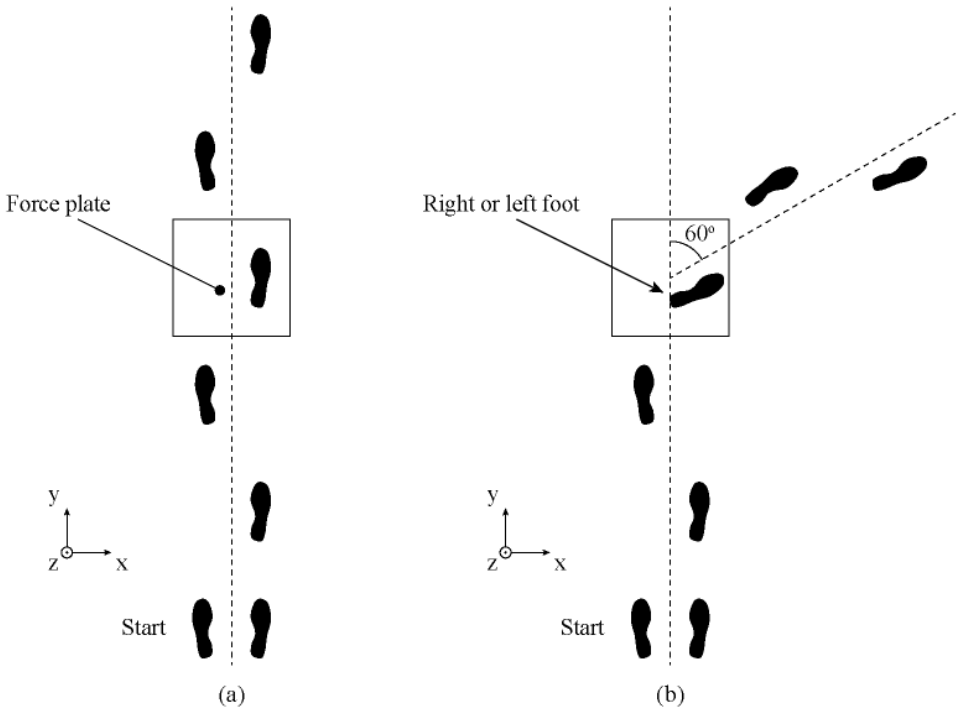

Fig. 1.4 Schematic of footprints: (a) walking along a straight line; (b) 60° turn to the right with the foot landing on the force plate [49]

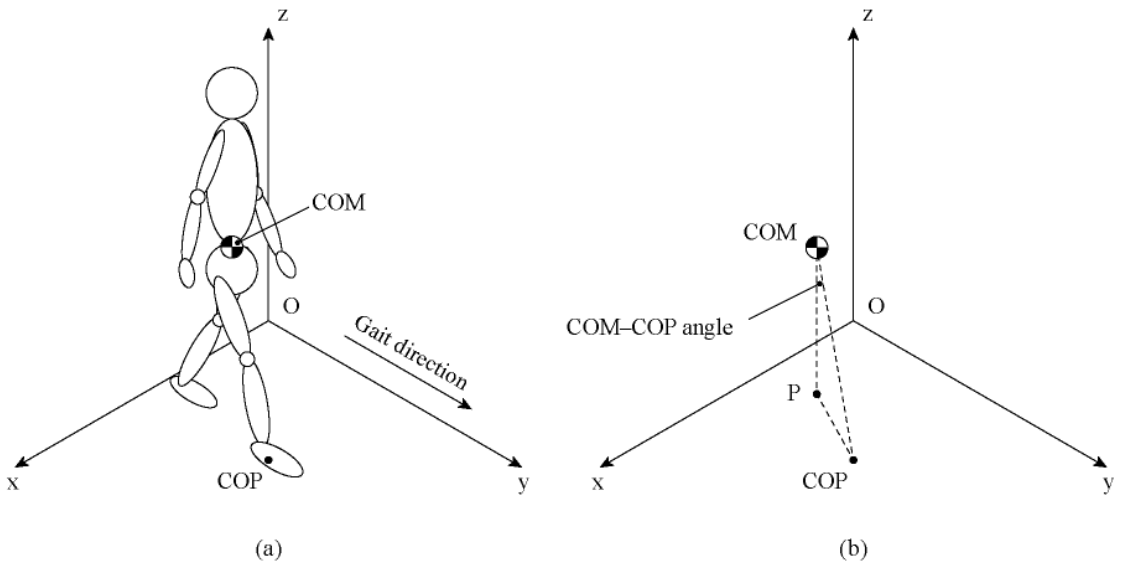

Fig. 1.5 Coordinates of COM, COP, and COM–COP angle [49]

contribution of these deflection modes is determined by the elastic modulus (E) and ratio of the width, length, and depth of grooves, it is reasonable to optimize the shape of treads/grooves [57,61,62]. As for the microscopic design of tread patterns, Yamaguchi et al. reported that μ of the outer sole on wet and icy floors can be controlled by the distribution of surface roughness, as shown in Fig. 1.8 [63–65]. It is considered that the formation of a fluid film and real contacts between two substrates can be reduced and promoted, respectively, by optimizing the distribution of surface roughness [63–65]. In many cases, the outer sole consists of rubber [33,34]; thus, designing rubber composition can also be

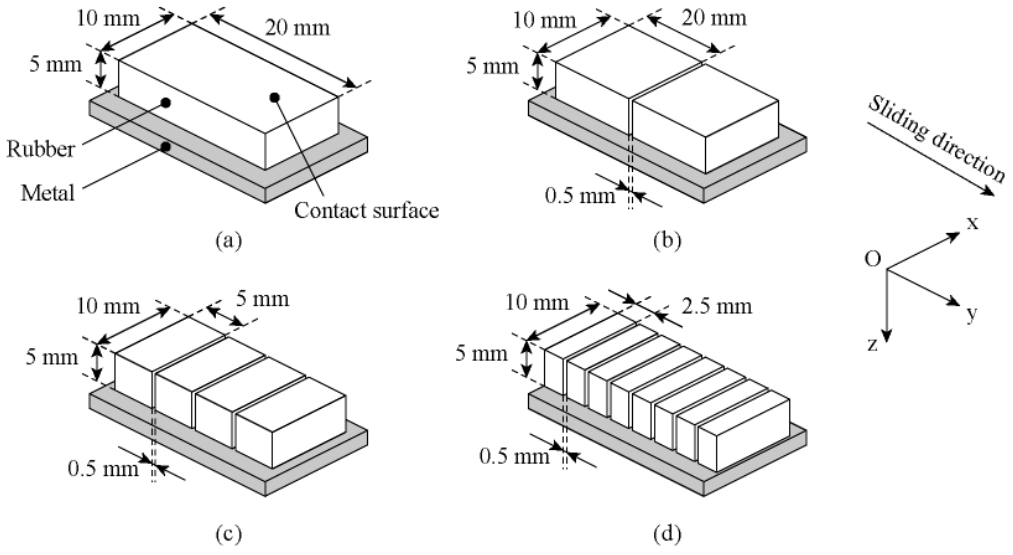

Fig. 1.6 Schematic of tread patterns' deflection [57]

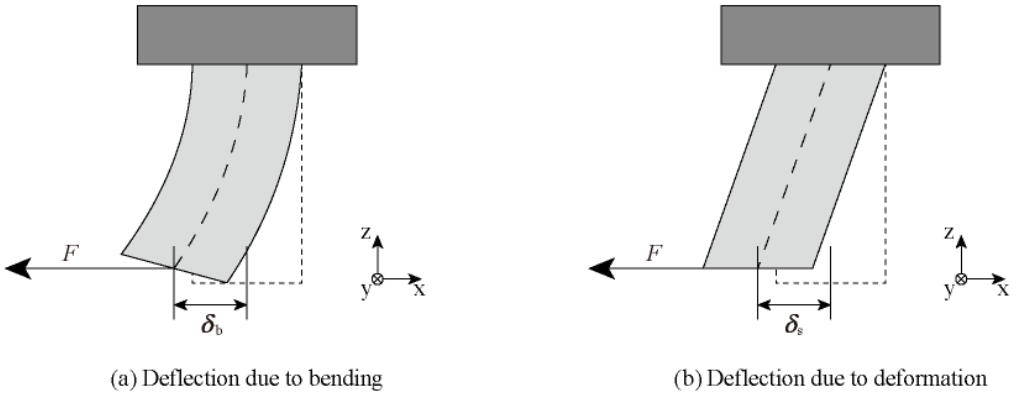

Fig. 1.7 Schematic view of tread patterns' deflection [33]

important to design the slip resistance of the outer sole.

1.2.2 Basic theory of rubber friction

In a basic theory for rubber friction, the friction force (F) is defined as the sum of F_{plow}, F_{hys}, and F_{ad}, which indicate the plowing, hysteresis, and adhesion terms, respectively [66–69]. Fig. 1.9 shows the schematic view of each term. Fig. 1.9 (a) explains that F_{plow} corresponds to the digging force, and this term can be dominant for the case of friction between the outer sole and a dirt track [70]. F_{plow} can be controlled based on the shape of tread patterns, especially based on the projected area of tread patterns. As shown in Fig. 1.9(b), rubber can be cyclically deformed by friction on asperities on the floor [69]. At the front and rear edge of the real contact, the rubber is compressed and decompressed,

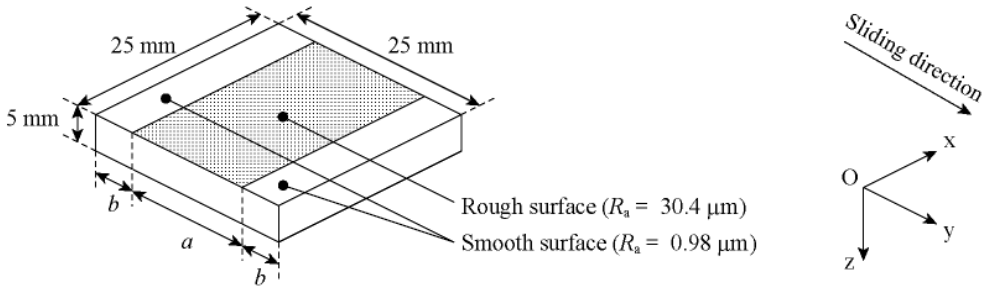

Fig. 1.8 Schematic of tread patterns with nonuniform surface roughness distribution [63]

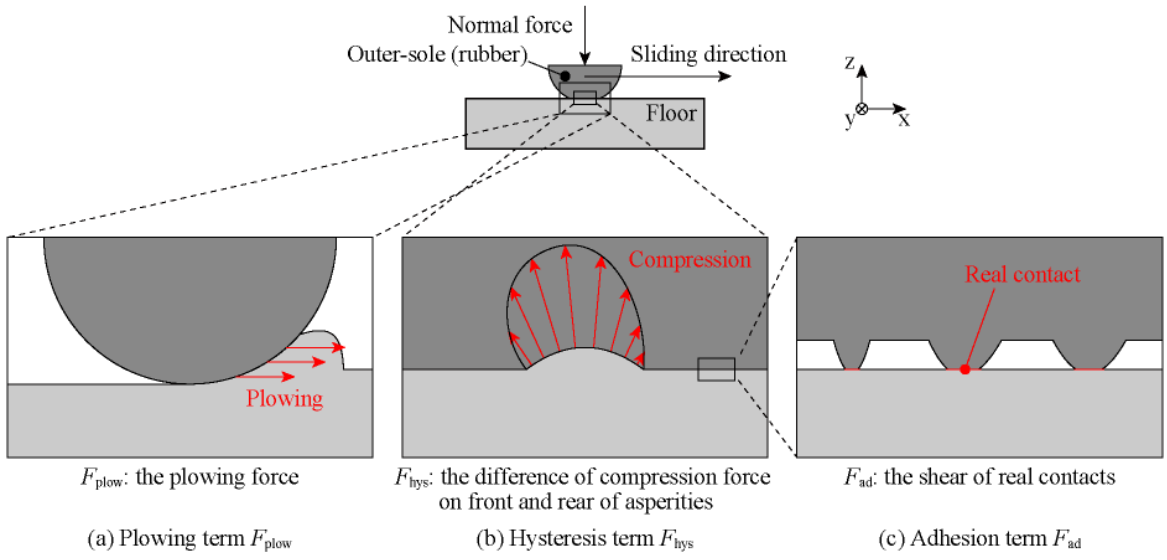

Fig. 1.9 Schematics of plowing, hysteresis, and adhesion terms

respectively [69]. Since rubber does not have perfect elasticity but viscoelasticity, the compression force is larger than the decompression force, resulting in F_{hys} [69]. As shown in Fig. 1.9(c), F_{ad} is caused by the shear of the real contact, which leads to F_{ad} being proportional to A_r [66]. Here, F_{ad} is also proportional to the shear strength [66]. Schallamach optically investigated the interface between rubber and glass during fiction, and the repetition of attachment and detachment between them, where the so-called Schallamach wave was observed [71]. Roberts reported that energy dissipation in the Schallamach wave increases or decreases shear strength depending on the spacing apart and velocity of Schallamach wave [72]. Yamaguchi et al. also investigated the relationship between energy dissipation and F_{ad} experimentally and theoretically [73–76]. In addition, Momozono et al. reported that energy dissipation can be theoretically explained based on molecular mobility [77–80].

Here, F_{plow} can be almost zero when either rubber or floor surfaces are not dug during friction, while real contacts would be formed. Regardless of lubricated or unlubricated conditions, F_{hys} contributes to F, but the value of F_{hys} can be almost zero on a smooth floor because the strain in rubber is very small. In contrast, F_{ad} can increase on the smooth floor because A_r can be large due to the small intervention of surface roughness. However, for a lubricated condition, lubricant intervention causes low A_r, leading to a small F_{ad} [70]. Therefore, it is a challenge to perform high F on a hard, smooth, and lubricated floor, such as the friction of the outer sole on a smooth and wet marble floor. In fact, the risk of slip and fall accidents on such floors is very high [39]. Considering F_{plow} and F_{hys} are almost zero in this condition, F_{ad} can dominate F, indicating that it is important to ensure large A_r to improve the slip resistance of the outer sole.

As shown in Fig. 1.10, Stribeck has reported that the lubrication condition changes from boundary lubrication to flui d lubrication with the increase of Sommerfeld numbers, $\eta v_s/P$, where η, v_s, and P indicate the lubricant viscosity, sliding velocity, and contact pressure, respectively [81,82]. The elastohydrodynamic lubrication (EHL) theory postulates that the lubricant film thickness increases with $\eta v_s/P$ for mixed and fluid lubrication and that μ drastically decreases with $\eta v_s/P$ for the mixed

lubrication and slightly increases for the fluid lubrication [83–85]. Here, μ–$\eta v_s/P$ and Stribeck curves also depend on surface roughness because the formation of real contacts can be determined by the ratio of film thickness to surface roughness [86].

1.2.3 Influence of wetting on rubber friction

In general, wetting is one of the physical properties of a liquid. Fig. 1.11 shows a typical contact angle (θ), which is used to quantify wetting [87]. θ decreases as the liquid becomes more hydrophilic and vice versa [87]. According to the Young law, the value of θ is determined by the energy balance between surface free energy and interfacial free energy around the triple line, where the liquid, solid, and air contact, as shown in Fig. 1.11, and wetting is generally described based on surface free energy and interfacial free energy [88]. The spreading coefficient (S) is also one of the parameters determined based on interfacial free energy [87]. S quantifies lubricant wettability at the triple line, and the liquid

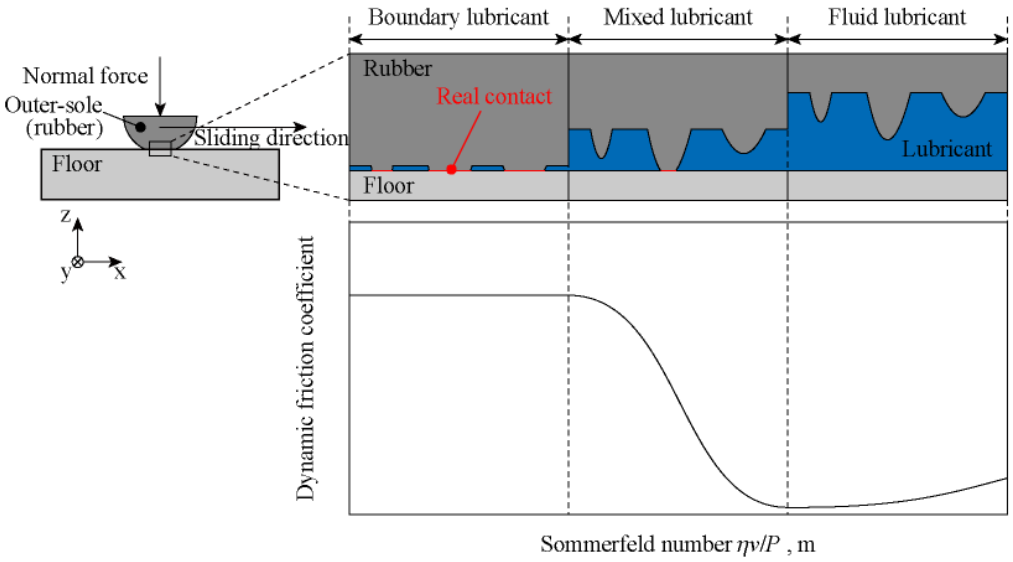

Fig. 1.10 Typical Stribeck curve and contact conditions for boundary, mixed, and fluid lubrication

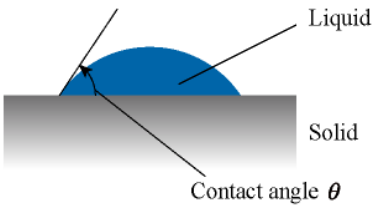

Fig. 1.11 Schematic view of the contact angle of liquid on solid [88]

tends to spread at the interface with increased S and vice versa [89]. Thus, μ and A_r in boundary and mixed lubrication change, depending on S [82,89]. The dependence of S on A_r and μ has been extensively studied [90–99]. Roberts investigated the expansion of real contact between rubber and glass [90,91] and reported that the energy balance between surface free energy and strain energy triggers this expansion [92]. This theory was developed based on the optical investigation of film thickness in a static contact between optically flat rubber and glass [93–95]. It has been reported that the dewetting effect determines the contact condition and friction behavior between rubber and glass in a sliding process [96–99]. Shibata et al. investigated the influence of S on the slip resistance of shoes, and it was confirmed that the slip resistance of shoes depends on the dewetting effect [100]. Thus, it is expected that the slip resistance of the outer sole, especially on the hard, smooth, and wet floor, can be improved by designing the wettability of rubber compounds.

By observing the interface between optically smooth rubber and glass for lubricated conditions, the dewetting theory has been developed. However, the rubber surface of the outer sole is not always optically smooth. So far, the dewetting theory has not been clarified for the friction of rubber with a rough surface. In addition, air and water are hydrophobic and hydrophilic materials, respectively. For an interface containing water droplets in air or air bubbles in water, the wetting conditions of the interface can be heterogeneous, known as nonuniform wetting. Nonuniform wetting is expected in practical situations, such as the interface between the outer sole and floor for partly lubricated conditions. Interestingly, the friction of skin on plastic bags is experimentally enlarged by adding moisture [101], and the interface gets nonuniform by adding a small amount of water. This

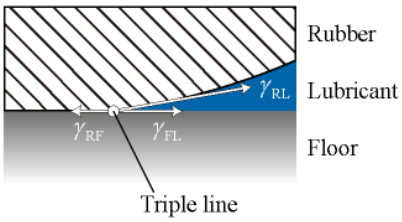

Fig. 1.12 Schematic of the triple line [88]

phenomenon indicates that the friction behavior can be sensitive to wetting distribution and that the dewetting behavior can change. However, the dewetting theory for nonuniform wetting has not been fully clarified and can be helpful to improve the slip resistance of the outer sole. Therefore, an in-depth understanding of the dewetting theory for rubber with nonuniform wetting is required.

1.3 Purpose of study

Considering that the high slip resistance of the outer sole is required and can be improved based on wetting, the purpose of this thesis was to clarify the contact and friction mechanism of rubber (including non-optically smooth rubber) with uniform and nonuniform wetting states under wet conditions and develop a rubber compound with a high grip performance for shoe soles.

1.4 Structure of the thesis

The structure of the thesis is described as follows (Fig. 1.13): Chapter 1 presents the introduction. Chapter 2 describes experimental methods for contact measurement under wet conditions. Chapters 3 and 4 describe the rubber friction with uniform wetting states, the contacting and sliding processes, respectively. Chapter 5 and 6 describe the rubber friction with nonuniform wetting states, namely rubber with hydrogel patch and rubber with an air pocket, respectively. Chapter 7 describes the friction of rubber without/with activated carbon or sodium chloride and its application to a highly slip-resistant shoe sole. Chapter 8 outlines the conclusions of this study.

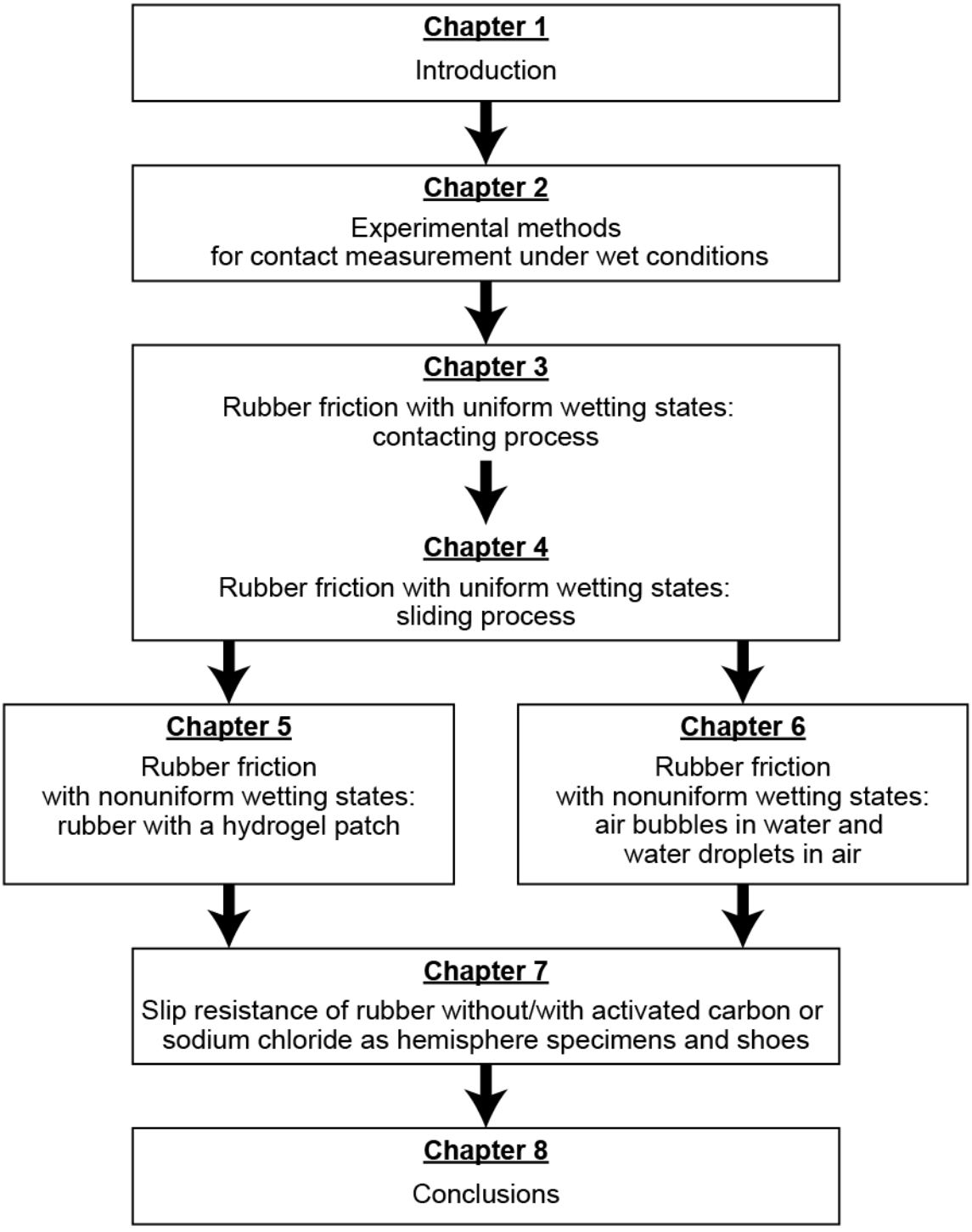

Fig. 1.13 Outline of this study

References

[1] Schultes R.E., “The Odyssey of the Cultivated Rubber Tree,” Endeavour, 1, 3, 1977, 133–8.

[2] The Society of Rubber Science and Technology Japan, “Basics of Rubber Technology,” The Society of Rubber Science and Technology Japan, 2002.

[3] Ito M., “Basics and Mechanism of Rubber,” 2009 (in Japanese).

[4] Morris P.J.T., “The American Synthetic Rubber Research Program,” University of Pennsylvania Press, 1989.

[5] The Society of Rubber Science and Technology Japan, “Rubber Industry Handbook,” Maruzen, 1949 (in Japanese).

[6] Carbon Black Association, “Carbon Black Handbook [3rd Edition],” Carbon Black Association, 1995 (in Japanese).

[7] Sone K., “Carbon Black and Tribology (Friction and Wear) Characteristics for Tires,” Journal of the Society of Rubber Science and Technology, Japan, 69, 3, 1996, 171–9 (in Japanese).

[8] Misono S., “Introduction to Carbon Black,” Journal of the Society of Rubber Science and Technology, Japan, 70, 10, 1997, 564–73 (in Japanese).

[9] Rivin D., “Surface Properties of Carbon,” Rubber Chemistry and Technology, 44, 2, 1971, 307–43.

[10] Yamamoto S., “One Trend of Short Fiber Reinforced Rubber,” Journal of the Society of Rubber Science and Technology, Japan, 60, 1, 1987, 12–8 (in Japanese).

[11] Ashida M., “Reinforcing Fiber (Short Fiber),” Journal of the Society of Rubber Science and Technology, Japan, 63, 11, 1990, 694–701 (in Japanese).

[12] Shiraki Y., “Filler Surface and Surface Modification,” Journal of the Society of Rubber Science and Technology, Japan, 65, 5, 1992, 294–303 (in Japanese).

[13] Rubber Digest Sha, “Rubber / Plastic Combination Chemicals,” Rubber Digest Sha, 2003 (in Japanese).

[14] Inoue T., “Plasticizer,” Journal of the Society of Rubber Science and Technology, Japan, 50, 10, 1977, 672–80 (in Japanese).

[15] Yamaguchi T., “Petroleum-Based Plasticizer,” Journal of the Society of Rubber Science and Technology, Japan, 50, 10, 1977, 664–71 (in Japanese).

[16] Yamashita S., “Review,” Journal of the Society of Rubber Science and Technology, Japan, 56, 3, 1983, 130–44 (in Japanese).

[17] Nagasaki H., “Modifier for Rubber,” Journal of the Society of Rubber Science and Technology, Japan, 63, 10, 1990, 646–51 (in Japanese).

[18] Yamashita S., and Kaneko T., “Crosslinker Handbook,” Taiseisha, 1981.

[19] Tachi S., “Recent Trends in Cross-Linking Agents,” Journal of the Society of Rubber Science and Technology, Japan, 63, 10, 1990, 605–15 (in Japanese).

[20] Ujikawa N., “Cross-Linking and Vulcanizing Chemicals (Peroxide Cross-Linking Agent),” Journal of the Society of Rubber Science and Technology, Japan, 63, 10, 1990, 616–24 (in Japanese).

[21] Fujiwara K., and Ueno T., “Recent Trends in Anti-Aging Agents,” Journal of the Society of Rubber Science and Technology, Japan, 63, 10, 1990, 625–38 (in Japanese).

[22] Tachi S., “Elastomer Degradation and Stabilization,” Journal of the Society of Rubber Science and Technology, Japan, 68, 5, 1995, 335–47 (in Japanese).

[23] Kudo I., “Foaming Agent,” Journal of the Society of Rubber Science and Technology, Japan, 52, 10, 1979, 614–20 (in Japanese).

[24] Suzuki T., “Processing Aid,” Journal of the Society of Rubber Science and Technology, Japan, 52, 10, 1979, 655–60 (in Japanese).

[25] Numayasu I., “Processing Aid,” Journal of the Society of Rubber Science and

Technology, Japan, 63, 11, 1990, 702–10 (in Japanese).

[26] Kubo R., “Elasticity of Vulcanized Rubber,” Shokabo, 1996 (in Japanese).

[27] Strandberg L., “The Effectof Conditions Underfoot on Falling and Overexertion Accidents,” Ergonomics, 28, 1, 1985, 131–47.

[28] Grönqvist R., Roine J., Järvinen E., and Korhonen E., “An Apparatus and a Method for Determining the Slip Resistance of Shoes and Floors by Simulation of Human Foot Motions,” Ergonomics, 32, 8, 1989, 979–95.

[29] Grönqvist R., Hirvonen M., Rajamäki E., and Matz S., “The Validity and Reliability of a Portable Slip Meter for Determining Floor Slipperiness during Simulated Heel Strike,” Accident Analysis & Prevention, 35, 2, 2003, 211–25.

[30] Perkins P.J., and Wilson Shoe M.P., “Slip Resistance Testing of Shoes- New Developments,” Ergonomics, 26, 1, 1983, 73–82.

[31] Fong D.T.-P., Hong Y., and Li J.-X., “Human Walks Carefully When the Ground Dynamic Coefficient of Friction Drops below 0.41,” Safety Science, 47, 10, 2009, 1429–33.

[32] Kuwayama K., and Kimura Y., “Tribology in Water Tap,” Toraibarojisuto/Journal of Japanese Society of Tribologists, 54, 6, 2009, 389–93 (in Japanese).

[33] Nishi T., Chapter 22: Mechanism of High Frictiona and Material Design for Sport Shoes, In “Tribology Control of Polymer Materials -Friction and Wear Mechanism/Material Design/Measurement and Evaluation Method/Development and Application Example -,” Technical Information Institute Co., Ltd., 2020. 543–550 (In Japanese)

[34] Nishi T., “Development of Volunteer Shoes for Tokyo 2020 Based on Tribology,” Toraibarojisuto/Journal of Japanese Society of Tribologists, 65, 7, 2020, 398–403 (in Japanese).

[35] Nishiwaki T., “Foot and Shoe Science,” NIkkan Kougyou Shinbunsha, 2013 (in Japanese).

[36] Nishiwaki T., “Record-Setting Running Shoes,” Journal of the Japan Society of Mechanical Engineers, 113, 1095, 2010, 101–4 (in Japanese).

[37] Moriyasu K., “Tribology in Sports Shoes,” Toraibarojisuto/Journal of Japanese Society of Tribologists, 58, 1, 2013, 17–23 (in Japanese).

[38] Nishi T., Yamaguchi T., Shibata K., and Hokkirigawa K., “Effect of the Porosity Distribution on Dry Sliding Friction and Wear of Cross-Linked Ethylene Vinyl Acetate Foams With a Skin Layer,” Biotribology, 22, February, 2020, 100128.

[39] Nishiyama Isao, “Research on Evaluation Technologies and Measures to Protect People from Accidents inside Buildings in Daily Life,” 2012 (in Japanese).

[40] Courtney T.K., Sorock G.S., Manning D.P., Collins J.W., and Holbein-Jenny M.A., “Occupational Slip, Trip, and Fall-Related Injuries--Can the Contribution of Slipperiness Be Isolated?,” Ergonomics, 44, 13, 2001, 1118–37.

[41] Koepp G.A., Snedden B.J., and Levine J.A., “Workplace Slip, Trip and Fall Injuries and Obesity,” Ergonomics, 58, 5, 2015, 674–9.

[42] Yamaguchi T., “Tribology for Safe Walking,” Toraibarojisuto/Journal of Japanese Society of Tribologists, 62, 1, 2017, 3–9 (in Japanese).

[43] Yamaguchi T., and Hokkirigawa K., “Walking-Mode Maps’ Based on Slip/Non-Slip Criteria,” Industrial Health, 46, 2008, 23–31.

[44] Pedroza A., Fernandez S., Heidt R., and Kaeding C., “Evaluation of the Shoe-Surface Interaction Using an Agility Maneuver,” Medicine and Science in Sports and Exercise, 42, 9, 2010, 1754–9.

[45] Sterzing T., Müller C., Hennig E.M., and Milani T.L., “Actual and Perceived Running Performance in Soccer Shoes: A Series of Eight Studies,” Footwear Science, 1, 1, 2009,

5–17.

[46] Thomson A., Whiteley R., Wilson M., and Bleakley C., “Six Different Football Shoes, One Playing Surface and the Weather; Assessing Variation in Shoe-Surface Traction over One Season of Elite Football,” PLoS ONE, 14, 6, 2019, 1–13.

[47] Yamaguchi T., “Distribution of the Local Required Coefficient of Friction in the Shoe–Floor Contact Area during Straight Walking: A Pilot Study,” Biotribology, 19, April, 2019.

[48] Yamaguchi T., Hatanaka S., and Hokkirigawa K., “Effect of Step Length and Walking Speed on Traction Coefficient and Slip between Shoe Sole and Walkway,” Tribology Online, 3, 2, 2008, 59–64.

[49] Yamaguchi T., Yano M., Onodera H., and Hokkirigawa K., “Kinematics of Center of Mass and Center of Pressure Predict Friction Requirement at Shoe-Floor Interface during Walking,” Gait and Posture, 38, 2, 2013, 209–14.

[50] Yamaguchi T., and Masani K., “Contribution of Center of Mass-Center of Pressure Angle Tangent to the Required Coefficient of Friction in the Sagittal Plane during Straight Walking,” Biotribology, 5, 2016, 16–22.

[51] Yamaguchi T., Suzuki A., and Hokkirigawa K., “Required Coefficient of Friction in the Anteroposterior and Mediolateral Direction during Turning at Different Walking Speeds,” PLoS ONE, 12, 6, 2017, 1–16.

[52] Yamaguchi T., Okamoto R., Hokkirigawa K., and Masani K., “Decrease in Required Coefficient of Friction Due to Smaller Lean Angle during Turning in Older Adults,” Journal of Biomechanics, 74, 2018, 163–70.

[53] Yamaguchi T., and Masani K., “Effects of Age-Related Changes in Step Length and Step Width on the Required Coefficient of Friction during Straight Walking,” Gait and Posture, 69, October 2018, 2019, 195–201.

[54] Li K.W., and Chen C.J., “The Effect of Shoe Soling Tread Groove Width on the Coefficient of Friction with Different Sole Materials, Floors, and Contaminants,” Applied Ergonomics, 35, 6, 2004, 499–507.

[55] Li K.W., and Chin J.C., “Effects of Tread Groove Orientation and Width of the Footwear Pads on Measured Friction Coefficients,” Safety Science, 43, 7, 2005, 391–405.

[56] Li K.W., Wu H.H., and Lin Y.C., “The Effect of Shoe Sole Tread Groove Depth on the Friction Coefficient with Different Tread Groove Widths, Floors and Contaminants,” Applied Ergonomics, 37, 6, 2006, 743–8.

[57] Maegawa S., Itoigawa F., and Nakamura T., “Effect of Surface Grooves on Kinetic Friction of a Rubber Slider,” Tribology International, 102, 2016, 326–32.

[58] Yamaguchi T., Katsurashima Y., and Hokkirigawa K., “Effect of Rubber Block Height and Orientation on the Coefficients of Friction against Smooth Steel Surface Lubricated with Glycerol Solution,” Tribology International, 110, December 2016, 2017, 96–102.

[59] Isobe M., Moriyasu K., and Nishiwaki T., “Application of Numerical Simulation to Sole Structure Designing for Grip Improvement,” The Proceedings of the Symposium on Sports and Human Dynamics, 2012, 251–4 (in Japanese).

[60] Sridharan K., and Sivaramakrishnan R., “Dynamic Behavior of Tyre Tread Block,” American Journal of Engineering and Applied Sciences, 5, 2 SE-Research Article, 2012.

[61] Moriyasu K., Nishiwaki T., Shibata K., Yamaguchi T., and Hokkirigawa K., “Friction Control of a Resin Foam/Rubber Laminated Block Material,” Tribology International, 136, December 2018, 2019, 548–55.

[62] Maegawa S., Itoigawa F., and Nakamura T., “A Role of Friction-Induced Torque in

Sliding Friction of Rubber Materials," Tribology International, 93, 2016, 182–9.

[63] Yamaguchi T., Umetsu T., Ishizuka Y., Kasuga K., Ito T., Ishizawa S., et al., "Development of New Footwear Sole Surface Pattern for Prevention of Slip-Related Falls," Safety Science, 50, 4, 2012, 986–94.

[64] Yamaguchi T., and Hokkirigawa K., "Development of a High Slip-Resistant Footwear Outsole Using a Hybrid Rubber Surface Pattern," Industrial Health, 52, 5, 2014, 414–23.

[65] Yamaguchi T., Hsu J., Li Y., and Maki B.E., "Efficacy of a Rubber Outsole with a Hybrid Surface Pattern for Preventing Slips on Icy Surfaces," Applied Ergonomics, 51, 2015, 9–17.

[66] Bowden F.P., and Tabor D., "The Friction and Lubrication of Solids Part II," Physics Today, 17, 6, 1964, 72.

[67] Moore D.F., "The Friction and Lubrication of Elastomers," Pergamon Press, 1972.

[68] Moore D.F., and Geyer W., "A Review of Adhesion Theories for Elastomers," Wear, 22, 2, 1972, 113–41.

[69] Moore D.F., and Geyer W., "A Review of Hysteresis Theories for Elastomers," Wear, 30, 1, 1974, 1–34.

[70] Ramsay H.T., and Senneck C.R., "Anti-Slip Studs for Safety Footwear," Applied Ergonomicsfile:///C:/Users/Nishi-to/Downloads/Anti-Slip Studs for Safety FootwearPdf, 3, 4, 1972, 219–23.

[71] Schallamach A., "How Does Rubber Slide?," Wear, 17, 4, 1971, 301–12.

[72] Roberts A.D., and Thomas A.G., "The Adhesion and Friction of Smooth Rubber Surfaces," Wear, 33, 1, 1975, 45–64.

[73] Yamaguchi T., Ohmata S., Creton C., and Doi M., "Adhesion and Sliding Friction of Sticky Materials," Toraibarojisuto/Journal of Japanese Society of Tribologists, 53, 3,

2007, 150–5 (in Japanese).

[74] Yamaguchi T., Ohmata S., and Doi M., “Regular to Chaotic Transition of Stick-Slip Motion in Sliding Friction of an Adhesive Gel-Sheet,” Journal of Physics Condensed Matter, 21, 20, 2009, 205105.

[75] Morishita M., Kobayashi M., Yamaguchi T., and Doi M., “Observation of Spatio-Temporal Structure in Stick-Slip Motion of an Adhesive Gel Sheet,” Journal of Physics Condensed Matter, 22, 36, 2010, 365104.

[76] Yamaguchi T., Morishita M., Doi M., Hori T., Sakaguchi H., and Ampuero J.P., “Gutenberg-Richter’s Law in Sliding Friction of Gels,” Journal of Geophysical Research: Solid Earth, 116, 12, 2011, B12306.

[77] Momozono S., Nakamura K., and Kyogoku K., “A Boundary Friction Model with Attachments of Molecular Chains and Interfacial Failure for Amorphous Polymers,” Toraibarojisuto/Journal of Japanese Society of Tribologists, 55, 11, 2010, 827–35 (in Japanese).

[78] Momozono S., Nakamura K., and Kyogoku K., “Theoretical Model for Adhesive Friction between Elastomers and Rough Solid Surfaces,” Journal of Chemical Physics, 132, 11, 2010, 114105.

[79] Momozono S., Takeuchi H., Iguchi Y., Nakamura K., and Kyogoku K., Dissipation characteristics of adhesive kinetic friction on amorphous polymer surfaces. Tribol. Int., vol. 48, 2012, p. 122–7.

[80] Momozono S., “Adhesion and Boundary Friction of Elastomer Surfaces,” Toraibarojisuto/Journal of Japanese Society of Tribologists, 58, 10, 2013, 734–41 (in Japanese).

[81] Stribeck R., “Die Wesentlichen Eigenschaften Der Gleit-Und Rollenlager,” Zeitschrift Des Vereines Deutscher Ingenieure, 46, 37, 1902, 1341–8.

[82] Nishi T., Moriyasu K., Harano K., and Nishiwaki T., Influence of dewettability on rubber friction properties with different surface roughness under water/ethanol/glycerol lubricated conditions. Tribol. Online, vol. 11, Japanese Society of Tribologists, 2016, p. 601–7 (in Japanese).

[83] Hamrock B.J., and Dowson D., "Isothermal Elastohydrodynamic Lubrication of Point Contacts: Part III—Fully Flooded Results," Journal of Lubrication Technology, 99, 2, 1977, 264–75.

[84] Kaneta M., "Elastohydrodynamic Lubricatoin," Toraibarojisuto/Journal of Japanese Society of Tribologists, 57, 2, 2011, 64–73.

[85] Yagi K., "Basic of Elastohydrodynamic Lubricatoin," Toraibarojisuto/Journal of Japanese Society of Tribologists, 59, 2, 2014, 68–74 (in Japanese).

[86] Jackson A., and Cameron A., "An Interferometric Study of the EHL of Rough Surfaces," A S L E Transactions, 19, 1, 1976, 50–60.

[87] de Gennes P.-G., Brochard-Wyart F., and Quéré D., Special Interfaces. Capillarity Wetting Phenom. Drops, Bubbles, Pearls, Waves, New York, NY, Springer New York, 2004, p. 215–59.

[88] Hata K., "Chemical Handbook 3rd Edition," Marubeni Corporation, 1984 (in Japanese).

[89] Nishi T., "Effects of Wettability on Tribology of Soft Matter," Toraibarojisuto/Journal of Japanese Society of Tribologists, 64, 10, 2019, 588–93 (in Japanese).

[90] Roberts A.D., "Squeeze Films between Rubber and Glass," Journal of Physics D: Applied Physics, 4, 3, 1971, 423–32.

[91] Roberts A.D., and Tabor D., "The Extrusion of Liquids between Highly Elastic Solids," Proceedings of the Royal Society of London Series A, Mathematical and Physical Sciences, 325, 1562, 1971, 323–45.

[92] Brochard-Wyart F., and De Gennes P.G., “Dewetting of a Water Film between a Solid and a Rubber,” Journal of Physics: Condensed Matter, 6, 23A, 1994, A9–12.

[93] Martin P., Silberzan P., and Brochard-Wyart F., “Sessile Droplets at a Solid/Elastomer Interface,” Langmuir, 13, 18, 1997, 4910–4.

[94] Martin P., and Brochard-Wyart F., “Dewetting at Soft Interfaces,” Physical Review Letters, 80, 15, 1998, 3296–9.

[95] Martin A., Buguin A., and Brochard-Wyart F., “Dewetting Nucleation Centers at Soft Interfaces,” Langmuir, 17, 21, 2001, 6553–9.

[96] Martin A., Clain J., Buguin A., and Brochard-Wyart F., “Wetting Transitions at Soft, Sliding Interfaces,” Physical Review E - Statistical, Nonlinear, and Soft Matter Physics, 65, 3, 2002, 031605/1-031605/4.

[97] Martin A., Buguin A., and Brochard-Wyart F., “‘Čerenkov’ Dewetting at Soft Interfaces,” Europhysics Letters, 57, 4, 2002, 604–10.

[98] Nishi T., Moriyasu K., Harano K., and Nishiwaki T., “Influence of Surface Free Energy on Rubber Friction Properties under Water/Ethanol Lubrilated Conditions,” Tribologists, 59, 11, 2014, 41–7 (in Japanese).

[99] Chudak M., Kwaks J.S., Snoeijer J.H., and Darhuber A.A., “Non-Axisymmetric Elastohydrodynamic Solid-Liquid-Solid Dewetting: Experiments and Numerical Modelling,” European Physical Journal E, 43, 1, 2020, 1–11.

[100] Shibata K., Warita I., Yamaguchi T., Hinoshita M., Sakauchi K., Matsukawa S., et al., “Effect of Groove Width and Depth and Urethane Coating on Slip Resistance of Vinyl Flooring Sheet in Glycerol Solution,” Tribiology International, 135, February, 2019, 89–95.

[101] Derler S., and Gerhardt L.C., “Tribology of Skin: Review and Analysis of Experimental Results for the Friction Coefficient of Human Skin,” Tribology Letters,

45, 1, 2012, 1–27.

Chapter 2

Experimental methods

for contact measurement under wet conditions

2.1 Introduction

Slip and fall accidents, particularly on wet surfaces, have increased in Japan [1]. The slip resistance of the outer sole of a shoe must be improved to prevent these accidents. Generally, an outer sole is composed of rubber, such as butadiene rubber and styrene butadiene rubber. Thus, the compositions of rubber and tread patterns must be considered to improve the slip resistance of the outer sole [2].

The elastohydrodynamic lubrication theory states that the friction force in lubricated conditions can be determined by the contact condition between two substrates, depending on the lubricant viscosity, sliding velocity, and mean contact pressure [3]. Rubber friction behaviors for lubricated conditions are also sensitive to the dewetting behavior, which depends on the surface free energy of rubber, floor, and lubricant [4–11].

Some in situ methods to observe the interface during friction have been reported [12–21]. In light interferometry, the film thickness of the lubricant is quantified based on interference patterns [12]. However, if the surfaces of rubber and floor are not optically flat, it is difficult to observe interference patterns, and consequently, the film thickness cannot be estimated for many cases of rubber friction due to surface roughness. In contrast, Eguchi et al. reported that the distribution of real contacts can be observed in light interferometry regardless of roughness [13–15]. In laser-induced fluorescence, the film thickness can be detected based on the fluorescent intensity of the added substance in a lubricant [16]. However, considering the influence of the fluorescent material on the surface free energy of the lubricant, laser-induced fluorescence is unsuitable for studying the wettability between the two

substrates. In the total reflection method, the scattered light on the interface corresponds to the distribution of real contacts [17–21]. Additionally, this method enables measuring contact time and frictional stress distributions during sliding between rubber and glass [20,21]. In the total reflection method, an electromagnetic field called the evanescent field is generated above the surface and does not propagate but is localized in the vicinity of the surface [22]. At a point above the surface where the reflective index is locally different, the evanescent wave can scatter. The evanescent field technique is used in nanofluidics for measuring the distance between a nanoparticle and a wall [23]. Thus, observing scattered light at the interface in the total reflection method enables one to determine the presence of the real contact area. Because the intensity of scattered light corresponds to the intensity of the evanescent field, the distribution of film thickness is also quantified based on the intensity of scattered light.

In this chapter, we aimed to establish an in situ measurement of the real contact area and film thickness based on the damping behavior of the evanescent field in the total reflection method. By preparing a wedge between polypropylene (PP) and glass plates, the intensity decay was measured by the total reflection method and compared with the clearance between two substrates measured by light interferometry.

2.2 Experimental methods

2.2.1 Evanescent field

The intensity distribution of the evanescent field above a surface is described as follows [22]:

$$I_{\mathrm{E}} = I_{\mathrm{E0}} \exp\left(-\frac{h}{d_{\mathrm{E}}} \right) \tag{1.1}$$

where I_{E}, h, and d_{E} are the energy intensity of the evanescent field, distance from the surface, and evanescent decay length, respectively, and $I_{\mathrm{E0}} = I_{\mathrm{E}}$ at h = 0 nm. Eq. (1.1) shows that the energy density of the evanescent field exponentially decreases with distance from the surface, depending on the value of d_{E}. For the total internal reflection in material (a), which faces material (b), d_{E} is determined by the

incident angle (θ), wavelength (λ), and reflection index [22]:

$$d_{\mathrm{E}} = \frac{\lambda}{4\pi n_{\mathrm{a}}}\left(\sin^2\theta - \frac{{n_{\mathrm{b}}}^2}{{n_{\mathrm{a}}}^2}\right)^{-0.5} \tag{1.2}$$

where n_{a} and n_{b} are the reflection indices of materials (a) and (b), respectively.

2.2.2 Light interferometry

The measured interference patterns in light interferometry can be used to quantify the clearance between two substrates, and the following equation explains the relationship between the intensity of interference patterns and clearance [24]:

$$I_{\mathrm{L}} = I_{\mathrm{L1}} + I_{\mathrm{L2}} + 2\sqrt{I_{\mathrm{L1}} I_{\mathrm{L2}}}\exp\left(-Knh^m\right)\cos\left(\frac{4\pi h}{\lambda} + \phi\right) \tag{1.3}$$

where I_{L} is the interference pattern intensity, I_{L1} and I_{L2} are light intensities reflected on the surfaces of two substrates, and n and ϕ are the reflection index and phase difference between the light reflected on the surfaces of two substrates. K and m indicate constant values, which correspond to coherence and the damping of light. These parameters were determined by fitting experimental and theoretical intensities of interference patterns on each condition in the least-squares method.

2.2.3 Experimental apparatus

To investigate the relationship between the measured intensity in the total reflection method and clearance, the contact conditions of the wedge between the PP (J-3021GR, Prime Polymer Co., Ltd.) plate and glass (BK7) prism (084.4L100-45DEG-6P-4SH3.5, SIGMAKOKI Co., Ltd.) in air and water (ion-exchanged with a demineralizer (REP343RB, Toyo Seisakusyo, Ltd.)) were observed by the total reflection method and light interferometry. Fig. 2.1 indicates an overview of the experimental system. A plastic wrap sheet (SW-3040, CAINZ Corporation) was set between the prism surface and the edge of the PP plate. A normal force of 0.98 N was loaded on the edge of the PP plate to generate

contact between the PP plate and prism. In the total reflection method, to ensure the total internal reflection on the surface of the prism internally, light was penetrated from a light-emitting diode (LED) through the light guide (LE-OPT-24, OPTEC FA Co., Ltd.). The charge-coupled device (CCD) camera (AT-030MCL, JAI Ltd.) was used to observe the light scattered at the interface between the PP plate and the prism. The pixel format and pixel size were 12 bit and 3.6 × 3.6 μm^2, respectively. In light interferometry, the light was also penetrated from another LED light source to the interface between the PP plate and the prism through the telecentric lens (TV-2F-110, OPTART Co., Ltd.). By using the same camera, the light reflected at the PP plate–prism interface was observed. Here air or water was present in the space between the PP plate and prism. Table 2.1 shows that the refractive indices of air and water are smaller than those of the substrates [25,26], indicating that $\phi = \pi$ in Eq. (1.3). Table 2.2 shows the list of experimental conditions (lubrication condition, wavelengths in the total reflection method and light interferometry, incident angle, and evanescent decay length). Here, different wavelengths were selected in the total reflection method and light interferometry to distinguish light in each method. In detail, blue (λ = 465 nm), green (λ = 520 nm), and red (λ = 645 nm) LEDs (HLV2-22BL-3W, HLV2-22GR-3W, and HLV2-22RD-3W, CCS Inc.) were used. To

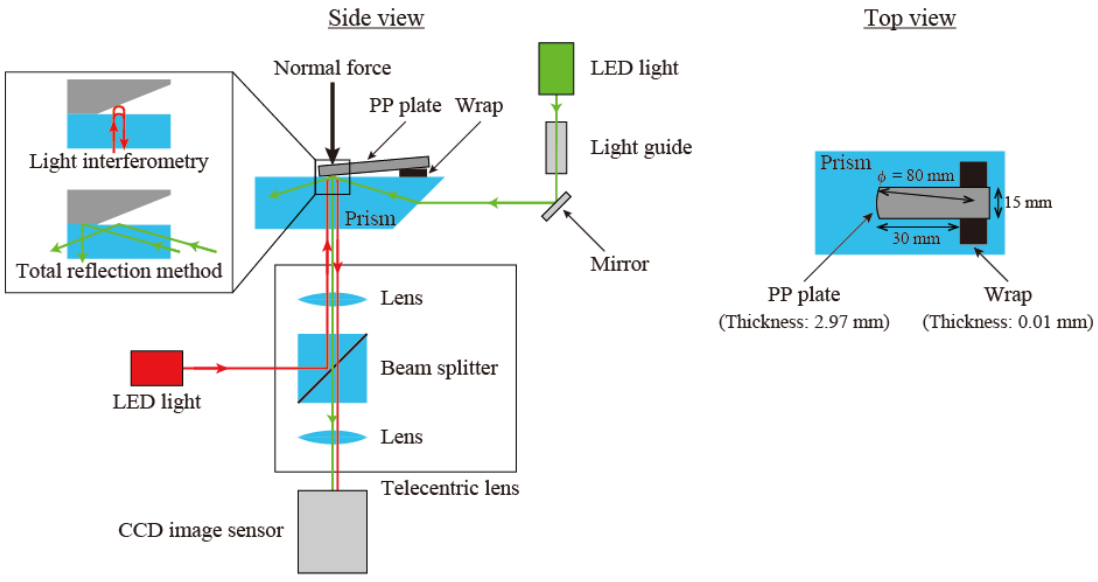

Fig. 2.1 Schematic of the experimental setup [27]

ensure total internal reflection, the incident angle above the critical angles, 41.2° and 61.5°, was used for air and water, respectively. The atmospheric temperature and humidity were controlled at 23.5°C and 75% RH, respectively. To ensure that light did not transmit through the PP plate, titanium oxide (A150, Sakai Chemical Industry Co., Ltd.) was added to PP at 10 vol.% by the rotating twin-screw extruder (KZW20TW-45MG-NH, TECHNOVEL Corporation) at 200°C. The surface roughness and elastic modulus of the PP plate were measured by a one-shot 3D-measuring macroscope (VR3000, Keyence Corporation) and a dynamic viscoelastic measurement device (Reogel E4000, UBM Co., Ltd.), respectively. The arithmetical mean height (S_a) and elastic modulus of the PP plate were 0.17 μm and 1.34 GPa, respectively.

2.2.4 Elimination of the influence of incident light distributions

Both in the total reflection method and light interferometry, the intensity of the penetrated light was high at the center of the interface in comparison with that at the edge, indicating that the penetrated light was not in-plane uniform. In this study, this nonuniformity was offset by defining the intensities (I) in the total reflection method and light interferometry based on Eq. 1.4 [15]:

$$I = I_{\mathrm{O}} \frac{\bar{I}_{\mathrm{I}}}{I_{\mathrm{I}}} \tag{1.4}$$

where I_{O} and I_{I} are the measured intensity and incident light intensity in each pixel, respectively, and $\bar{I}_{\mathrm{I}}$ is the mean value of I_{I}. The value of I_{I} in the total reflection method corresponds to the intensity on the real contact area, thus, was experimentally defined as the observed intensity when the observation field was occupied with real contact. To ensure a large contact area, soft and flat silicone rubber was placed to face the prism surface in the unlubricated condition, and titanium oxide (A150, Sakai Chemical Industry Co., Ltd.) was blended with the silicone rubber (Sylgard 184, Dow Corning Toray Co., Ltd.) at 10 vol.% to ensure that the incident light scattered at the interface. S_a and elastic modulus of the rubber were 0.15 μm and 1.74 MPa, respectively, measured as for the PP plate. For light interferometry, the distribution of I_{I} was determined by observing the air–prism interface.

2.3 Results

2.3.1 Relationship between the measured intensity in the total reflection method and clearance

In Fig. 2.2, the observed images and distributions of measured intensity in the total reflection method and light interferometry in condition (iii) are shown. The graphs under the measured intensity images indicate the distribution of I along the white lines in the images above. Focusing on the range

Table 2.1 Refractive indices related to the experimental system in this study

	Refractive index
Polypropylene [25]	1.4707-1.5245
Titanium oxide [26]	2.616
Air [26]	1.000
Water [26]	1.333
Glass (BK7) [26]	1.517

Table 2.2 Experimental conditions

Condition	Lubricant Condition	Wavelength in the total reflection method, nm	Wavelength in light interferometry, nm	Incident angle, deg.	Evanescent decay length, nm
(i)	Dry	465	645	65	39
(ii)	Dry	520	645	60	49
(iii)	Dry	520	645	65	44
(iv)	Dry	520	645	70	41
(v)	Dry	645	465	65	54
(vi)	Wet	520	645	65	123
(vii)	Wet	645	465	65	152

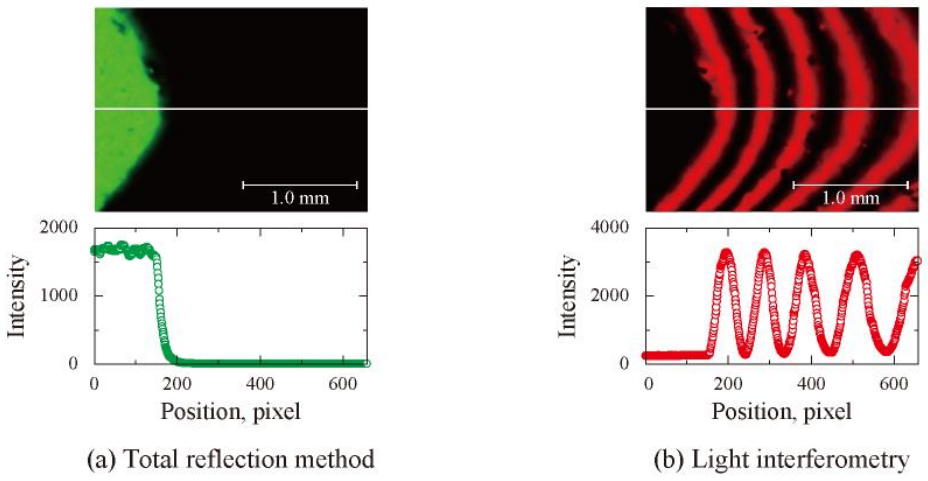

Fig. 2.2 Observed images and intensity distributions along the white lines at the interface between the PP plate and the prism under condition (iii) [27]

between 0 and 152 pixels, the intensity in the total reflection method (I_T) was high, and any interference patterns were not confirmed in light interferometry. Meanwhile, from 153 pixels, I_T drastically decreased, and interference patterns appeared in light interferometry. These results show the presence of real contact between the PP plate and the prism at 0–152 pixels and that the clearance between them increased toward the right side. Fig. 2.3 shows the clearance distribution calculated from interference patterns, supporting that the PP plate contacted the prism surface within 0–152 pixels and that the clearance increased from 153 to 659 pixels.

2.3.2 Influence of incident angle, wavelength, and lubrication condition on the measured intensity in the total reflection method

Fig. 2.4 shows I_T versus clearance calculated based on light interferometry for conditions (i–vi). Here, the value of I_T at h = 0 nm corresponds to I on the real contact area. Fig. 2.4(a) indicates that I on the real contact area decreased with the incident angle. The incident light per unit area decreased with the incident angle at the interface between two substrates. At h > 0 nm, I_T exponentially decreased with clearance, and I saturated to the constant values, which are considered as the dark current in the CCD. These results confirmed that the incident light scattered on the PP plate surface even if there was not a real contact between the PP plate and prism and that I_T decreased with clearance. Then, focusing on I_T was higher than 10 in Fig. 2.4(a), the decreasing rate of I increased

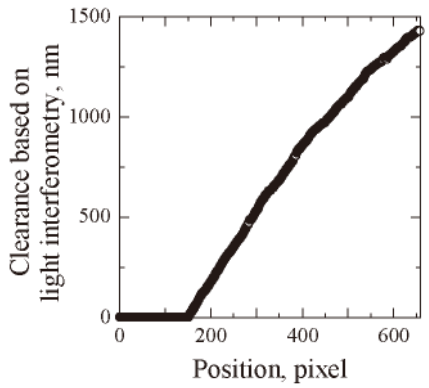

Fig. 2.3 Distribution of clearance based on light interferometry on the white line in Fig. 2.2 [27]

with the incident angle. Additionally, judging from Figs. 2.4(b, c), this rate decreased with wavelength and drastically changed due to lubrication conditions. Note that the dependence of the decay behavior of I_T on the incident angle, wavelength, and reflection index is similar to that of the evanescent field.

2.4 Discussion

2.4.1 Damping behavior of the measured intensity with clearance in the total reflection method

As shown in Fig. 2.5, the incident light in the total reflection method scattered on not only the real contact area but also on the noncontact area, indicating that I_T would depend on the evanescent wave above the PP plate surface. Fig. 2.4 shows that I_T exponentially decreased with clearance at $I >$ 10. Note that the intensity of the evanescent field is also sensitive to clearance, as explained in Eq. (1.1). To compare the exponential decay of I_T and the evanescent field, the relationship between I_T and

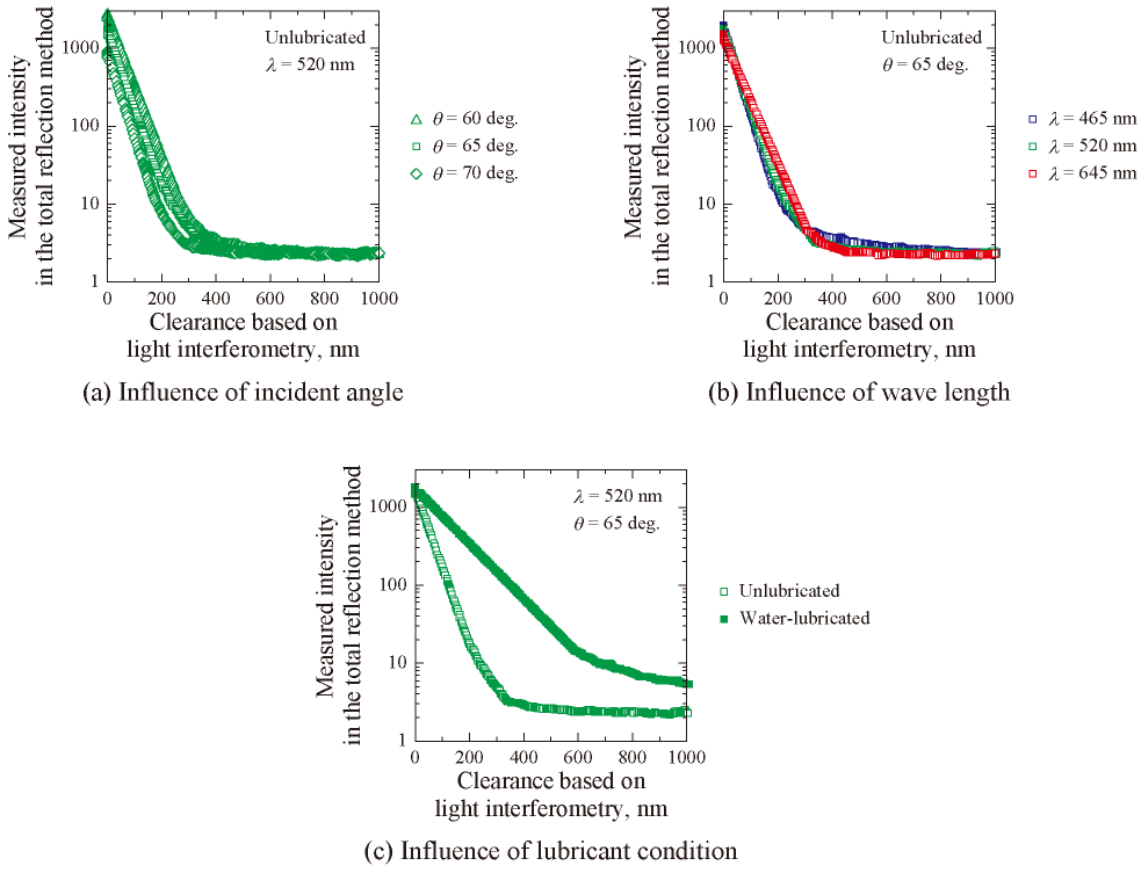

Fig. 2.4 Relationships between measured intensity in the total reflection method and clearance based on light interferometry under conditions (i–vi) [27]

clearance was investigated based on Eq. (1.5):

$$I_T = I_{T0} \exp\left(-\frac{h}{d_T}\right) \tag{1.5}$$

where I_{T0} and d_T are the value of I_T on the real contact area and the decay length of I_T, respectively. In this chapter, I_{T0} was defined as the mean value of I_T on the real contact area. Whether there was a real contact or not was determined by light interferometry [15]. To eliminate the influence of the dark current, the investigated range of I_T was limited to $I_T > 10$.

Fig. 2.6 shows the relationship between d_T and d_E for conditions (i–vii). In each condition, the value of d_T was calculated by Eq. (1.5) using the least-squares method. The results confirmed that d_T was equivalent to d_E, regardless of the incident angle, wavelength, and lubrication condition. This result explains that the negative correlation between I_T and h corresponded to the relationship between

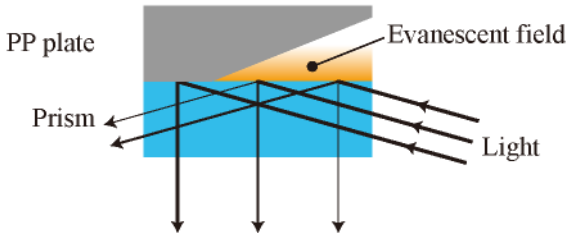

Fig. 2.5 Schematic of total internal reflection in the experimental system [27]

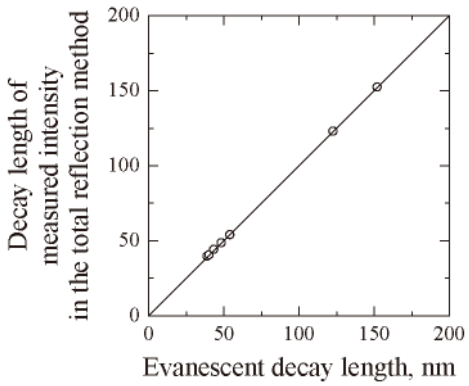

Fig. 2.6 Comparison between the damping behavior of measured intensity in the total reflection method and the evanescent field under conditions (i–vii) [27]

I_E and h; in other words, I_T was proportional to I_E.

2.4.2 Measurement of the distribution of the real contact area and film thickness

Given Eq. (1.5) and $d_T = d_E$, h can be calculated as follows:

$$h = d_E \ln \frac{I_{T0}}{I_T} \tag{1.6}$$

This equation explains that h is calculated from d_E and the ratio of I_{T0} to I_T, indicating that the measurement range of h depends on these parameters. Thus, to maximize the measurement range of h, the value of d_E and I_{T0} should be maximized. Eq. (1.2) explains that d_E decreases with the incident angle and increases with the wavelength and reflection index difference between two substrates. Additionally, as mentioned in Chapter 2.3.2, I_{T0} decreases with the incident angle. Therefore, based on the critical angle, the measured clearance range in condition (vii) was the widest in this chapter.

Fig. 2. 7 shows the relationship between h values measured based on the total reflection method and light interferometry in condition (vii). Using Eq. (1.6), the value of h was calculated from I_T. The values of h based on the total reflection method and light interferometry had a good agreement within h = 0–800 nm, which explains that real contact distributions and clearance can be measured within h = 0–800 nm and that Eq. (1.6) is not useless at h > 800 nm because of the dark current. This relationship

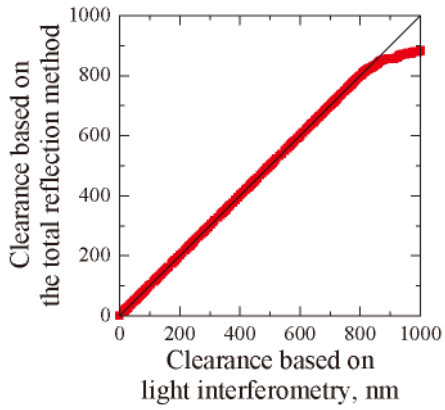

Fig. 2.7 Relationship between clearances based on the total reflection method and light interferometry under condition (vii)

also indicates that the accuracy of the clearance within h = 0–800 nm was less than 1 nm.

2.5 Conclusions

Real contact and film thickness distributions between two substrates can be measured based on the damping behavior of the evanescent field in the total reflection method. This method is useful to study rubber friction for designing outer soles with high slip resistance. Here, the measured intensity in the total reflection method is a mean value over one pixel, as well as the light interferometry and laser-induced fluorescence. If the surface of rubber or floor has asperity smaller than one pixel, the measured intensity would depend on roughness. Thus, to apply this method to estimate the clearance between two substrates, the horizontal scale of roughness must be larger than one pixel. Nevertheless, the above experimental results lead to the following conclusions:

1) In the total reflection method, the scattered light on the interface between the PP plate and prism is observed on not only the real contact area but also the noncontact area.
2) The intensity measured by the total reflection method was proportional to the intensity of the evanescent field.
3) Real contact and film thickness distributions between two substrates in a water-lubricated condition can be measured based on the damping behavior of the evanescent field in the total reflection method with an accuracy of 1 nm in the clearance range less than 800 nm.

References

[1] Nishiyama I., “Research on Evaluation Technologies and Measures to Protect People from Accidents inside Buildings in Daily Life,” 2012 (in Japanese).

[2] Moriyasu K., “Tribology in Sports Shoes,” Toraibarojisuto/Journal of Japanese Society of Tribologists, 58, 1, 2013, 17–23 (in Japanese).

[3] Stribeck R., “Die Wesentlichen Eigenschaften Der Gleit-Und Rollenlager,” Zeitschrift Des Vereines Deutscher Ingenieure, 46, 37, 1902, 1341–8.

[4] Roberts A.D., “Squeeze Films between Rubber and Glass,” Journal of Physics D: Applied Physics, 4, 3, 1971, 423–32.

[5] Brochard-Wyart F., and De Gennes P.G., “Dewetting of a Water Film between a Solid and a Rubber,” Journal of Physics: Condensed Matter, 6, 23A, 1994, A9–12.

[6] Martin P., Silberzan P., and Brochard-Wyart F., “Sessile Droplets at a Solid/Elastomer Interface,” Langmuir, 13, 18, 1997, 4910–4.

[7] Martin P., and Brochard-Wyart F., “Dewetting at Soft Interfaces,” Physical Review Letters, 80, 15, 1998, 3296–9.

[8] Martin A., Buguin A., and Brochard-Wyart F., “Dewetting Nucleation Centers at Soft Interfaces,” Langmuir, 17, 21, 2001, 6553–9.

[9] Martin A., Clain J., Buguin A., and Brochard-Wyart F., “Wetting Transitions at Soft, Sliding Interfaces,” Physical Review E - Statistical, Nonlinear, and Soft Matter Physics, 65, 3, 2002, 031605/1-031605/4.

[10] Nishi T., Moriyasu K., Harano K., and Nishiwaki T., “Influence of Surface Free Energy on Rubber Friction Properties under Water/Ethanol Lubrilated Conditions,” Toraibarojisuto/Journal of Japanese Society of Tribologists, 59, 11, 2014, 717–23 (in Japanese).

[11] Nishi T., Moriyasu K., Harano K., and Nishiwaki T., Influence of dewettability on

rubber friction properties with different surface roughness under water/ethanol/glycerol lubricated conditions. Tribol. Online, vol. 11, Japanese Society of Tribologists, 2016, p. 601–7 (in Japanese).

[12] Spikes H.A., and Cann P.M., "The Development and Application of the Spacer Layer Imaging Method for Measuring Lubricant Film Thickness," Proceedings of the Institution of Mechanical Engineers, Part J: Journal of Engineering Tribology, 2001.

[13] Eguchi M., Shibamiya T., and Yamamoto T., "Measurement of Real Contact Area and Analysis of Stick/Slip Region," Tribology International, 42, 11–12, 2009, 1781–91.

[14] Eguchi M., "Statistical Measurement of Real Contact Area on the Basis of Image Intensity Histograms (Part 1) -Using Gaussian Distribution of Light Interference Image-," Toraibarojisuto/Journal of Japanese Society of Tribologists, 57, 5, 2012, 345–52 (in Japanese).

[15] Eguchi M., Hirayanagi T., and Miyoshi T., "Statistical Measurement of Real Contact Area on the Basis of Image Intensity Histograms (Part 2) -Application to Paper-Based Wet Friction Materials-," Toraibarojisuto/Journal of Japanese Society of Tribologists, 57, 5, 2012, 353–60 (in Japanese).

[16] Tango W.J., Link J.K., Zare R.N., and LrNK J.K., "Spectroscopy of K2 Using Laser-Induced Fluorescence," The Journal of Chemical Physics, 49, 10, 1968.

[17] Schallamach A., "How Does Rubber Slide?," Wear, 17, 4, 1971, 301–12.

[18] Rubinstein S.M., Cohen G., and Fineberg J., "Detachment Fronts and the Onset of Dynamic Friction," Nature, 430, 7003, 2004, 1005–9.

[19] Maegawa S., Suzuki A., and Nakano K., "Precursors of Global Slip in a Longitudinal Line Contact under Non-Uniform Normal Loading," Tribology Letters, 38, 3, 2010, 313–23.

[20] Morishita M., Kobayashi M., Yamaguchi T., and Doi M., "Observation of

Spatio-Temporal Structure in Stick-Slip Motion of an Adhesive Gel Sheet," Journal of Physics Condensed Matter, 22, 36, 2010, 365104.

[21] Yamaguchi T., Sawae Y., and Rubinstein S.M., "Effects of Loading Angles on Stick–Slip Dynamics of Soft Sliders," Extreme Mechanics Letters, 2016.

[22] Axelrod D., Burghardt T.P., and Thompson N.L., "Total Internal Reflection Fluorescence," Annual Review of Biophysics and Bioengineering, 13, 1, 1984, 247–68.

[23] Bouzigues C.I., Tabeling P., and Bocquet L., "Nanofluidics in the Debye Layer at Hydrophilic and Hydrophobic Surfaces," Physical Review Letters, 2008.

[24] Sandoz P., and Tribillon G., "Profilometry by Zero-Order Interference Fringe Identification," Journal of Modern Optics, 1993.

[25] Samuels R.J., "Application of Refractive Index Measurements to Polymer Analysis," Journal of Applied Polymer Science, 1981.

[26] Hata K., "Chemical Handbook 3rd Edition," Marubeni Corporation, 1984 (in Japanese).

[27] Nishi T., Moriyasu K., and Nishiwaki T., "Precise Measurement of Clearance between Two Substrates Using Evanescent Waves," Tribology Online, 12, 5, 2017, 251–6.

Chapter 3

Rubber friction with uniform wetting states: contacting process

3.1 Introduction

Tribology of soft materials such as rubber is of great interest for not only industrial applications but also academic research. Rubber is a useful material to improve grip and sealing properties, which are caused by contact between two substrates. Rubber friction has been extensively studied, and contact theories have been developed, such as Schallamach waves [1–5]. Many contact theories have been reported to explain real contact deformation, especially under unlubricated conditions, such as the Hertz contact theory, the Johnson–Kendall–Roberts (JKR) theory [6], and the Greenwood–Williamson model [7]. Bowden and Tabor [8] reported that the friction force is proportional to the real contact area (A_r). A_r can be decreased due to lubricant intervention, which leads to a decrease in grip properties. Thus, it is essential to control A_r by considering lubricant intervention for practical applications, such as in shoes and vehicle tires, via material and structural design.

In material design, the lubricant between the rubber and floor can be eliminated by dewetting [9–18]. In a contact process, A_r increases with dewetting velocity, which is determined by surface free energy (γ) and lubricant viscosity (η) [9–14]. Additionally, in a sliding process (friction), A_r and the friction coefficient (μ) increase with dewetting velocity [15–18]. Therefore, A_r can be controlled by optimizing γ and η.

In contrast, in structural design, designing the tread patterns of outer soles and vehicle tires is required. The tread groove depth and width [19–22], tread groove orientation [21–23], number of grooves [24], and surface roughness of the groove [24,25] can increase μ. In the Hertz contact theory

[26], the contact area between rubber and floor is calculated from the radius of curvature (R) and elastic modulus (E). However, lubricant intervention between two substrates was not considered in the above studies. Experimentally, tread edge structure is important to break the lubricant film and make real contact in a lubricated condition, which is related to the dewetting behavior. Here, the relationships among real contact formation, dewetting behavior, and rubber edge properties (R and E) have not been clarified. Additionally, real contact formation could be affected by the contact velocity (v_c) since it determines the contact time between them.

In this chapter, we investigated the influence of dewetting velocity (γ and η) and rubber edge properties (R and E) on real contact formation between a rubber hemisphere and glass prism under lubricated conditions. The time dependencies of the real contact distribution and lubricant film thickness between the rubber and glass were experimentally investigated.

3.2 Materials and methods

3.2.1 Sample preparation

To investigate the influences of wettability and η on A_r, five types of lubricants with different γ and η were prepared. γ and η were controlled by changing the ratio of mixtures of water deionized with a demineralizer (REP343RB, Toyo Seisakusyo, Ltd., Japan), ethanol (Wako 1st grade, Wako Pure Chemical Industries, Ltd., Japan), and glycerol (Wako 1st grade, Wako Pure Chemical Industries, Ltd., Japan), as shown in Table 3.1. The surface free energies of the lubricants were measured based on the pendant drop method [27] and the Kaelble–Uy theory [28], as explained in a previous study [18]. The refractive indices and viscosities of the lubricants were measured with a refractometer (NAR-1T SOLID, ATAGO Co., Ltd., Japan) and Ostwald viscometer (2370-03-10, Climbing Co., Ltd., Japan), respectively.

To clarify the influences of R and E on real contact formation, hemispheres of silicon rubber (Sylgard 184, Dow Corning Toray Co., Ltd., Japan) with different R and E were prepared, as shown in Table 3.2. Titanium oxide (A150, Sakai Chemical Industry Co., Ltd., Japan) was added to silicon at 10

vol.% to ensure that light was reflected in a total reflection method, as explained in a previous study [29]. Three types of concave lenses (TS-0250S, Sugitoh Co., Ltd., Japan, S-SLB-10-15N, SIGMAKOKI Co., Ltd., Japan, and SLB-10-20N, SIGMA- KOKI Co., Ltd., Japan) were used to mold the rubber to control *R*. *E* was changed by changing the ratio of the cross-linking agent (5.0, 10.0, and 20.0 wt.%) to the silicon rubber. Table 3.2 shows that there was no difference in surface roughness and surface free energy between the rubbers. *E* was quantified by a dynamic viscoelastic measurement device (Reogel E4000, UBM Co., Ltd., Japan). To measure *R* and surface roughness, a One-Shot 3D measuring macroscope (VR3000, Keyence Corporation, Japan) was used. As the index of surface roughness, arithmetical mean height (S_a) was calculated from 0.100 mm^2 rubber surface where real contact was formed. The effect of *R* on S_a was eliminated by the plane correction of the measured rubber surface using an accompanying software (VR-H1A, Keyence Corporation, Japan). To calculate surface free energy based on the Kaelble–Uy theory [28], the contact angles of ion-exchanged water and diiodomethane (Wako 1st grade, Wako Pure Chemical Industries, Ltd.) were measured by a contact angle meter (DMs-401, Kyowa Interface Science Co., Ltd., Japan).

Table 3.1 Compositions and physical properties of lubricants in selected experimental conditions

Lubricant		(A)	(B)	(C)	(D)	(E)
Composition, vol.%	Water	100	90	80	60	30
	Ethanol	0	10	20	10	10
	Glycerol	0	0	0	30	60
Surface free energy, mJ/m^2	Dispersion	21.8	21.6	17.5	16.2	17.3
	Polar	51.0	28.7	22.3	27.5	27.5
	Total	72.8	50.3	39.8	43.7	44.8
Spreading coefficient, mJ/m^2		–53.3	–21.8	–13.7	–20.4	–20.3
Viscosity, mPa·s		0.89	1.06	1.38	3.17	16.1
Refractive index		1.333	1.337	1.344	1.382	1.426
Critical angle, deg.		61.68	62.01	62.61	65.86	70.35
Incident angle, deg.		65.0	65.0	66.0	69.0	73.0

Table 3.2 Shape and physical properties of rubber

Rubber		(i)	(ii)	(iii)	(iv)	(v)
Curvature radius, mm		7.62	5.08	10.30	7.60	7.62
Elastic modulus, MPa		2.30	2.30	2.30	1.26	3.53
Arithmetical mean height S_a, μm		0.18	0.16	0.17	0.18	0.16
Surface free energy, mJ/m^2	Dispersion	11.0	11.0	11.0	10.6	10.6
	Polar	1.7	1.7	1.7	1.8	1.8
	Total	12.7	12.7	12.7	12.4	12.4

3.2.2 Wettability evaluation

As explained in a previous study, wettability between the rubber and glass was estimated using the spreading coefficient (S) [18]. S was obtained from the following equations:

$$S = \gamma_{AG} - (\gamma_{AW} + \gamma_{GW}) \tag{3.1}$$

$$\gamma_{ij} = \left(\sqrt{\gamma_i^d} - \sqrt{\gamma_j^d}\right)^2 + \left(\sqrt{\gamma_i^p} - \sqrt{\gamma_j^p}\right)^2 \tag{3.2}$$

where γ_{ij} is the interfacial free energy between material i and material j [28]; subscripts R, G, and L denote rubber, glass, and lubricant, respectively; γ_i d and γ_i p are the dispersion and polar components of the surface free energy of material i, respectively [28]. The calculated S values of lubricants at the rubber–glass interface are listed in Table 3.1.

3.2.3 Experimental apparatus

To determine the relationship between real contact formation and dewetting behavior, the distributions of real contact and lubricant film thickness were quantified based on a total reflection method and light interferometry using the original apparatus in Fig. 3.1 [30]. Fig. 3.2(a) shows the schematic of the experimental system used for measuring the contact states [31]. The rubber hemisphere (rubber (i)) was placed on the glass prism under lubricated conditions (lubricants (A–E)), as shown in Table 3.1, using lubricant (A) for rubber (ii–v). In the total reflection method, light from a light-emitting diode (LED) (HLV2-22RD-3W, CCS Inc., Japan) penetrated the glass through a light guide (LE-OPT-24, OPTEC FA Co., Ltd., Japan) and internally reflected on the surface of the glass.

The light scattered at the rubber–glass interface was observed by a charge-coupled device camera (AT-030MCL, JAI Ltd., Japan). In the light interferometry method, the light from another LED light source (HLV2-22BL-3W, CCS Inc., Japan) penetrated the rubber–glass interface through a telecentric lens (TV-2F-110, OPTART Co., Ltd., Japan), and light reflected from the surfaces of the rubber and

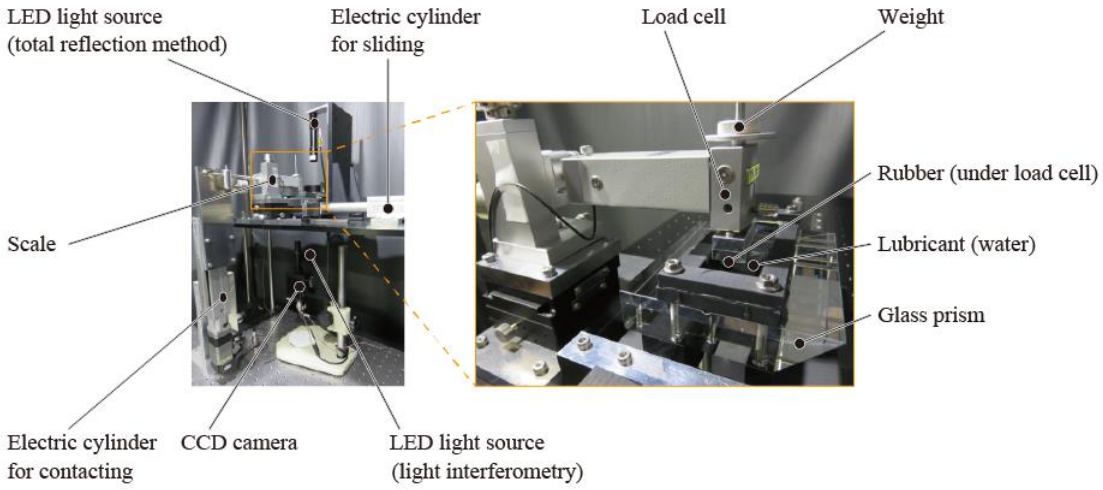

Fig. 3.1 Picture of experimental apparatus [30]

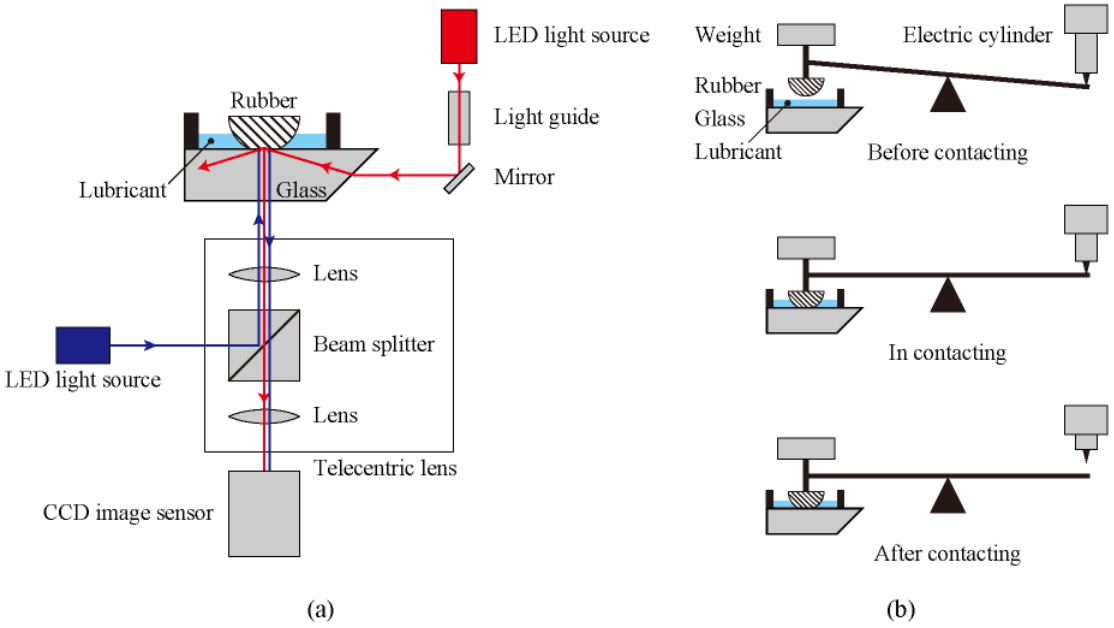

Fig. 3.2 Schematic view of the experimental system (a) and contact between rubber and glass (b) [31]

glass was observed by the same camera. The pixel format, pixel size, and frame rate were 12 bit, 3.6 μm × 3.6 μm, and 100 fps, respectively. The peaks in the total reflection and light interferometry methods appeared at 645 nm and 465 nm, respectively. As shown in Table 3.1, incident angles were set to greater than the critical angles by changing the position and angle of the mirror (Fig. 3.2(a)). The contact velocity of the rubber (v_c) was controlled from 0.10 to 1.00 mm/s in steps of 0.1 mm/s using an electric cylinder (EASM4NXD010AZMC, Oriental Motor Co., Ltd., Japan) and a scale (TL201Ts, Trinity-Lab Inc., Japan), as shown in Fig. 3.2(b). As the rubber approached the glass surface, the normal force increased until the electric cylinder and scale separated. The maximum normal force was set at 0.0981 N. The atmospheric temperature and relative humidity were controlled in the ranges 23.8–25.0 °C and 71–75%, respectively. [30]

3.3 Results

3.3.1 Real contact formation

Fig. 3.3 shows the time series of the distributions of real contact area and lubricant film thickness for rubber (i) and lubricant (A) at v_c = 0.50 mm/s. The red and blue areas indicate the real contact and lubricant film, respectively. Based on a previous study [29], the distributions of real contact and lubricant film thickness were measured. The onset time of real contact was defined as t = 0.00 s. For rubber (i) at v_c = 0.50 mm/s, the contact process was complete at t = 0.08 s. According to Fig. 3.3, the number of real contacts (N) increased, and each real contact area expanded. In addition, the lubricant

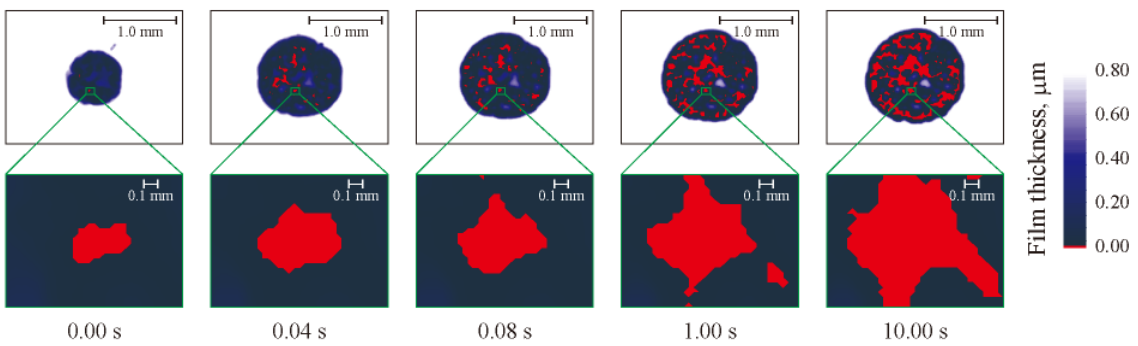

Fig. 3.3 Time dependence of the distributions of real contact and film thickness for rubber (i) and lubricant (A), respectively, at v_c = 0.5 mm/s [30]

film thickness around the real contacts increased, indicating the dewetting of the lubricant from the real contact area [13]. Fig. 3.4 shows A_r and N plotted against t and the relationship between N and A_r for the same case in Fig. 3.3 (for rubber (i) and lubricant (A) at v_c = 0.50 mm/s). A_r was defined as the total real contact area between two substrates. N was defined as the number of completely separated real contacts whose area was larger than 1 pixel by using MATLAB software (R2016b, The MathWorks, Inc., USA). At t = 0.01–0.08 s, A_r and N increased, and the rate of increase of A_r decreased at t = 0.08 s when the contact process was complete. These results suggest that A_r and N increased with the apparent contact area A, as calculated by the Hertz contact theory, before the completion of the contact process (t = 0.01–0.08 s). N increased linearly at t = 0.01–0.08 s, indicating that N is proportional to A, given a proportional relation between A and t. In contrast, A_r continued to increase by lubricant localization or dewetting after the completion of the contact process (at t = 0.08–10.00 s, the rubber remained stationary). Fig. 3.4(c) also indicates that N slightly decreased at t = 0.08–10.00 s, which indicates coalescence between real contacts.

3.3.2 Influences of each parameter on real contact formation

Here, A_{r0} is defined as A_r at $t = t_0$. t_0 is the time when $v_c t$ is equal to the approach distance (δ) calculated in the Hertz contact theory. In other words, it corresponds to the time when the contact process was complete. In Fig. 3.5, A_r is plotted against R, E, and v_c. To focus on the influence of R, the

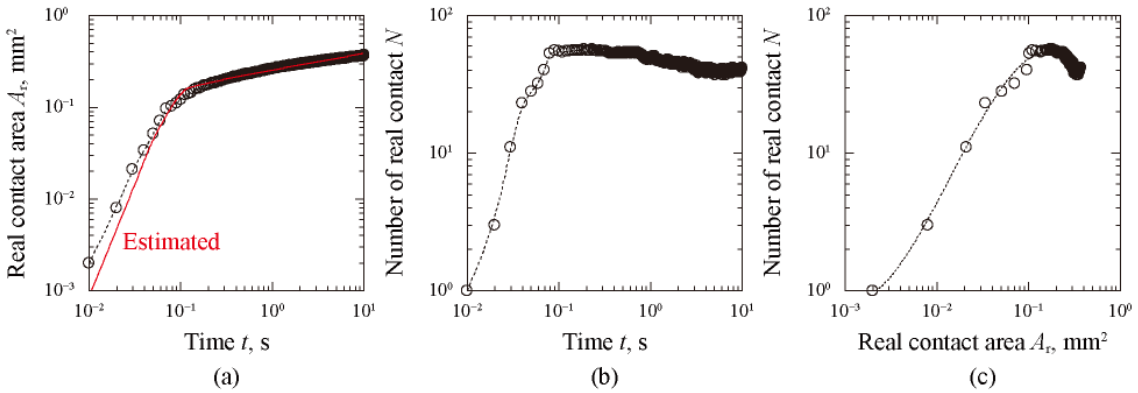

Fig. 3.4 A_r and N plotted against t and relationship between N and A_r. The red solid line in Fig. 3.4(a) gives A_r estimated based on Eqs. (3.4) and (3.5). [30]

cases of rubbers (i), (ii), and (iii) for lubricant (A) at v_c = 0.50 mm/s are plotted in Fig. 3.5(a). We confirmed that there was a negative correlation between A_{r0} and R. Fig. 3.5(b) shows the A_{r0}–E curves for rubbers (i), (iv), and (v) and lubricant (A) at v_c=0.50 mm/s and indicates that A_{r0} decreased with E. According to Fig. 3.5(c), A_{r0} decreased with v_c for rubber (i) and lubricant (A), and the rate of decrease of A_{r0} slowed with v_c. The Hertz contact theory explains that A is proportional to $R^2/3E^{-2/3}$. To eliminate the influences of R and E on A, Fig. 3.6 shows the influence of R and E on the real contact ratio A_{r0}/A_0, where A_0 is defined as the contact area at $t = t_0$. A_{r0}/A_0 decreased with R and E, showing that real contact deformation depended on R, E, and v_c because A_0 is proportional to $R^2/3E^{-2/3}$, and R, E, and v_c change the dewetting behavior between the rubber and glass during the contact process.

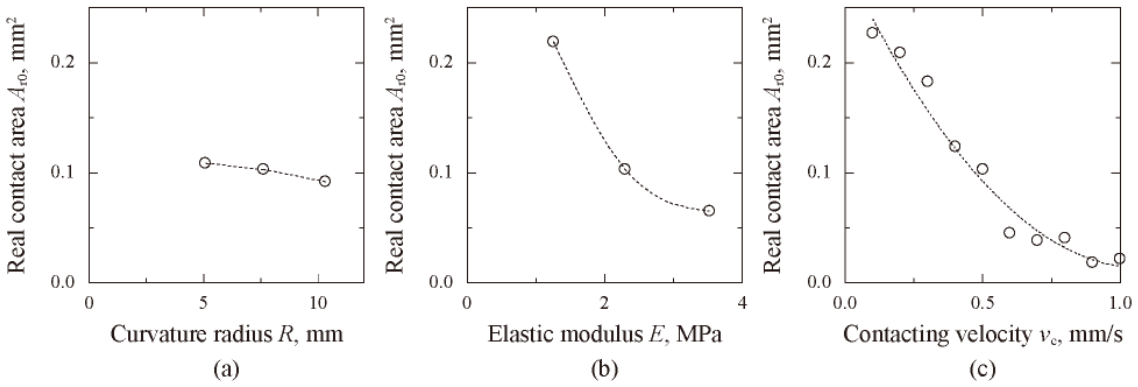

Fig. 3.5 Influence of R, E, and v_c on A_{r0} for lubricant (A) and (a) rubbers (i–iii) at v_c = 0.50 mm/s; (b) rubbers (i,iv,v) at v_c = 0.50 mm/s; (c) rubber (i) [30]

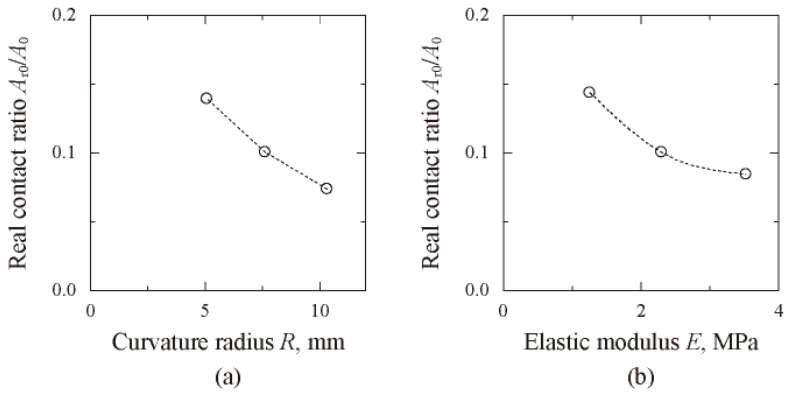

Fig. 3.6 Relationship between A_{r0}/A_0, R, and E for lubricant (A) and (a) rubbers (i–iii) at v_c = 0.50 mm/s; (b) rubbers (i,iv,v) at v_c = 0.50 mm/s [30]

Fig. 3.7(a) shows the influence of S on A_{r0} for rubber (i) and lubricants (A−C) at v_c = 0.50 mm/s. Here, the influence of η on A_{r0} for lubricants (A−C) was plotted in Fig. 3.7(a), which indicates that A_{r0} decreased with the increase in S. The influence of η on A_{r0} for rubber (i) and v_c = 0.50 mm/s is shown in Fig. 3.7(b). To eliminate the influence of S on A_{r0}, the results for lubricants (B), (D), and (E) are combined. A_{r0} was small because of the high value of S and decreased with η.

3.4 Discussion

3.4.1 Dewettability at the rubber–glass interface

We experimentally confirmed that many real contacts were formed between the rubber and glass. The time dependence of the real contact area of each real contact (a_r) can be important to discuss the time dependence of A_r. Using MATLAB software, the time dependence of a_r of each real contact point

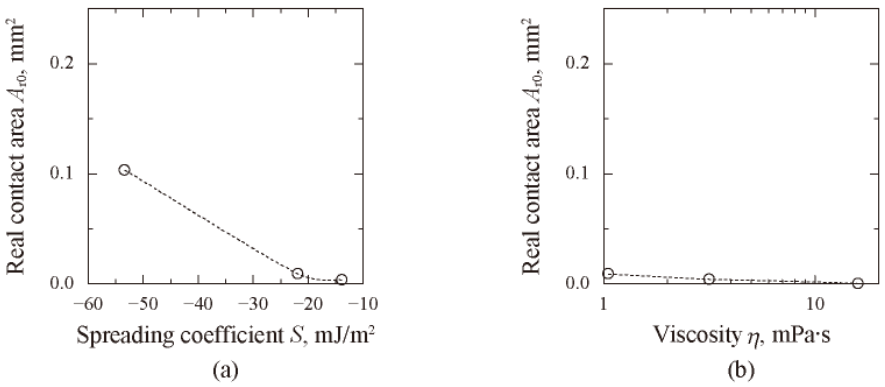

Fig. 3.7 Influence of S and η on A_{r0} for rubber (i) at v_c = 0.50 mm/s and (a) lubricants (A−C); (b) lubricants (B,D,E) [31]

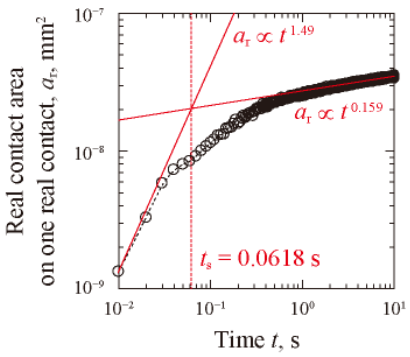

Fig. 3.8 Typical a_r–t curve for rubber (i) and lubricant (A) at v_c = 0.50 mm/s [30]

was extracted. Fig. 3.8 shows a representative example of the a_r–t curve for rubber (i) and lubricant (A) at v_c = 0.50 mm/s. a_r increased with t. In the case of a single real contact between the optically flat rubber and glass surfaces under lubricated conditions, a_r is proportional to $t^{3/2}$, which is explained by the energy balance between strain and surface energies [13]. Fig. 3.8 shows that the initially increasing rate of a_r corresponded to $t^{3/2}$. However, the increasing rate of a_r slowed down at $t \approx 0.0618$ s. The influence of roughness on the energy balance between strain and surface energies increased as a_r increased. Table 3.3 shows index numbers (n_1 and n_2) and the saturated time (t_s) for rubbers (i–v) and lubricant (A) at v_c = 0.50 mm/s. n_1 and n_2 were calculated from the increasing rate of a_r with respect to t for all real contacts on the apparent contact area at t = 0.01–0.03 and 1.00–10.00 s, respectively, based on the least-squares method. t_s is defined as the point of intersection between the two approximate lines, as shown in Fig.3.8. Table 3.3 explains that n_1, n_2, and t_s were similar, regardless of the condition of the rubbers. This result indicates that rubbers with similar roughnesses have similar n_1, n_2, and t_s, regardless of R and E.

Table 3.3 Parameters used to describe the time dependence of a_r

Rubber		(i)	(ii)	(iii)	(iv)	(v)	Average
Index numbers n_1 (t = 0.01–0.03 s)		1.49	1.44	1.46	1.50	1.51	1.48
	Standard error	0.17	0.18	0.17	0.12	0.16	-
Index numbers n_2 (t = 1.00–10.00 s)		0.159	0.142	0.161	0.161	0.121	0.149
	Standard error	0.023	0.041	0.043	0.023	0.037	-
Saturated time t_s, s		0.0618	0.0579	0.0680	0.0690	0.0611	0.0636
	Standard error	0.0081	0.0109	0.0119	0.0063	0.0129	-

As mentioned in Section 3.3.1, experimental results indicated that N in the contact phase increased linearly with A. Because the vertical displacement of rubber during contact is equal to $v_c t$, the following equation is obtained:

$$N = kA = \pi k R v_c t, (t \leq t_0) \tag{3.3}$$

where k is a constant that corresponds to the number of real contacts per area. Eq. (3.3) explains that N increases from 0 to N_0, which is defined as N at $t = t_0$. A_r is given by the sum of a_r in the following equation, where a_r is defined as a function of time $f(t)$:

$$A_r = \sum_{i=1}^{N} a_{ri} = \sum_{i=0}^{N-1} f\left(\frac{i}{N}t\right) \approx \frac{N}{t}\int_0^t f(x)\,dx, (t \leq t_0) \tag{3.4}$$

Here, given that $N = N_0$ at $t_0 < t$, A_r is calculated from Eq. (3.5):

$$A_r = \sum_{i=1}^{N_0} a_{ri} = \sum_{i=0}^{N_0-1} f\left(\frac{i}{N_0}t_0 + (t - t_0)\right) \approx \frac{N_0}{t_0}\int_{t-t_0}^{t} f(x)\,dx, (t_0 < t) \tag{3.5}$$

The red solid line in Fig. 3.4 is A_r estimated based on Eqs. (3.4) and (3.5). Here, $f(t)$ is a continuous function of time. The experimental results explain that $f(t)$ is proportional to $t^{1.49}$ at $t \leq 0.0618$ s and $t^{0.159}$ at $t > 0.0618$ s based on the values of n_1, n_2, and t_s given in Table 3.3. Considering Eq. (3.4), A_{r0} is calculated from the following equation:

$$A_{r0} = \frac{N_0}{t_0}\int_0^{t_0} f(x)\,dx \tag{3.6}$$

Eq. (3.6) shows that A_{r0} is proportional to N_0. Because Eq. (3.3) demonstrates that $N_0 = kA_0$, the following equation is obtained:

$$\frac{A_{r0}}{A_0} = \frac{k}{t_0}\int_0^{t_0} f(x)\,dx \tag{3.7}$$

This equation shows that A_{r0}/A_0 is proportional to k, which is constant. Therefore, A_{r0}/A_0 is regarded as a function of t_0. The relationship between A_{r0}/A_0 and t_0 for all rubbers and lubricant (A) is shown in

Fig. 3.9, where the plots and red solid line indicate the experimental and estimated results, respectively. The estimated A_{r0}/A_0 was calculated from Eq. (3.7), where $f(t)$ is defined as a function, which is proportional to $t^{1.48}$ at $t \leq 0.0636$ s and $t^{0.149}$ at $t > 0.0636$ s based on the average values of n_1, n_2, and t_s in Table 3.3. From Fig. 3.9, it was confirmed that A_{r0}/A_0 has a positive exponential correlation with t_0, and the increase rate of A_{r0}/A_0 slowed down at $t \approx t_s$, regardless of the experimental and estimated results. Based on these results, A_{r0}/A_0 rapidly increased because the lubricant around each real contact was aggressively dewetted at $t_0 \leq t_s$. However, this dewetting effect saturated at $t_s < t_0$. Considering the Hertz contact theory, t_0 is proportional to $R^{-1/3}E^{-2/3}v_c^{-1}$. Thus, a sharp (small R) and soft (small E) edge can make an effective structure to increase A_{r0}/A_0. At the same time, it is important to control A_0 determined by R and E, as explained in the Hertz contact theory. Note that the value of t_s is not negligible, which is not discussed in detail in this chapter.

3.4.2 Influence of lubricant parameters on dewettability

Based on the influence of S and η on the dewetting behavior of the lubricant, the dewetting velocity of one real contact is described by the characteristic dewetting velocity $v^* = |S|/\eta$ [13]. While the dewetting behavior in the presence of many real contacts (as shown in Fig. 3.3) is not explained elsewhere [9,12–15,32], it is expected that the theory for the dewetting behavior of one real contact can be used to explain the case.

In Fig. 3.10, A_{r0} is plotted against v^* for rubber (i) and lubricants (A–E) at v_c = 0.10, 0.50, and

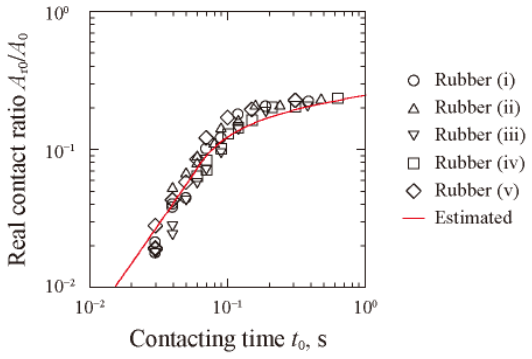

Fig. 3.9 Influence of t_0 on measured and estimated A_{r0}/A_0 for Lubricant (A) [30]

1.00 mm/s. A positive correlation existed between A_r and v^*, regardless of v_c. This result indicated that the increase in dewettability makes the lubricants between two substrates squeeze out. In addition, A_r–v^* curves can be changed by v_c. Here, the increase in v_c corresponded to the decrease in contact time (t_0), suggesting that the volume of the dewetted lubricant decreased with t_0; in other words, the volume of the dewetted lubricant is inversely proportional to v_c. Therefore, the parameter v^*/v_c can be used to quantify the influence of dewettability. Fig. 3.11 shows the relationship between A_r and v^*/v_c for rubber (i). Most results were plotted on a single curve, regardless of the values of v_c, S, and η, and A_r increased with v^*/v_c. Meanwhile, at v^*/v_c < 105.2, A_r exponentially increased with v^*/v_c, and the increasing rate of this correlation decreased at v^*/v_c > 105.2. These results indicated that the volume of the dewetted lubricant increased with v^*/v_c during contact between rubber and glass and that the dewetting effect slowed down at v^*/v_c > 105.2. Here, the energy balance between the surface free

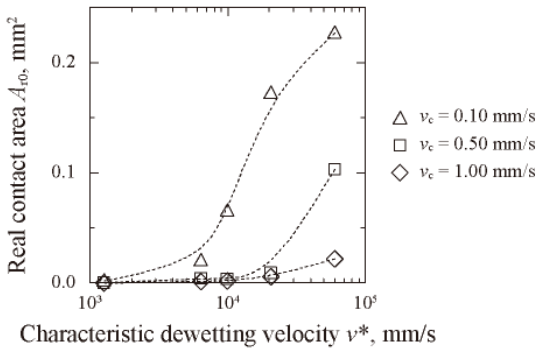

Fig. 3.10 Relationship between A_{r0} and v^* for rubber (i) at v_c = 0.10, 0.50, and 1.00 mm/s [31]

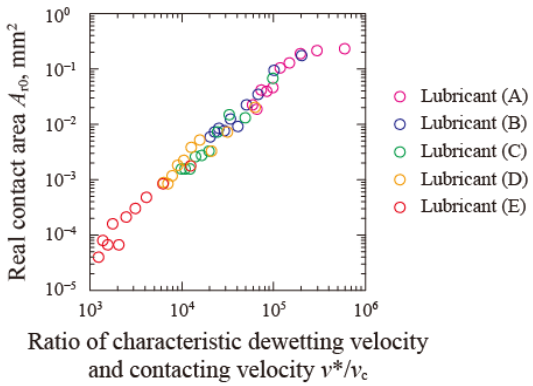

Fig. 3.11 Influence of v^*/v_c on A_{r0} for rubber (i) [31]

energy and strain energy triggers the dewetting process [14], Thus, the asymptotic value of A_r–v^*/v_c curve can be determined by the surface free energy and surface roughness, and the asymptote can confirm if t_0 is larger than the saturation time of dewetting.

3.5 Conclusions

The dewetting behavior between rubber and glass was clarified based on the influences of the radius of curvature (R), elastic modulus (E), spreading coefficient (S), lubricant viscosity (η), and contact velocity (v_c) on the measured real contact area (A_r). The following conclusions were drawn according to the experimental results.

In the contact process, the number of real contacts (N) increased simultaneously as each real contact area expanded. The lubricant film thickness around real contacts increased. When the contact process was completed, the real contact area A_{r0} decreased with R, E, S, η, and v_c. In this chapter, the theory of dewetting was developed to quantify real contact deformation between rubber and floor (glass) under lubricated conditions. Based on the developed theory, the real contact ratio A_{r0}/A_0 exponentially increased with contact time (t), and the increasing rate of A_{r0}/A_0 slowed down at $t \approx t_s$, which can be determined by surface roughness. In addition, the dewetting velocity was quantified by the characteristic dewetting velocity, $v^* = |S|/\eta$.

Therefore, to control the grip property for applications under lubricated conditions, such as in shoe soles and vehicle tires, the material and structure of rubber must be designed considering the dewetting behavior based on R, E, S, η, and v_c.

References

[1] Schallamach A., “How Does Rubber Slide?,” Wear, 17, 4, 1971, 301–12.

[2] Roberts A.D., and JJackson S.A., “Sliding Friction of Rubber,” Nature, 257, 1975, 118.

[3] Roberts A.D., and Thomas A.G., “The Adhesion and Friction of Smooth Rubber Surfaces,” Wear, 33, 1, 1975, 45–64.

[4] Barquins M., and Courtel R., “Rubber Friction and the Rheology of Viscoelastic Contact,” Wear, 32, 2, 1975, 133–50.

[5] M Barquins and A D Roberts, “Rubber Friction Variation with Rate and Temperature: Some New Observations,” Journal of Physics D: Applied Physics, 19, 4, 1986, 547.

[6] Johnson K.L., Kendall K., and Roberts A.D., “Surface Energy and the Contact of Elastic Solids,” Proceedings of the Royal Society A: Mathematical, Physical and Engineering Sciences, 324, 1558, 1971, 301–13.

[7] Greenwood J.A., and Williamson J.B.P., “Contact of Nominally Flat Surfaces,” Proceedings of the Royal Society A: Mathematical, Physical and Engineering Sciences, 295, 1442, 1966, 300–19.

[8] Bowden F.P., and Tabor D., “The Friction and Lubrication of Solids Part II,” Physics Today, 17, 6, 1964, 72.

[9] Roberts A.D., “Squeeze Films between Rubber and Glass,” Journal of Physics D: Applied Physics, 4, 3, 1971, 423–32.

[10] Roberts A.D., and Tabor D., “The Extrusion of Liquids between Highly Elastic Solids,” Proceedings of the Royal Society of London Series A, Mathematical and Physical Sciences, 325, 1562, 1971, 323–45.

[11] Brochard-Wyart F., and De Gennes P.G., “Dewetting of a Water Film between a Solid and a Rubber,” Journal of Physics: Condensed Matter, 6, 23A, 1994, A9–12.

[12] Martin P., Silberzan P., and Brochard-Wyart F., “Sessile Droplets at a Solid/Elastomer

Interface," Langmuir, 13, 18, 1997, 4910–4.

[13] Martin P., and Brochard-Wyart F., "Dewetting at Soft Interfaces," Physical Review Letters, 80, 15, 1998, 3296–9.

[14] Martin A., Buguin A., and Brochard-Wyart F., "Dewetting Nucleation Centers at Soft Interfaces," Langmuir, 17, 21, 2001, 6553–9.

[15] Martin A., Clain J., Buguin A., and Brochard-Wyart F., "Wetting Transitions at Soft, Sliding Interfaces," Physical Review E - Statistical, Nonlinear, and Soft Matter Physics, 65, 3, 2002, 031605/1-031605/4.

[16] Martin A., Buguin A., and Brochard-Wyart F., "'Čerenkov' Dewetting at Soft Interfaces," Europhysics Letters, 57, 4, 2002, 604–10.

[17] Nishi T., Moriyasu K., Harano K., and Nishiwaki T., "Influence of Surface Free Energy on Rubber Friction Properties under Water/Ethanol Lubrilated Conditions," Tribologists, 59, 11, 2014, 41–7.

[18] Nishi T., Moriyasu K., Harano K., and Nishiwaki T., Influence of dewettability on rubber friction properties with different surface roughness under water/ethanol/glycerol lubricated conditions. Tribol. Online, vol. 11, Japanese Society of Tribologists, 2016, p. 601–7.

[19] Li K.W., and Chen C.J., "The Effect of Shoe Soling Tread Groove Width on the Coefficient of Friction with Different Sole Materials, Floors, and Contaminants," Applied Ergonomics, 35, 6, 2004, 499–507.

[20] Li K.W., Wu H.H., and Lin Y.C., "The Effect of Shoe Sole Tread Groove Depth on the Friction Coefficient with Different Tread Groove Widths, Floors and Contaminants," Applied Ergonomics, 37, 6, 2006, 743–8.

[21] Li K.W., and Chin J.C., "Effects of Tread Groove Orientation and Width of the Footwear Pads on Measured Friction Coefficients," Safety Science, 43, 7, 2005,

391–405.

[22] Blanchette M.G., and Powers C.M., “The Influence of Footwear Tread Groove Parameters on Available Friction,” Applied Ergonomics, 50, 2015, 237–41.

[23] Yamaguchi T., Katsurashima Y., and Hokkirigawa K., “Effect of Rubber Block Height and Orientation on the Coefficients of Friction against Smooth Steel Surface Lubricated with Glycerol Solution,” Tribology International, 110, 2017, 96–102.

[24] Maegawa S., Itoigawa F., and Nakamura T., “Effect of Surface Grooves on Kinetic Friction of a Rubber Slider,” Tribology International, 102, 2016, 326–32.

[25] Yamaguchi T., Umetsu T., Ishizuka Y., Kasuga K., Ito T., Ishizawa S., et al., “Development of New Footwear Sole Surface Pattern for Prevention of Slip-Related Falls,” Safety Science, 50, 4, 2012, 986–94.

[26] Maegawa S., Itoigawa F., and Nakamura T., “A Role of Friction-Induced Torque in Sliding Friction of Rubber Materials,” Tribology International, 93, 2016, 182–9.

[27] Berry J.D., Neeson M.J., Dagastine R.R., Chan D.Y.C., and Tabor R.F., “Measurement of Surface and Interfacial Tension Using Pendant Drop Tensiometry,” Journal of Colloid and Interface Science, 454, 2015, 226–37.

[28] Kaelble D.H., “Dispersion-Polar Surface Tension Properties of Organic Solids,” Journal of Adhesion, 2, 2, 1970, 66–81.

[29] Nishi T., Moriyasu K., and Nishiwaki T., “Precise Measurement of Clearance between Two Substrates Using Evanescent Waves,” Tribology Online, 12, 5, 2017, 251–6.

[30] Nishi T., “Influence of Curvature Radius, Elastic Modulus, and Contact Velocity on Real Contact Formation between Rubber Hemisphere and Glass Plate during Contact Process under a Water-Lubricated Condition,” Tribology International, 130, 2019, 284–8.

[31] Nishi T., “Influence of Lubricant Properties and Contacting Velocity on Real Contact

Formation between Rubber and Glass in a Contact Process," Tribology International, 127, 2018, 240–4.

[32] Brochard-Wyart F., and De Gennes P.G., "Dewetting of a Water Film between a Solid and a Rubber," Journal of Physics Condensed Matter, 4, 10, 1994, 1727–35.

Chapter 4

Rubber friction with uniform wetting states: sliding process

4.1 Introduction

Rubber is one potential material for improving slip resistance and sealing performance. It has been widely applied to outer-soles of shoes, vehicle tires, floors, handgrips, and packing materials. The slip resistance and sealing performance of these objects are essential for safety enhancements. In particular, slip resistance of outer-soles is indispensable for preventing slip-and-fall accidents, especially on wet floors [1,2], while the sealing performance of faucet packing is crucial for reducing water leaks [3]. Therefore, it is necessary to establish a design guide for rubber and its properties, especially in lubricated conditions.

In general, the friction force F is the sum of the plowing F_{plow}, hysteresis F_{hys}, and adhesion F_{ad} terms [4–7]. F_{plow} corresponds to the digging resistance between the rubber and floor. Thus, F_{plow} for rubber outers-soles on a dirt track can be controlled based on the tread pattern [8]. The rubber surface under friction can be deformed cyclically by asperities on the floor (especially for a rough floor) due to microscopic contact [7]. During the deformation process, the rubber surface is compressed on the front contact edge and decompressed on the rear contact edge. Rubber is not a perfectly elastic material but viscoelastic, and the compression force is usually larger than the decompression force, which generates F_{hys} [7]. In addition, real contacts are formed and are sheared during friction. The shear strength of real contacts relates to F_{ad}, which is proportional to the real contact area A_{r} [4]. Alternatively, F_{plow} depends on structural factors such as tread patterns, while F_{hys} and F_{ad} can be designed based on the rubber compound. As a result, the value of F_{hys} is not negligible for rubber friction on a rough floor in both lubricated and unlubricated conditions. Conversely, the contribution

of F_{hys} to F on a smooth floor is minimal regardless of lubrication. Since lubricant intervention decreases A_r, the value of F_{ad} is usually small for lubricated conditions [9]. Thus, it would be desirable to maximize A_{ad} by ensuring large $A_{r,}$ thereby achieving high slip resistance regardless of floor roughness and lubrication conditions.

Based on Stribeck curves, the friction coefficient μ can be determined by the normal force F_n, sliding velocity v_s, and lubricant viscosity η under lubrication [10]. Real contacts between two substrates are formed in boundary and mixed lubrication conditions except for the case of fluid lubrication, meaning that $F_{ad} > 0$ due to $A_r > 0$. Additionally, it has also been reported that the spreading coefficient S influences μ for boundary and mixed lubrication, where S is the parameter of wettability [11]. The relationship between S, A_r, and μ has been studied for decades [12–23]. Roberts has reported that real contacts can be enlarged based on the energy balance between the surface free energy γ and strain energy (dewetting effect) [12–14]. This theory was developed by examining the time dependency of film thickness around the real contact between optically flat rubber and glass [15–17]. The dewetting effect can promote real contact formation between rubber and glass, leading to an increase in μ [18–20]. In addition, the real contact formation between a rubber hemisphere and a glass plate is also sensitive to contact velocity v_c, and the dewetting effect depends on the curvature radius of the rubber hemisphere R, elastic modulus, S, and η [21,22], which was demonstrated in the 2nd chapter. Shibata et al. explored the relationship between slip resistance of shoes and S and clarified that the dewetting effect in practical shoe applications depends on S [23]. In practical rubber applications such as outer-soles, the rubber surface approaches the counter surface (floor) and starts sliding. Thus far, real contact formation in contact and sliding processes has not been elucidated with consideration of both v_c and v_s, but the understanding of this relationship is meaningful to enhance the slip resistance of rubber.

This chapter aims to clarify the influence of dewetting behavior on real contact formation and friction behavior between a rubber hemisphere and a glass plate. Thus, the influence of v_c, v_s S, and η

on A_r and μ in contact and subsequent sliding processes were explored, and the effects of unforced dewetting and enforced wetting on real contact formation are discussed.

4.2 Experimental methods

4.2.1 Sample preparation and wettability evaluation

Contact and friction between a rubber hemisphere and an optically flat glass (BK7) plate (084.4L100-45DEG-6P-4SH3.5, SIGMAKOKI Co., Ltd., Japan) under lubricated conditions were measured. The rubber hemisphere was made from silicon rubber (Sylgard 184, Dow Corning Toray Co., Ltd., Japan) through molding in a concave lens (S-SLB-10-15 N, SIGMAKOKI Co., Ltd., Japan). Titanium oxide (A150, Sakai Chemical Industry Co., Ltd., Japan) was added to the rubber at 10 vol.% to ensure light reflected light in the total reflection method [21,22,24]. A dynamic viscoelastic measurement device (Reogel E4000, UBM Co., Ltd., Japan) was used to measure the elastic modulus of rubber, and the value was 2.30 MPa. The curvature radius R (=7.62 mm) of the rubber hemisphere was quantified using a One-Shot 3D measuring macroscope (VR3000, Keyence Corporation, Japan). Based on the 0.100 mm^2 geometry of the undermost rubber, the arithmetical mean height S_a was also measured, and its value was 0.18 μm. The influence of R on S_a was eliminated by using plane correction in the accompanying software (VR-H1A, Keyence Corporation, Japan). Consequently, there was no change of S_a before and after the friction tests. Furthermore, the contact angles were measured using a contact angle meter (DMs-401, Kyowa Interface Science Co., Ltd., Japan) and a 1.0 μL-drop of water deionized with a demineralizer (REP343RB, Toyo Seisakusyo, Ltd., Japan), and diiodomethane (Wako 1st grade, Wako Pure Chemical Industries, Ltd., Japan) content was also measured. The rubber and glass surface energies are listed in Table 4.1 based on the Kaelble and Uy theory [25].

Since γ and η for mixtures of water, ethanol, and glycerol are determined by the blend ratio [11,20–22,25], it is reasonable to use mixtures to investigate the influence of S and η on real contact formation and friction behavior. Table 4.2 presents five mixtures of water deionized with the

demineralizer, ethanol (Wako 1st grade, Wako Pure Chemical Industries, Ltd., Japan), and glycerol (Wako 1st grade, Wako Pure Chemical Industries, Ltd., Japan). The values of *S* for lubricants (A–C) varied, but the values of η were similar. In contrast, for lubricants (B, D, and E), *S* was comparable but η was different. Moreover, the Kaelble–Uy theory and the pendant-drop method were used to measure γ of each lubricant [11,23,25,26] and an Ostwald viscometer (2370-03-10, Climbing Co., Ltd., Japan) was used to quantify η.

The wettability *S* at a triple point where rubber, lubricant, and glass are in contact is calculated from the interfacial free energy between materials i and j γ_{ij}.

$$S = \gamma_{AG} - (\gamma_{AW} + \gamma_{GW}) \tag{4.1}$$

Here, γ_{ij} is quantified by γ based on the following equation:

$$\gamma_{ij} = \left(\sqrt{\gamma_i^d} - \sqrt{\gamma_j^d}\right)^2 + \left(\sqrt{\gamma_i^p} - \sqrt{\gamma_j^p}\right)^2 \tag{4.2}$$

where indices R, G, L, d, and p indicate rubber, glass, lubricant, and the dispersion and polar components, respectively [11,20–22,25]. Table 4.2 also displays the quantified values of *S* for each lubrication condition.

Table 4.1 Surface free energies of silicon rubber and glass

	Surface free energy, mJ/m^2		
	Dispersion	Polar	Total
Rubber	11.0	1.7	12.7
Glass	30.2	5.7	35.9

Table 4.2 Lubricant composition, physical properties, and spreading coefficient for each lubricant condition

Lubricant	Composition, vol.%			Surface free energy, mJ/m^2			Viscosity, mPa·s	Spreading coefficient, mJ/m^2
	Water	Ethanol	Glycerol	Dispersion	Polar	Total		
(A)	100	0	0	21.8	51.0	72.8	0.89	−53.3
(B)	90	10	0	21.6	28.7	50.3	1.06	−21.8
(C)	80	20	0	17.5	22.3	39.8	1.38	−13.7
(D)	60	10	30	16.2	27.5	43.7	3.17	−20.4
(E)	30	10	60	17.3	27.5	44.8	16.1	−20.3

4.2.2 Experimental apparatus

Using the experimental system shown in Fig. 4.1, the contact condition between the rubber hemisphere and glass plate was observed, and the friction force was also measured. In addition, the real contact and film thickness distribution was measured employing the total reflection method and light interferometry to observe the interface between the two substrates through glass using a charge-coupled device camera (AT-030MCL, JAI Ltd., Japan) [21,22,24]. The pixel format, pixel size, and frame rate were set at 12 bit, 3.6 μm × 3.6 μm, and 100 fps, respectively. Light-emitting diode light sources with different wavelengths (HLV2-22RD-3W/HLV2-22BL-3W, CCS Inc., Japan) were used in the total reflection method and light interferometry, respectively. In the total reflection method, a light guide (LE-OPT-24, OPTEC FA Co., Ltd., Japan) and a mirror (RPB3-20-550, SIGMAKOKI Co., Ltd., Japan) were used to ensure that red light reflected internally on the glass surface at an arbitrary angle which was determined according to a previous study [21]. In the light interferometry, blue light vertically penetrated the interface using a telecentric lens (TV-2F-110, OPTART Co., Ltd., Japan).

The rubber hemisphere approached the glass surface at v_c = 0.10, 0.50, and 1.00 mm/s using an electric cylinder (EASM4NXD010AZMC, Oriental Motor Co., Ltd., Japan). The contact process was complete when the contact cylinder separated from a scale that included a weight (0.0981 N).

Afterward, the glass started to slide within 0.01 s using another electric cylinder (EACM4D30AZAC, Oriental Motor Co., Ltd., Japan) at v_s = 0.10, 1.00, and 10.00 mm/s, and the sliding distance d was set to 10.0 mm. Furthermore, the friction force was measured by a load cell (TL201Ts, Trinity-Lab Inc., Japan) at 1 kHz, and the contact condition and friction force were quantified at $d \leq 5.0$ mm. Finally, the laboratory temperature and relative humidity were set at 23.4°C–24.0°C and 68%–71%RH, respectively.

4.2.3 Definitions of t_0, t_1, and t_2

The dewetting effect promotes real contact formation during contact between a rubber hemisphere and a glass plate [21,22]. Therefore, it was expected that A_r and μ would increase by the dewetting effect during the sliding process. We focused on three time periods (i.e., $t = t_0$, t_1, and t_2) to discuss the

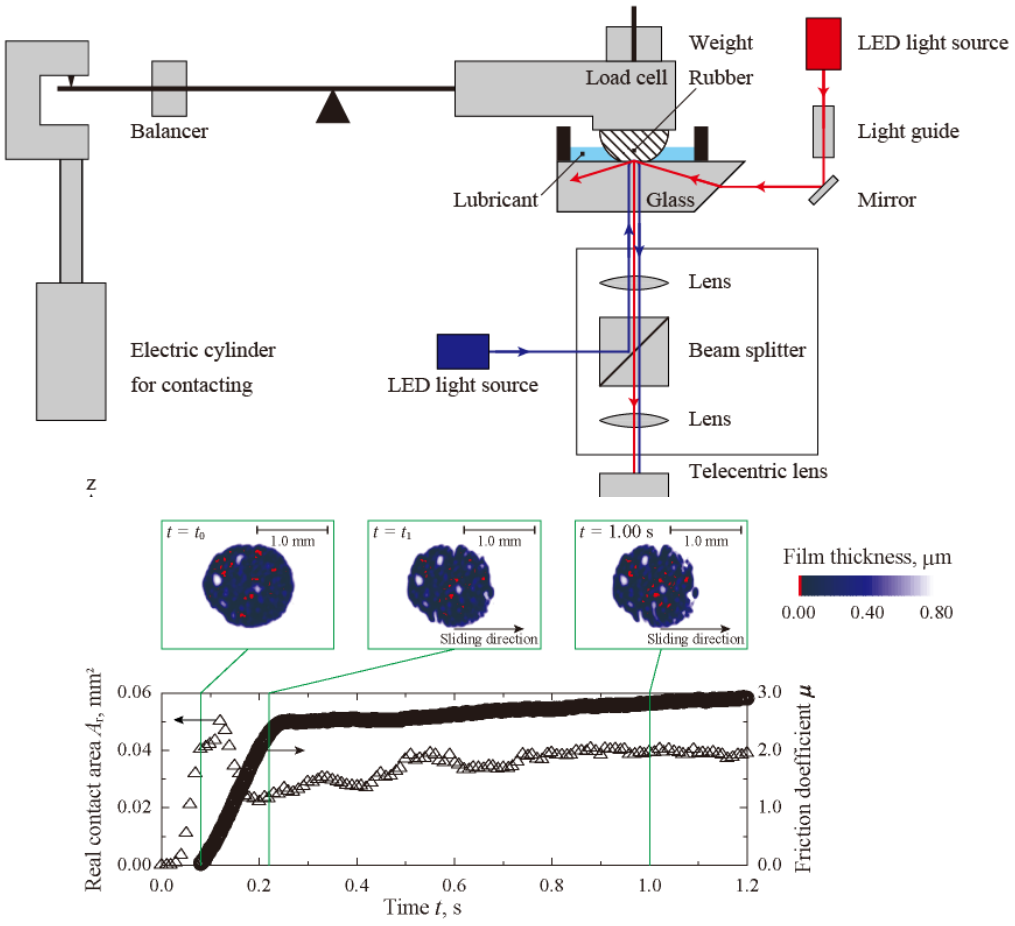

Fig. 4.2 Time dependency of contact condition, A_r, and μ for lubricant (B) at v_c = 0.50 mm/s and v_s = 1.00 mm/s [27].

dewetting effect during contact and sliding processes; t = 0 s is defined as the time when the first real contact was formed, $t_0 = \delta/v_c$, where δ is the depth of indentation based on the Hertz contact theory [22], and t_1 is defined as the time when d^2F/dt^2 exhibited its first negative peak. The negative peak of d^2F/dt^2 corresponds to strain relaxation in the rubber, caused by the first slip between the two substrates. Thus, $t = t_1$ corresponded to when the rubber was on the verge of sliding, and $t = t_2$ was defined as the period at d = 5.00 mm (steady friction). In the chapter below, d, A_r, and μ at $t = t_0$, t_1, and t_2 are represented by respective subscripts for different periods (e.g., A_{r0} is defined as the A_r at $t = t_0$, and d_1 ($=v_s(t_1 - t_0)$) corresponds to the sliding distance required for sliding).

4.3 Results

4.3.1 Time dependency of A_r and μ during contacting and sliding processes

Fig. 4.2 illustrates the real contact and film thickness distribution at $t = t_0$, t_1, and 1.00 s, and the time dependency of A_r and μ at 0.00 s $\leq t \leq$ 1.20 s for lubricant (B) at v_c = 0.50 mm/s and v_s = 1.00 mm/s. Many real contacts between the rubber and glass during the contact and sliding processes were formed, and the distribution and size of real contacts varied with t. When the rubber approached the glass surface (0.00 s $\leq t \leq t_0$), A_r increased. There was no macroscopic slip when the contact process was complete even though the tangential force was applied at the interface ($t_0 < t \leq t_1$); A_r decreased after the initial increase but μ continuously increased. Every instance of real contact continuously expanded due to the unforced dewetting effect, but this real contact formation would saturate, as reported in a previous study [22]. The dewetting equilibrium changed on the front edge of real contacts due to enforced wetting caused by sliding at v_s, which would cause a decrease in A_r at $t_0 < t \leq t_1$. Following the peeling period, the equilibrium point variation between unforced dewetting and enforced wetting caused the increase in A_r and μ at $t_1 < t \leq$ 1.20 s. For other lubrication conditions, v_c, and v_s, similar time dependencies of A_r and μ were confirmed except for lubricant (E) at v_s = 10.00 mm/s, corresponding to mixed lubrication that was similar to fluid lubrication.

4.3.2 Influence of v_c and v_s on contact and frictional behavior

In Fig. 4.3, values of d_1, A_r, and μ for lubricant (ii) at v_s = 1.00 mm/s are plotted against v_c. The dewetted lubricant volume decreased with v_c after contact ($t = t_0$), and A_{r0} decreased with v_c, as previously reported [21,22]. Then at $t = t_1$, d_1, A_{r1}, and μ_1 decreased with v_c. The decrease in d_1 corresponded to the decrease in energy required to peel the interface and start continuous friction. Consequently, d_1 was determined by the lubricant volume primarily dewetted during contact because the breaking energy of the interface increased with A_{r1}, especially at 0.00 s < $t \leq t_0$ (determined within 0.00 s < $t \leq t_1$,). Considering the adhesion term is proportional to A_r, the negative correlation between μ_1 and v_c was caused by the negative correlation between A_{r1} and v_c. In the continuous friction ($t = t_2$), A_{r2} and μ_2 also decreased with v_c, which indicated that the effect of real contact formation during the contacting process still had the influence. However, the influence of v_c on A_{r2} and μ_2 relatively decreased compared to the results at $t = t_1$ because the negative gradient of A_r and μ decreased.

Fig. 4.4 shows influence of v_s on d, A_r, and μ for lubricant (ii) at v_c = 0.50 mm/s. As expected, just before sliding at v_s ($t = t_0$), A_{r0} was almost the same. In the sliding process at $t = t_1$, d_1, A_{r1}, and μ_1 decreased with v_s, which indicates that the dewetting effect on the real contact formation at $t_0 < t \leq t_1$ decreased with v_s. In the steady friction ($t = t_2$), because the negative gradient of A_{r2} was larger than that of A_{r1}, the equilibrium point of real contact formation was more sensitive to v_s in this phase. μ_2 also decreased with v_s, which would be caused by the negative relationship between A_{r2} and v_s.

4.3.3 Influence of S and η on contact and frictional behavior

In Fig. 4.5, the influence of S on d, A_r, and μ for lubricants (A–C) at v_c = 0.50 mm/s and v_s = 1.00 mm/s is shown. The same negative correlation between A_{r0} and S was confirmed as previously reported [21], which explains that the dewetting effect during the contacting process decreased with S. At $t = t_1$ and t_2, d, A_r, and μ also decreased with S, would also be explained by the decrease in the dewetting effect.

Fig. 4.6 shows d, A_r, and μ plotted against η for lubricants (B,D,E) at v_c = 0.50 mm/s and v_s =

1.00 mm/s. d, A_r, and μ also decreased with η. It has been reported that the dewetting effect decreases with both η and S [21]. Hence, the negative dependencies of η on d, A_r, and μ are also explained by the decrease of the dewetting effect caused by the increase in η.

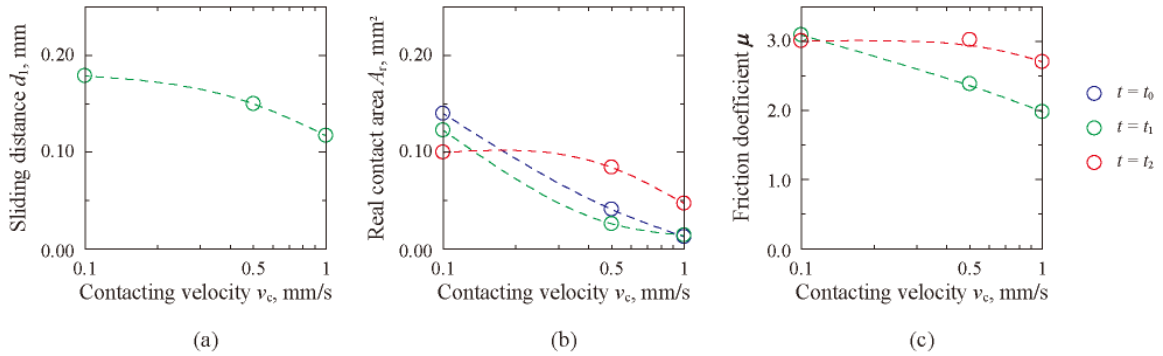

Fig. 4.3 A_r, and μ for lubricant (B) at v_s = 1.00 mm/s plotted against v_c on d [27]

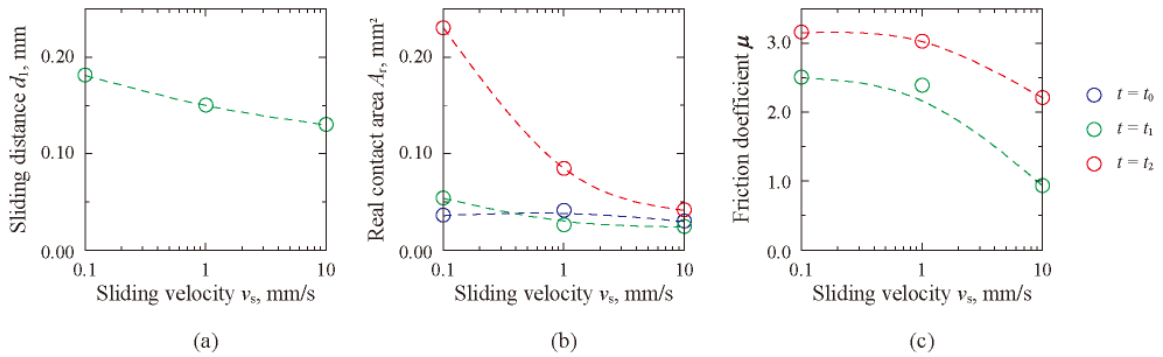

Fig. 4.4 Influence of v_s on d, A_r, and μ for lubricant (B) at v_c = 0.50 mm/s. [27]

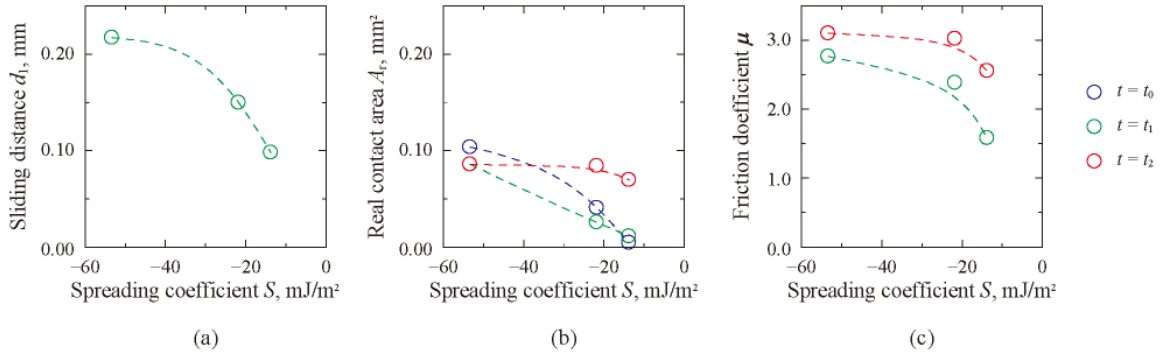

Fig. 4.5 Relationship among d, A_r, μ, and S at v_c = 0.50 mm/s and v_s = 1.00 mm/s for lubricants (A–C). [27]

4.4 Discussion

4.4.1 Real contact area expan sion caused by dewetting effect

It has been reported that real contact area is theoretically determined by γ in addition to physical conditions: elastic modulus, Poisson ratio, R, and F_n [26]. When at least one of two surfaces consists of a soft material like rubber, the dewetting effect gets remarkable. The real contact formation based on dewetting effect (Fig. 4.7) is caused by the balance between γ and strain energy [14–19]. Moreover, the radius of one real contact r is proportional to $(|S|t/\eta)^{3/4}$ [16], leading to the following equation, considering the real contact area of one real contact a_r is proportional to r^2:

$$a_r \propto \left(\frac{|S|}{\eta}t\right)^{\frac{3}{2}} = (v^* t)^{\frac{3}{2}} \tag{4.3}$$

where v^* is the characteristic dewetting velocity, defined as $|S|/\eta$. Experimentally, it has been reported that the initial time dependency of a_r can be predicted by Eq. (4.3), but due to surface roughness or interference between asperities, the increasing rate of a_r can slow down [22]. If $a_r = f(t)$ and the distribution of asperities on the rubber is uniform, A_{r0} was calculated from t_0 and the number of real contacts when the contact process was completed N_0 based on Eq. (4.4) [22]:

$$A_{r0} = \frac{N_0}{t_0}\int_0^{t_0} f(t)\,\mathrm{d}t \tag{4.4}$$

Since the surface geometry of the rubber hemisphere and F_n was constant, the value of N_0 was expected to be constant. Thus, Eq. (4.4) explains that A_{r0} is a function of t_0. Assuming that the influence of saturation of real contact expansion is small, Eq. (4.5) is obtained:

$$A_{r0} \propto \frac{N_0}{t_0}\int_0^{t_0} (v^* t)^{\frac{3}{2}}\,\mathrm{d}t \propto (v^* t_0)^{\frac{3}{2}} \tag{4.5}$$

Eq. (4.5) explains that v^*t_0 determines the value of A_{r0}. Even if the influence of saturation time of real contact expansion is not negligible, there would be a positive correlation between A_{r0} and v^*t_0. In the sliding process, a lubricant inflow at the front edge decreases a_r, but at the same time, lubricant is drained from the interface [19]. Therefore, real contact formation would be sensitive to v^* during both contacting and sliding processes. In Fig. 4.8, A_r and μ at v_c = 0.50 mm/s and v_s = 1.00 mm/s are plotted against v^*. In all phases, A_r and μ increased with v^*, as predicted by Eq. (4.6).

4.4.2 Relationship between unforced dewetting and enforced wetting

While the influence of v^* corresponds to the unforced dewetting effect, v_c and v_s cause enforced wetting effect, because the lubricants are squeezed and entered between the rubber and glass during the contacting and sliding processes, respectively. Here, A_{r0} is theoretically determined by not only v^* but also by t_0. Because t_0 is inversely proportional to v_c, v^*/v_c would be an index of the ratio of unforced dewetting and enforced wetting, mainly during the contacting process [21]. Fig 4 .9 shows

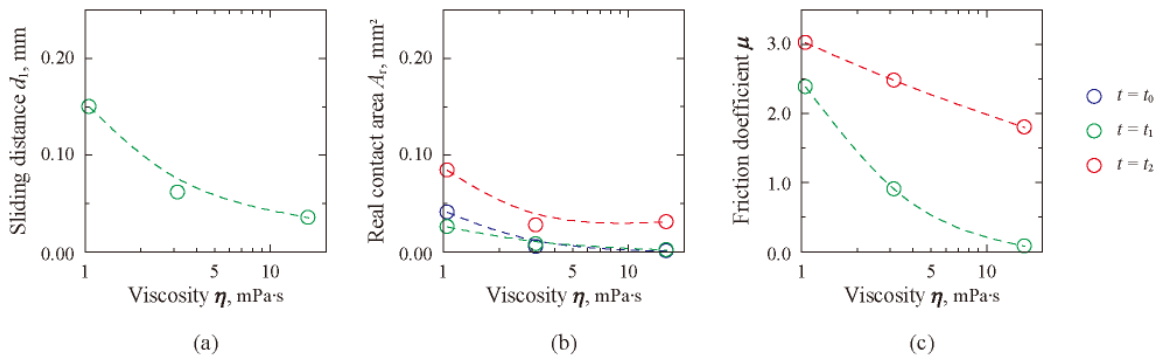

Fig. 4.6 d, A_r, and μ plotted against η at v_c = 0.50 mm/s and v_s = 1.00 mm/s for lubricants (B,D,E). [27]

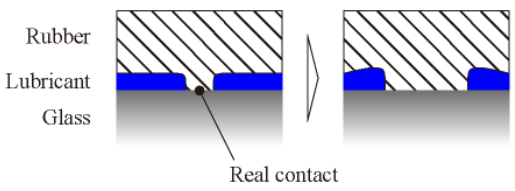

Fig. 4.7 Schematic view of dewetting behavior between rubber and glass associated with increased real contact area under a lubricated condition. [27]

the relationship between A_{r0} and v^*/v_c. As previously reported, v_s and A_{r0} positively correlated with v^*/v_c in all lubricant conditions [21]. Based on Eq. (4.5), A_{r0} was proportional to the 3/2 power of v^*/v_c at $v^*/v_c \leq 10^5$, but the increasing rate decreased at $10^5 < v^*/v_c$ due to the saturation of the dewetting effect.

In the sliding process, both unforced and enforced wetting effects are expected to determine contact conditions, and the en forced wetting effect would be determined by v_s in addition to v^* and v_c. Considering that real contact formation in the sliding process is also related to v^*t, and that t corresponded to the time required for dewetting, which is inversely proportional to v_s, it is reasonable to regard v^*/v_s as an index to explain the influences of both real contact expansion and lubricant inflow in the sliding process, as well as v^*/v_c in the contact process. Thus, it is expected that the balance between unforced dewetting and enforced wetting during contacting and sliding processes is

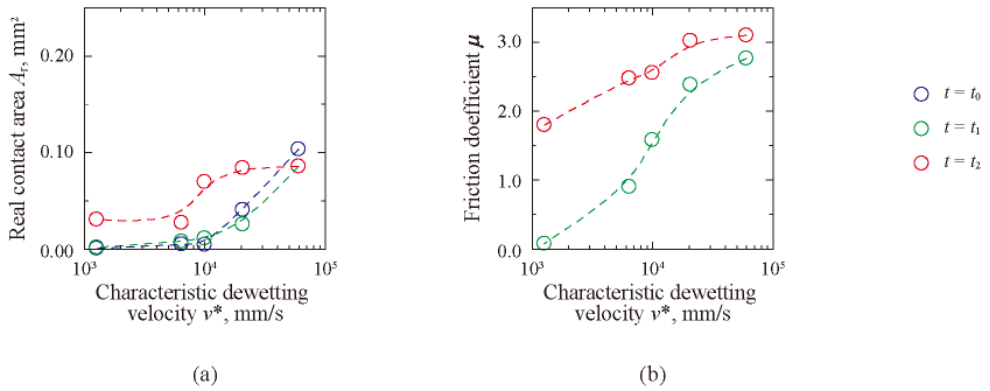

Fig. 4.8 Influence of v^* on A_r, μ at v_c = 0.50 mm/s and v_s = 1.00 mm/s. [27]

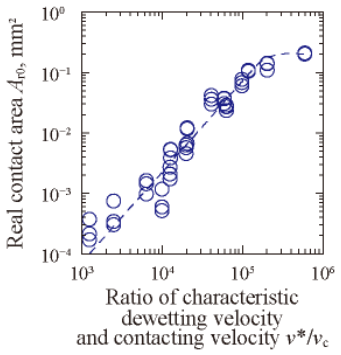

Fig. 4.9 Relationship between A_{r0} on v^*/v_c for all conditions of v_c, v_s, S, and η. [27]

explained based on both v^*/v_c and v^*/v_s. Fig. 4.10 shows the mapping A_r and μ as a function of v^*/v_c and v^*/v_s. Except for $\mu_0 = 0$ (due to $d = 0.00$ mm), the dependencies of v^*/v_c and v^*/v_s on A_r and μ depended on t. Fig. 4.11 shows the influences of v^*/v_c on A_r and μ at $10^{3.78} \leq v^*/v_s \leq 10^{4.31}$ which are extracted from Fig. 4.10, and indicates that A_r and μ increased with v^*/v_c regardless of t and that the increasing rate of A_r–t and μ–t curves decreased with the passage of t. These results suggest that A_r

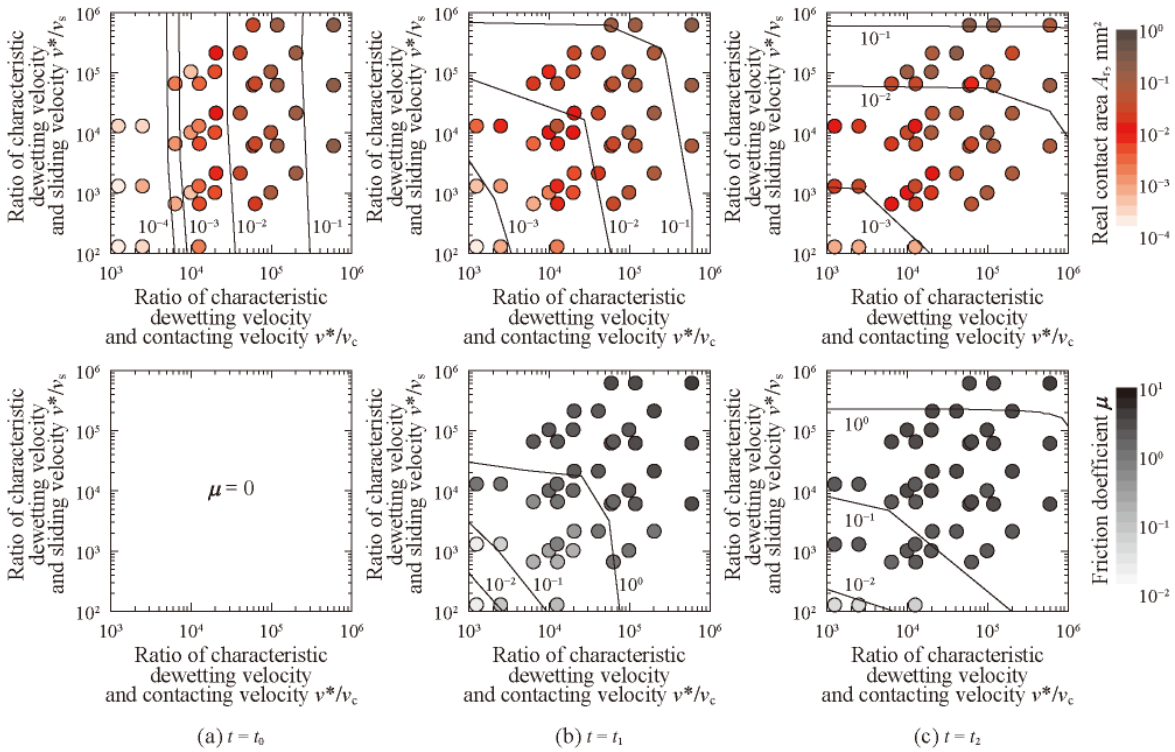

Fig. 4.10 Mapping of A_r, and μ at $t = t_0$, t_1, and t_2 as a function of v^*/v_c and v^*/v_s.[27]

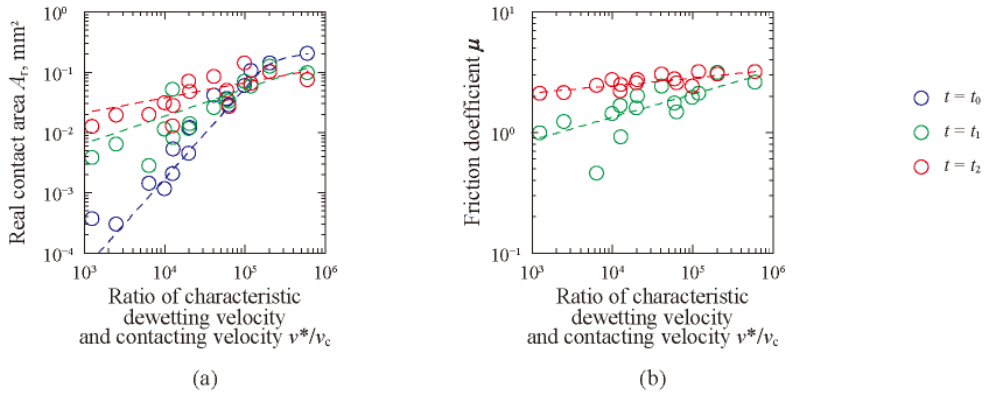

Fig. 4.11 Influence of v^*/v_c on A_r and μ at $10^{3.78} \leq v^*/v_s \leq 10^{4.31}$. [27]

after the contacting process was determined by v^*/v_c at least within $d \leq 5.00$ mm, and that the influence of v^*/v_c slowed down during the sliding process. On the other hand, Fi g. 4.12 shows A_r and μ plotted against v^*/v_s at $10^{4.10} \leq v^*/v_c \leq 10^{4.31}$ in Fig. 4.12. In comparison, there was no influence of v^*/v_s at $t = t_0$, A_r and μ increased with v^*/v_s. Except for the plot at $v^*/v_s = 10^{2.10}$, the increasing rates of A_{r1} and μ_1 were higher than the cases of A_{r2} and μ_2. Both A_r and μ were very sensitive to v^*/v_s in the sliding process (e.g., especially before initiation of continuous sliding), except for the case in which A_r was negligible. Based on these experimental results, the balance of unforced dewetting and enforced wetting effects in contact and sliding (except for a mode of mixed lubrication that was similar to fluid lubrication) was determined by v^*/v_c and v^*/v_s, and that the contributions of v^*/v_c and v^*/v_s depended on the period.

4.5 Conclusions

In this chapter, real contact formation and sliding friction behavior between a rubber hemisphere and glass plate under lubricated conditions during contact and sliding, respectively, were examined from the viewpoint of unforced dewetting and enforced wetting effects. The experimental results revealed the real contact area decreased with the contacting velocity v_c, sliding velocity v_s, spreading coefficient S, and lubricant viscosity η after contact (A_{r0}), just before sliding (A_{r1}), and when the friction was in steady-state sliding (A_{r1}), respectively. Similar dependency of these parameters on the

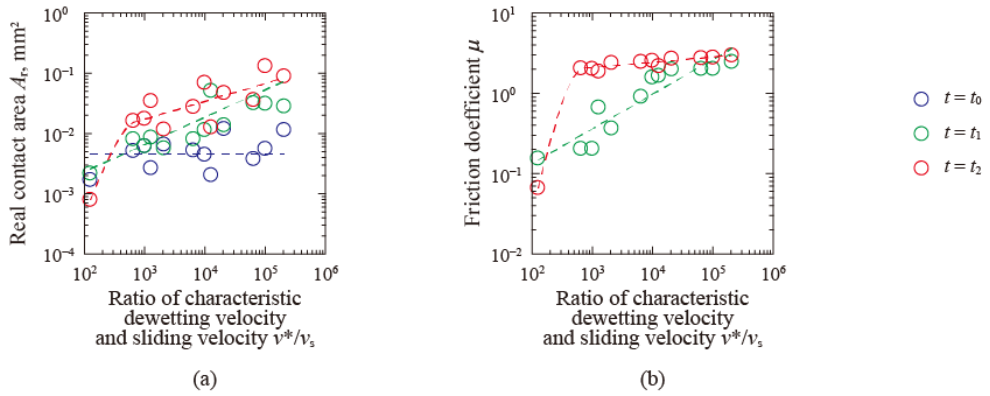

Fig. 4.12 Influence of v^*/v_s on A_r and μ at $10^{4.10} \leq v^*/v_c \leq 10^{4.31}$. [27]

friction coefficient μ at the three phases was confirmed. The influences of v^*/v_c and v^*/v_s ($v^* = |S|/\eta$.) were investigated to understand unforced dewetting and enforced wetting effects on real contact formation in contacting and sliding processes, and it was confirmed that the increase in v^*/v_c enlarged the real contact formation in the contacting process. Moreover, the effect of v^*/v_c was also confirmed even in the sliding process, but this effect decreased with sliding distance. In contrast, the real contact formation in the sliding processes was prompted by an increase in v^*/v_s instead of v^*/v_c. Furthermore, μ had a similar dependency on v^*/v_c and v^*/v_s because the adhesion term is proportional to A_r.

In conclusion, it is reasonable to control v^*/v_c and v^*/v_s to regulate A_r and μ during contacting and sliding processes to improve slip resistance of rubber items such as shoe soles, vehicle tires, floors, and handgrips.

References

[1] Strandberg L., “The Effect of Conditions Underfoot on Falling and Overexertion Accidents,” Ergonomics, 28, 1, 1985, 131–47.

[2] Grönqvist R., Roine J., Järvinen E., and Korhonen E., “An Apparatus and a Method for Determining the Slip Resistance of Shoes and Floors by Simulation of Human Foot Motions,” Ergonomics, 32, 8, 1989, 979–95.

[3] Kuwayama K., and Kimura Y., “Tribology in Water Tap,” Toraibarojisuto/Journal of Japanese Society of Tribologists, 54, 6, 2009, 389–93 (in Japanese).

[4] Bowden F.P., and Tabor D., “The Friction and Lubrication of Solids Part II,” Physics Today, 17, 6, 1964, 72.

[5] Moore D.F., “The Friction and Lubrication of Elastomers,” Pergamon Press, 1972.

[6] Moore D.F., and Geyer W., “A Review of Adhesion Theories for Elastomers,” Wear, 22, 2, 1972, 113–41.

[7] Moore D.F., and Geyer W., “A Review of Hysteresis Theories for Elastomers,” Wear, 30, 1, 1974, 1–34.

[8] Ramsay H.T., and Senneck C.R., “Anti-Slip Studs for Safety Footwear,” Applied Ergonomics, 3, 4, 1972, 219–23.

[9] Moore D.F., “The Friction of Pneumatic Tyres,” Elsevier Science Publishing Co. Inc., 1975.

[10] Stribeck R., “Die Wesentlichen Eigenschaften Der Gleit-Und Rollenlager,” Zeitschrift Des Vereines Deutscher Ingenieure, 46, 37, 1902, 1341–8.

[11] Nishi T., Moriyasu K., Harano K., and Nishiwaki T., Influence of dewettability on rubber friction properties with different surface roughness under water/ethanol/glycerol lubricated conditions. Tribol. Online, vol. 11, Japanese Society of Tribologists, 2016, p. 601–7.

[12] Roberts A.D., “Squeeze Films between Rubber and Glass,” Journal of Physics D: Applied Physics, 4, 3, 1971, 423–32.

[13] Roberts A.D., and Tabor D., “The Extrusion of Liquids between Highly Elastic Solids,” Proceedings of the Royal Society of London Series A, Mathematical and Physical Sciences, 325, 1562, 1971, 323–45.

[14] Brochard-Wyart F., and De Gennes P.G., “Dewetting of a Water Film between a Solid and a Rubber,” Journal of Physics: Condensed Matter, 6, 23A, 1994, A9–12.

[15] Martin P., Silberzan P., and Brochard-Wyart F., “Sessile Droplets at a Solid/Elastomer Interface,” Langmuir, 13, 18, 1997, 4910–4.

[16] Martin P., and Brochard-Wyart F., “Dewetting at Soft Interfaces,” Physical Review Letters, 80, 15, 1998, 3296–9.

[17] Martin A., Buguin A., and Brochard-Wyart F., “Dewetting Nucleation Centers at Soft Interfaces,” Langmuir, 17, 21, 2001, 6553–9.

[18] Martin A., Clain J., Buguin A., and Brochard-Wyart F., “Wetting Transitions at Soft, Sliding Interfaces,” Physical Review E - Statistical, Nonlinear, and Soft Matter Physics, 65, 3, 2002, 031605/1-031605/4.

[19] Martin A., Buguin A., and Brochard-Wyart F., “‘Čerenkov’ Dewetting at Soft Interfaces,” Europhysics Letters, 57, 4, 2002, 604–10.

[20] Nishi T., Moriyasu K., Harano K., and Nishiwaki T., “Influence of Surface Free Energy on Rubber Friction Properties under Water/Ethanol Lubrilated Conditions,” Toraibarojisuto/Journal of Japanese Society of Tribologists, 59, 11, 2014, 717–23 (in Japanese).

[21] Nishi T., “Influence of Lubricant Properties and Contacting Velocity on Real Contact Formation between Rubber and Glass in a Contact Process,” Tribology International, 127, 2018, 240–4.

[22] Nishi T., “Influence of Curvature Radius, Elastic Modulus, and Contact Velocity on Real Contact Formation between Rubber Hemisphere and Glass Plate during Contact Process under a Water-Lubricated Condition,” Tribology International, 130, 2019, 284–8.

[23] Shibata K., Warita I., Yamaguchi T., Hinoshita M., Sakauchi K., Matsukawa S., et al., “Effect of Groove Width and Depth and Urethane Coating on Slip Resistance of Vinyl Flooring Sheet in Glycerol Solution,” Tribiology International, 135, February, 2019, 89–95.

[24] Nishi T., Moriyasu K., and Nishiwaki T., “Precise Measurement of Clearance between Two Substrates Using Evanescent Waves,” Tribology Online, 12, 5, 2017, 251–6.

[25] Kaelble D.H., “Dispersion-Polar Surface Tension Properties of Organic Solids,” Journal of Adhesion, 2, 2, 1970, 66–81.

[26] Johnson K.L., Kendall K., and Roberts A.D., “Surface Energy and the Contact of Elastic Solids,” Proceedings of the Royal Society A: Mathematical, Physical and Engineering Sciences, 324, 1558, 1971, 301–13.

[27] Nishi T., Yamaguchi T., Shibata K., and Hokkirigawa K., “Influence of Unforced Dewetting and Enforced Wetting on Real Contact Formation and Friction Behavior between Rubber Hemisphere and Glass Plate during Contacting and Sliding Processes,” Tribology International, 141, 2020, 105921.

Chapter 5

Rubber friction with nonuniform wetting states: rubber with a hydrogel patch

5.1 Introduction

Soft materials such as jelly, agar, and contact lenses are categorized as hydrogels, which contain water. Interestingly, the friction coefficients (μ) of hydrogels, especially in water-lubricated conditions, are much smaller than that of rubber, although their elastic moduli (E) can be lower than that of rubber. Polyvinyl alcohol (PVA) hydrogel is a candidate material for artificial joints because of its high biocompatibility and very low μ in water and saline solutions [1–4]. While rubber is hydrophobic, hydrogels, which contain water, are hydrophilic. The lubricant wettability can be adjusted using the difference in the wettabilities of rubber and hydrogel [1,5]. In detail, the wettability at the triple line (the contact line of the lubricant and the substrates) is quantified as the spreading coefficient (S), whose value is calculated from their interfacial free energies [5]. At $S > 0$ mJ/m^2, the lubricant can flow at the interface between the substrates, and vice versa (the lubricant was is drained from the interface at $S < 0$ mJ/m^2) [6]. Because this phenomenon coincides with the strain in the substrate, the dewetting effect at $S < 0$ mJ/m^2 is remarkable when at least one of the substrates is a soft material [6]. The dewetting effect in rubber friction has been theoretically and experimentally studied [7-20], and it has been reported that A_r between a rubber hemisphere and a glass plate decreased with S during contact [7-12,16,17,21] and sliding [13-15,18-20]. Because of the proportional relationship between the adhesion term and A_r, μ also decreased with S [13-15,18-20]. While S is generally negative for rubber, the value of S is almost zero for hydrophilic materials, such as PVA hydrogel. Thus, the dewetting effect is very low for hydrogels, and such materials have low friction [1,5]. As mentioned in Chapters 3 and 4, real contact formation between a rubber hemisphere and a glass plate is determined

by the product of the characteristic dewetting velocity, v^* (the ratio of $|S|$ to the lubricant viscosity η), and time. Because the duration of dewetting is inversely proportional to the contacting velocity (v_c) and sliding velocity (v_s), A_r during contact and sliding can be determined by v^*/v_c and v^*/v_s. This theory, however, was developed assuming uniform wettability.

The dewetting behavior of soft materials when the distribution of wettability is nonuniform has not been reported, although it is expected that the wettability can be nonuniform between two substrates and that the contact condition and friction behavior differ from the case of uniform wettability. The purpose of this chapter was to investigate the influence of wettability distribution on the friction behavior of rubber on a glass plate under water-lubricated conditions. The wettability distribution was controlled by attaching a cross-linked PVA hydrogel patch at the bottom of a silicone rubber hemisphere.

5.2 Experimental methods

5.2.1 Preparation of silicone rubber hemisphere without/with a PVA hydrogel patch

A silicone rubber hemisphere with a PVA hydrogel patch was prepared based on a process shown in Fig. 5.1. First, to ensure highly reflected light in the total reflection method explained below, 10 wt.% PVA (Wako 1st grade 160-11485, FUJIFILM Wako Pure Chemical Corporation, Japan) aqueous solution with titanium oxide (10 vol.%, A150, Sakai Chemical Industry Co., Ltd., Japan) was prepared. As shown in Fig. 5.1(a), PVA aqueous solution with titanium oxide was chemically cross-linked using titanium bis(triethanolamine)diisopropoxide (ORGATIX TC-400, Matsumoto Fine Chemical Co., Ltd., Japan) at 25°C for 30 s and crushed at –196°C for 5 min with a freeze crusher (JFC-300, Japan Analytical Industry Co., Ltd., Japan). Secondly, as shown in Fig. 5.1(b), the surface of the cross-linked PVA hydrogel particles (53.2 mg) was chemically modified in a solution of triethoxyvinylsilane (0.210 mL, Tokyo Chemical Industry Co., Ltd., Japan) in toluene (10.0 mL, Wako 1st grade, FUJIFILM Wako Pure Chemical Corporation, Japan) at 80°C for 18 h. The chemical reaction between PVA and triethoxyvinylsilane is given in Eq. 5.1:

(5.1)

By rinsing in ethanol (Wako 1st grade, FUJIFILM Wako Pure Chemical Corporation, Japan) and ion-exchanged water three times, the reaction residue was removed. Consequently, by vacuum drying at 25°C and 33.9 kPa for 30 min using a vacuum pump (DAP-15, ULVAC KIKO. Inc., Japan), the solvent was eliminated. The chemically modified PVA particle was cut with a razor blade (FH-10, Feather Safety Razor Co., Ltd., Osaka, Japan) and placed in ion-exchanged water at 25°C for more than 24 h to ensure that the cross-linked PVA hydrogel particle had a partially untreated surface and contained water at equilibrium. Thirdly, as shown in Fig. 5.1(c), by setting the half-cut and cross-linked PVA hydrogel particle as the chemically untreated surface contacting with the center of a concave lens (S-SLB-10-15 N, SIGMAKOKI Co., Ltd., Japan), non-cross-linked silicone rubber and a cross-linking agent (polydimethylsiloxane, Sylgard 184, Dow Corning Toray Co., Ltd., Japan) with 10 vol.% titanium oxide and 20 wt.% inorganic fluorescent powder (black light powder blue, GP-PRO Co., Ltd., Japan) was poured into a mold and heated at 80°C for 90 min for the chemical reactions between the cross-linking agent and silicone rubber and between the cross-linking agent and chemically modified PVA to complete. The chemical reaction between the cross-linking agent and chemically modified PVA is shown in Eq. 5.2.

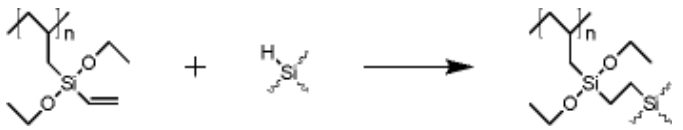

(5.2)

Finally, to ensure the saturation of water absorption in the cross-linked PVA hydrogel on the cured silicone rubber hemisphere, it was set in ion-exchanged water at 25°C for more than 24 h. Fig. 5.2 indicates the geometry of the hemispheres without and with one cross-linked PVA hydrogel patch. Hemispheres with different patch sizes (denoted by hydrogels #1–3) were prepared by selecting chemically modified PVA hydrogel particles with various diameters (~100 μm, ~200 μm, and >2000 μm), respectively. The hemisphere without a hydrogel was also prepared, as shown in Fig. 5.1(c), but

the PVA particle was not placed on the concave mold. Table 5.1 shows the geometric properties of rubber hemispheres measured using a one-shot 3D macroscope (VR3000, Keyence Corporation, Japan). Using the accompanying software (VR-H1A, Keyence Corporation, Japan), a plane correction was applied, and the arithmetical mean height (S_a) was calculated. To avoid shrinkage in PVA hydrogel, each specimen was placed in water just before the measurement, which was completed within 1 min. Here, the difference in curvature radii between the samples was approximately 1%. While the S_a values of the rubber without the hydrogel and that with hydrogel #1 were similar, it increased with the size of the PVA patch (hydrogels #1–3). Considering that the chemically untreated surface of the PVA hydrogel was rougher than the silicone rubber surface and that the E of the PVA patch was smaller than the silicone rubber, as listed in Table. 5.2, the effect of the increase in S_a among the rubbers with hydrogels #1–3 on their friction behaviors was negligible. The elastic modulus in Table 5.2 was measured by a dynamic viscoelastic measurement device (Reogel E4000, UBM Co., Ltd., Japan). The contact angle of a 1.0 μL-drop of ion-exchanged water and diiodomethane (Wako 1st grade, FUJIFILM Wako Pure Chemical Corporation, Japan) was measured on the silicone rubber, PVA hydrogel, and BK7 glass (084.4L100-45DEG-6P-4SH3.5, SIGMAKOKI Co., Ltd., Japan) using a contact angle meter (DMs-401, Kyowa Interface Science Co., Ltd., Japan), and the surface free energy among them and the values of S based on Kaelble and Uy theory were calculated [22]. As expected, the spreading coefficients for the silicone rubber (S_R) and PVA hydrogel (S_H) were $S_R << S_H \approx 0$ mJ/m^2.

Table 5.1 Geometry parameters of rubber hemispheres with/without a PVA hydrogel patch [28]

Rubber	Without hydrogel	With hydrogel #1	With hydrogel #2	With hydrogel #3
Curvature radius, mm	7.84	7.76	7.86	7.83
Arithmetical mean height S_a, μm	0.37	0.32	3.69	6.12
Horizontal PVA hydrogel size R_H, μm	-	≈ 100	≈ 200	>2000

Table 5.2 Physical properties of the silicone rubber, PVA hydrogel, and glass [28].

Rubber		Silicone rubber	PVA hydrogel	Glass
Elastic modulus (E), MPa		2.04	0.0333	-
Surface free energy, mJ/m^2	Dispersion	11.0	22.5	26.8
	Polar	1.7	46.6	24.7
	Total	12.7	69.1	51.5
Spreading coefficient contacting with the glass plate in water S, mJ/m^2		–24.0	–1.4	-

5.2.2 Friction testing and contact condition observation

Using the previously reported system [20], the friction forces and contact conditions during the sliding of SR hemispheres (rubbers without/with hydrogels #1–3) on the glass plate in ion-exchange water were investigated. During contact, the rubber hemisphere approached the water-covered glass plate at 0.10 mm/s, which was controlled using an electric cylinder (EASM4NXD010AZMC, Oriental Motor Co., Ltd., Japan). Immediately after contact, at least within 0.01 s, 0.0981 N was loaded on the rubber hemisphere, and the glass plate was horizontally slid at 0.10 mm/s using another electric cylinder (EACM4D30AZAC, Oriental Motor Co., Ltd., Japan). Here, the contact diameter and the nominal contact pressure (mean pressure) among rubber specimens were 0.947–0.950 mm and 0.138–0.139 MPa, respectively, calculated based on the Hertz contact theory assuming that the elastic modulus of the SR was dominant regardless of PVA attachment. A tribometer (TL201Ts, Trinity-Lab Inc., Japan) was used to measure the friction force. The sliding distance, sampling number, temperature, and relative humidity were set at 10.0 mm, 100 Hz, 24.6–25.5°C, and 68%–73%, respectively.

The distributions of real contacts, the interfacial gap e, and the PVA hydrogel between the rubber hemisphere and the glass plate during contact and sliding were measured using the optical system shown in Fig. 5.3. Based on light interferometry and the total reflection method, the distribution of real contacts and e were quantified, respectively, as previously reported [26]. In the total reflection method, red light from a light-emitting diode (LED, HLV2-22RD-3W, CCS Inc., Japan) was internally reflected in the glass plate by setting the incidence angle at 65° with a light guide (LE-OPT-24, OPTEC FA Co., Ltd.,

Japan) and a mirror (RPB3-20-550, SIGMAKOKI Co., Ltd., Japan). The red light on the interface between the rubber hemisphere and the glass plate was scattered and observed using a charge-coupled device (CCD) camera (AT-030MCL, JAI Ltd., Japan). In light interferometry, the same CCD camera observed the reflected green light from an LED (HLV2-22GR-3W, CCS Inc., Japan) through a telecentric lens (TV-2F-110, OPTART Co., Ltd., Japan). Because the inorganic powder in the SR absorbs UV light and emits blue light, the position of PVA hydrogel (orange area shown in Fig. 5.3) was determined by observing blue fluorescence excited by UV radiation from a UV LED

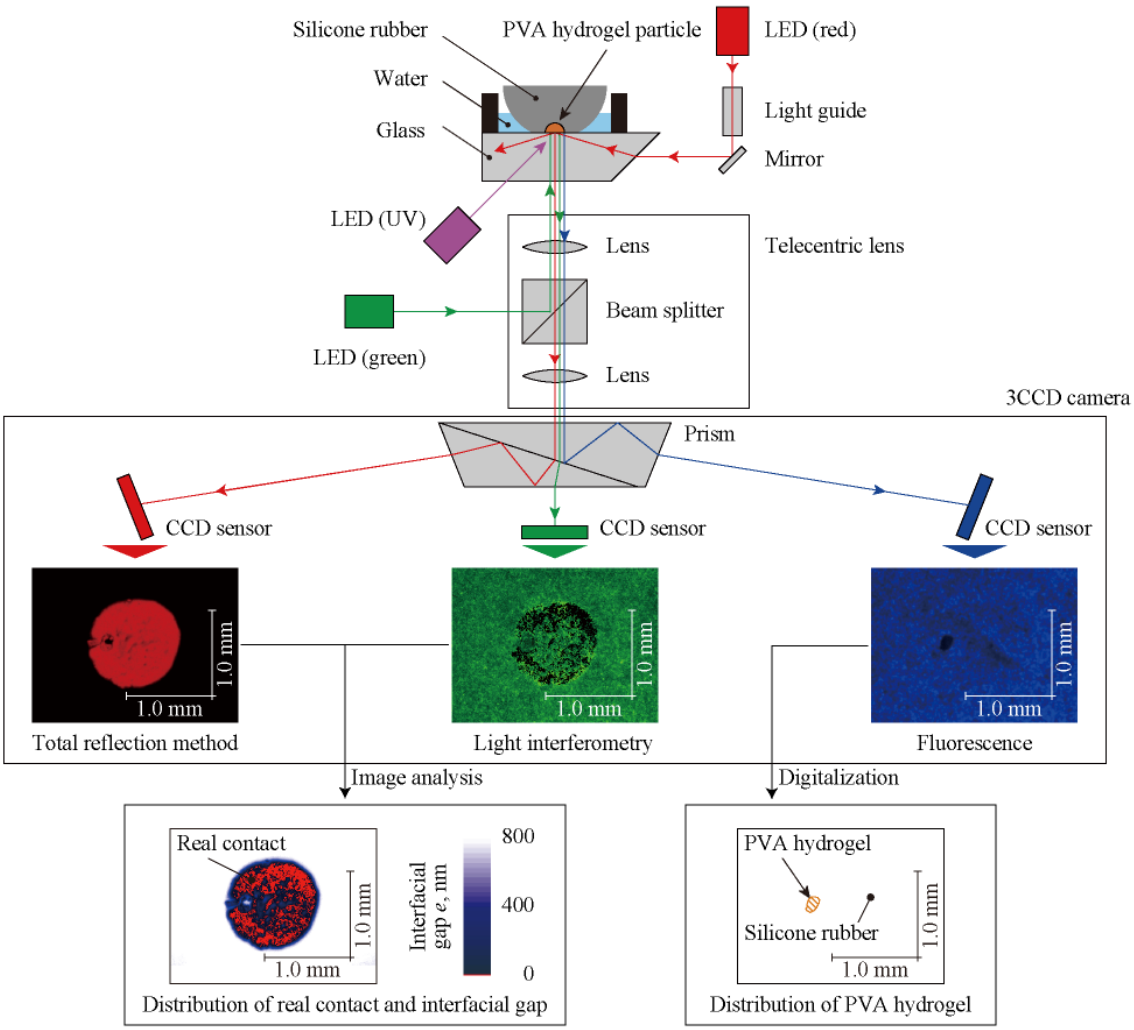

Fig. 5.3 Optical system to measure the distributions of real contact, interfacial gap *e*, and hydrogel between the rubber hemisphere with an attached hydrogel patch and a glass plate in the processes of contacting and sliding based on total reflection method, light interferometry, and fluorescence [28].

(HLV-24UV365-4WNRBTNJ, CCS Inc., Japan) and setting the threshold value in fluorescence images. Here, the camera had three CCDs for red, green, and blue lights; each intensity of light was individually measured on the same pixels. The pixel format, size, and sampling rate were set at 12-bit, 3.6 μm × 3.6 μm, and 100 Hz, respectively. The region with low intensity in light interferometry was defined as the real contact [23-25]. In addition, because the intensity in the total reflection method exponentially decreased with e, e was quantified based on its intensity [26]. The observations above were conducted when the siding distance (d) was within 5.0 mm. In this chapter, the average values of measured parameters at d = 0.00, 1.00, 2.00, 3.00, 4.00, and 5.00 mm (including the results of μ) were extracted and compared with each other.

5.3 Results

5.3.1 Contact conditions of the rubber hemispheres before and during the sliding

Fig. 5.4 shows the distributions of real contact, e, and hydrogel for all rubber hemispheres at d = 0.00 and 5.00 mm. The contact conditions just after the completion of the contact process and steady friction corresponded to d = 0.00 and 5.00 mm. The red and blue regions indicate real and non-real contact, respectively. The gradation in blue corresponds to the value of e. The shaded orange area in Figs. 5.4(b)–(d) indicates the hydrogel area. As expected, the presence of one hydrogel patch was confirmed in the apparent contact area for hydrogels #1 and #2, and hydrogel #3 covered the entire contact area. Regardless of rubber hemispheres, many real contacts were confirmed in the apparent contact area. For hydrogels #1 and #2 at d = 0.00 mm, the green shaded area in Fig. 5.4(b,c) indicates that real contacts were formed around the hydrogel, and few real contacts were formed on the hydrogel, except for the case of hydrogel #1 at d = 5.00 mm. On the other hand, in the steady friction (d = 5.00 mm), the real contacts were formed in the shape of a crescent moon around the hydrogel. It is considered that water flow from the front edge during the sliding peeled the real contacts, which were formed at d = 0.00 mm. Based on water distribution, e between the hydrogel and glass was larger than that between the rubber and glass. Considering $S_R < S_H \approx 0$ mJ/m^2, the dewetting effect was

smaller on the hydrogel, which would lead to large *e*. In addition, *e* increased with the hydrogel size,

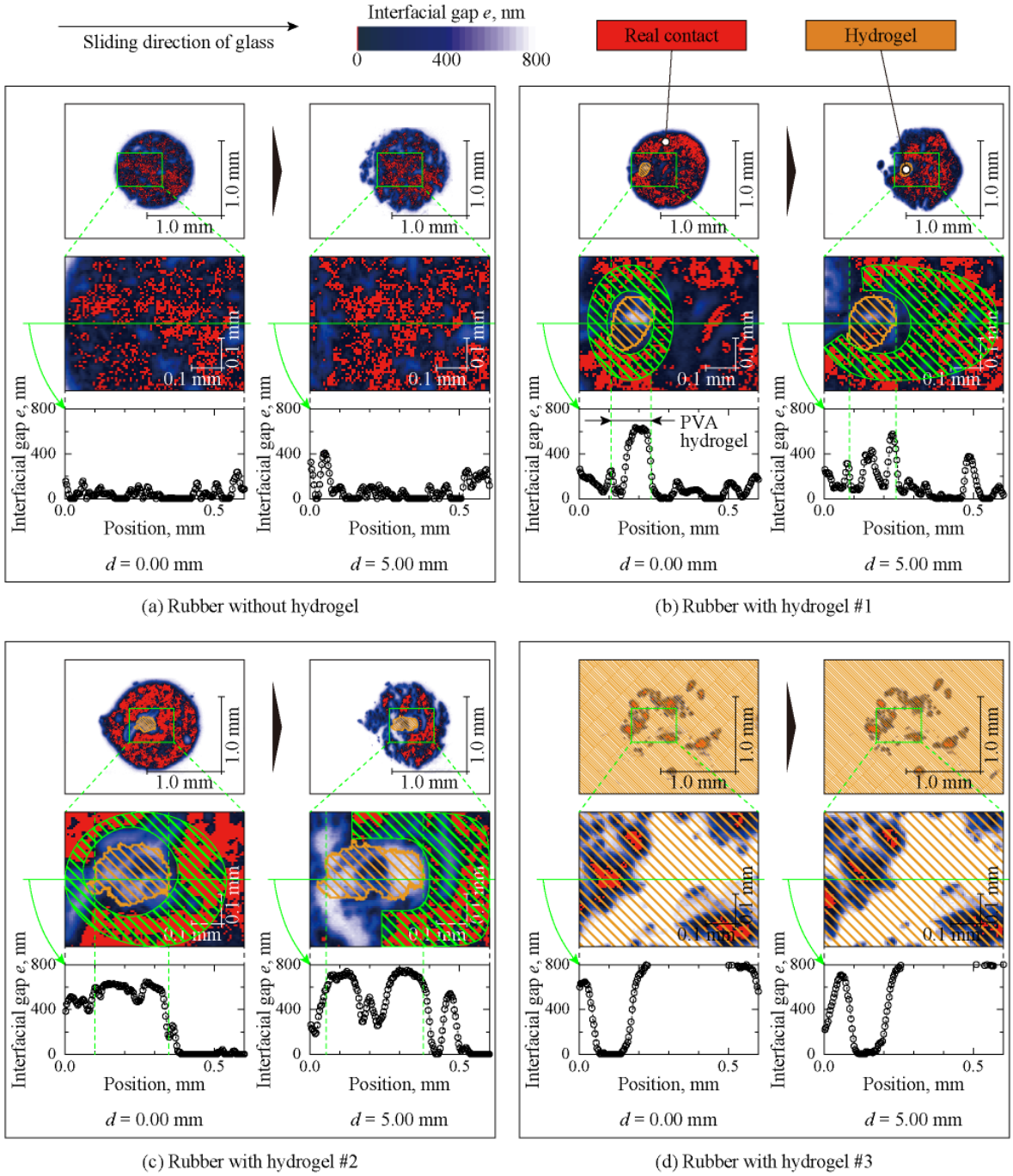

Fig. 5.4 Distributions of real contact, interfacial gap *e*, and PVA hydrogel at the rubber–glass interface for *d* = 0.00 and 5.00 mm. The red and blue areas indicate real and non-real contact, respectively. The orange areas in Figs. 4(b)–(d) indicate the distribution of the hydrogel. The green area in Figs. 4(b,c) indicate the ring/crescent-shaped real contact regions outside the hydrogel patch [28].

suggesting that the low dewetting effect on the hydrogel dominated with the increase in hydrogel size.

5.3.2 Real contact area A_r and friction coefficient μ for rubber without/with hydrogels

In Fig. 5.5, A_r and μ are plotted against d for the rubber without and with hydrogels #1–3. Regardless of rubber hemispheres, A_r and μ were in steady states at d > 2 mm. When the contact process was completed (d = 0.00 mm), A_r was the lowest for the rubber with hydrogel #3 but increased with the size of the hydrogel patch for other specimens. In the sliding process (d > 0.20 mm), A_r and μ were the highest for the rubber with hydrogel #1, but these parameters decreased with the size of the hydrogel patch. Only for the rubber with hydrogel #1 at d < 0.70 mm, the stick–slip behavior was observed. Fig. 5.6 shows the mean values and error bars of A_r and μ at d = 0.00, 1.00, 2.00, 3.00, 4.00, and 5.00 mm for all rubber specimens. The magnitude correlations of A_r and μ were the same as those in Fig. 5.5. Focusing on the results at d = 5.00 mm, the changes in A_r due to adding hydrogels #1–3 were +19.9% ± 2.8%, –10.0% ± 0.6%, –75.2% ± 6.4%, respectively, and the changes in μ at d = 5.00 mm were +23.2% ± 3.5%, –7.8% ± 2.4%, –82.8% ± 1.2%, respectively. Thus, adding the hydrogel patch on the rubber surface changed the real contact and friction behavior. Fig. 5.7 shows the relationship between A_r and μ at d = 1.00, 2.00, 3.00, 4.00, and 5.00 mm for all samples and indicates a proportional relationship between them. Because the adhesion term was proportional to A_r, the adhesion term was dominant. Therefore, the effect of hydrogels on real contact formation can shed

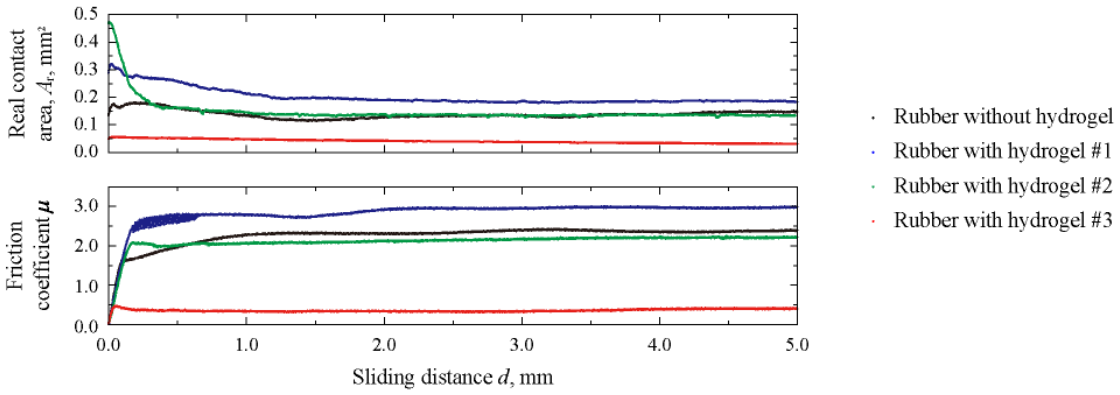

Fig. 5.5 A_r and μ plotted against the sliding distance d [28].

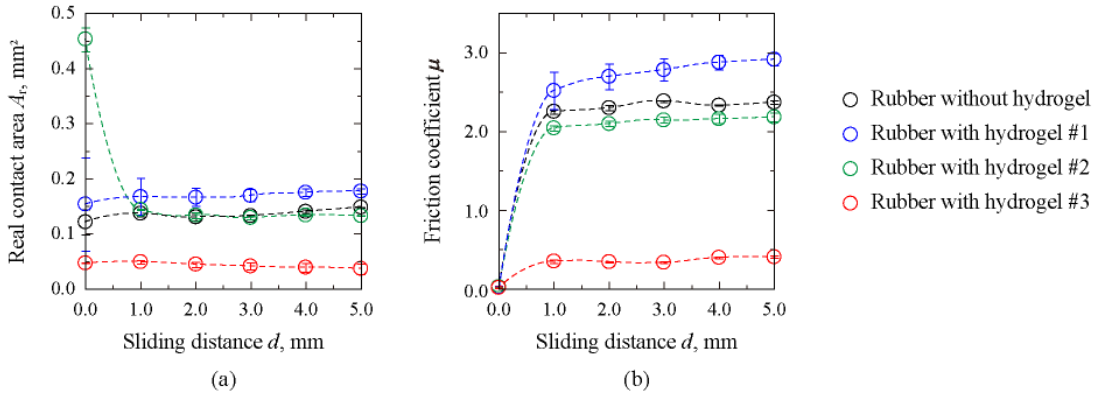

Fig. 5.6 Effect of d on the mean values of (a) A_r and (b) μ at d = 0.00, 1.00, 2.00, 3.00, 4.00, and 5.00 mm. The error bars indicate standard deviations. [28].

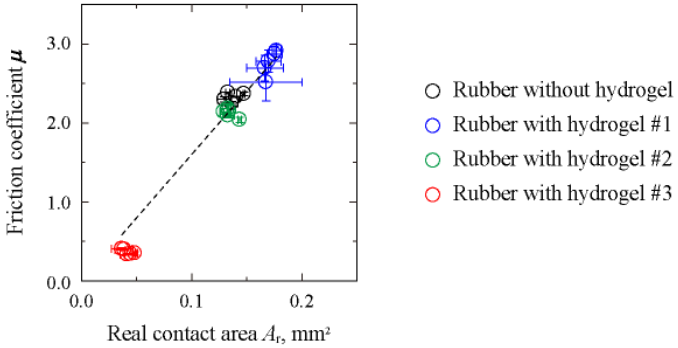

Fig. 5.7 Mean values of μ plotted against A_r at d = 1.00, 2.00, 3.00, 4.00, and 5.00 mm. The error bars indicate standard deviations. [28].

light on their effect on the friction behavior of rubber.

5.4 Discussion

5.4.1 Theory of dewetting in the case of uniform or nonuniform wetting

Regardless of lubricant existence, when soft material such as rubber makes contact with the floor, the real contact between the two surfaces can be thermodynamically enlarged for $S < 0$ (dewetting effect) [10]. In Fig. 5.8, the theoretical models of the dewetting effect for rubber without a hydrogel (uniform wetting), with hydrogel #1 or #2 (nonuniform wetting), and with hydrogel #3 (uniform wetting) are depicted. Because real contacts are seldom formed experimentally, no real contacts between the hydrogel and glass are assumed. The free energy of the system G for an interface with uniform wetting is given in Eq. 5.3 as the convex quadratic function of the size of real contact R

[10,11]:

$$G \sim -|S|R^2 + Ee^2R \tag{5.3}$$

The first and second terms are the changes in total surface free energy and strain energy, respectively. In this theory, only the strain in real contact formation is considered, and the strain as explained in the Hertz contact theory is not included [10.11]. The typical relationship between G and R for uniform wetting is shown in Fig. 5.9. Because G and the increasing rate of G are negative at $R > Ee^2/|S| = R_c$, the real contact is thermodynamically enlarged once R gets larger than R_c [10,11]. In contrast, because G is positive at $R < R_c$ and the maximum value of $G(R_c/2)$ is $E^2e^4/4|S|$, external energy is needed to form real contact whose R is larger than R_c. According to Eq. (5.3), G values for rubbers without and with hydrogel #3 are given in the following equations:

$$G \sim -|S_R|R^2 + E_Re^2R \tag{5.4}$$

$$G \sim -|S_H|R^2 + E_He^2R \tag{5.5}$$

The subscripts R and H indicate SR and hydrogel, respectively. Due to S_R = –24.0 mJ/m^2 << S_H = –1.4 mJ/m^2, the dewetting effect between the hydrogel and glass was much smaller than that between the

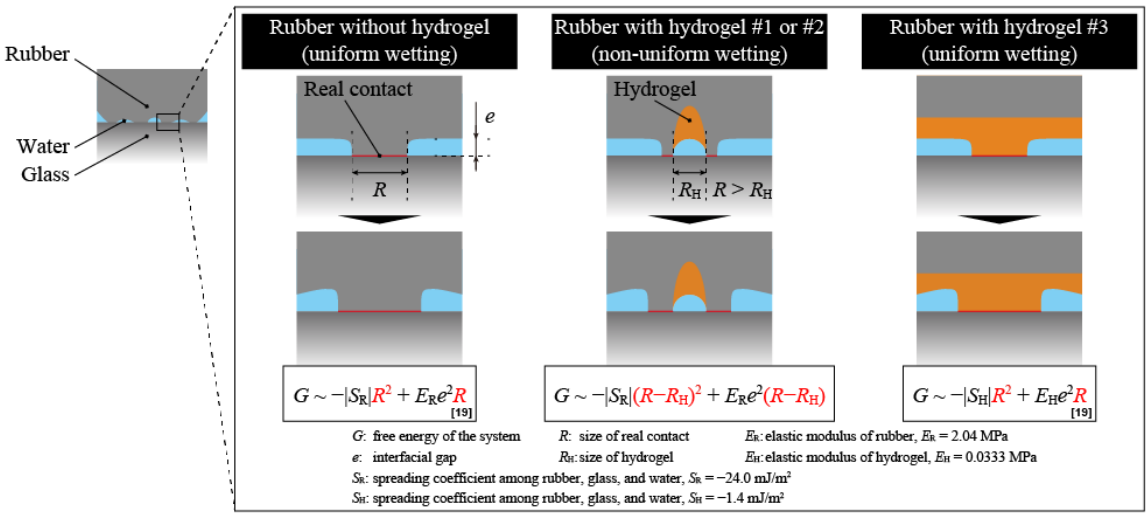

Fig. 5.8 Dewetting behavior models for uniform and nonuniform wettability distributions. Rubbers without a hydrogel and with hydrogel #3 demonstrate uniform wetting, while rubbers with hydrogel #1 and #2, nonuniform wetting [28].

silicone rubber and glass, suggesting that the strains in hydrogel #1 and #2 were negligible in comparison with that in the silicone rubber. Assuming no strain in the hydrogel for rubbers with hydrogel #1 and #2, $G = 0$ at $0 \leq R \leq R_H$, and G at $R > R_H$ can be calculated by

$$G \sim -|S_R|(R-R_H)^2 + E_R e^2 (R-R_H) \quad (5.6)$$

where R_H is the size of the hydrogel patch in Fig. 5.8. Eq. (5.6) explains that $G = 0$ at $0 \leq R \leq R_H$ and $G < 0$ at $R > R_c = R_H$; thus, the real contact formation was promoted with no activation energy for the rubbers with hydrogels #1 and #2.

5.4.2 Statistical definition of the critical interfacial gap (e_c)

Eqs. (5.4–5.6) explain that G is sensitive to e. According to a previous study of the dewetting behavior between an optically smooth rubber hemisphere and a glass plate, one real contact was surrounded by a rim, and e was constant outside the rim [11]. Although the surface was not optically smooth, Chudak et al. reported that e at an apparent contact area was almost constant during dewetting [21]. In this chapter, the measured area (1.80 mm × 2.40 mm) included not only the apparent contact area but also the area outside of the apparent contact area. Because the maximum measurable range of e was 800 nm, a peak at 800 nm, which corresponds to e around and outside the apparent contact area, and another peak at e < 800 nm, which corresponds to e within the apparent contact area, is expected in the histogram of e. As shown in Fig. 5.10, the experimentally measured histogram of e for all

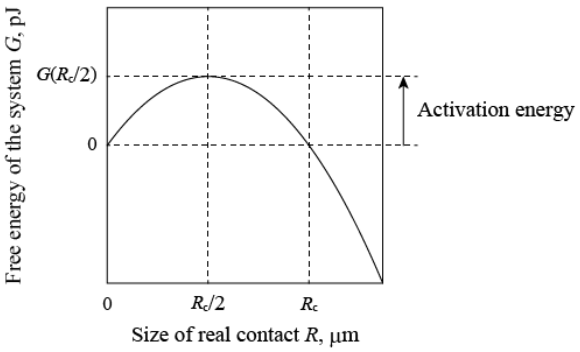

Fig. 5.9 Theoretical G–R curve for uniform wetting. $G(R_c/2)$ is equivalent to the activation energy of real contact formation [28].

rubbers at d = 5.00 mm was bimodal. Here, the critical interfacial gap e_c (e on the apparent contact area) was defined as the peak value of e (< 800 nm) based on minimizing the sum of squared residuals between the measured and calculated probability around the peak at e < 800 nm (not including the histogram around the peak at e = 800 nm) using the Solver add-in for Microsoft Excel (Microsoft Excel 2016, Microsoft Corporation, USA). Fig. 5.11 shows e_c for each rubber at d = 0.00, 1.00, 2.00, 3.00, 4.00, and 5.00 mm and indicates that e_c for the rubber with hydrogel #3 was constant and higher than those of the other rubbers. Except for the rubber with hydrogel #3, e_c increased with d and got saturated. It is considered that e_c initially increased with water inflow during sliding and that the contact condition reached an equilibrium point. Based on the differences between rubbers, e_c decreased with the addition of hydrogel patches but increased with the hydrogel size.

5.4.3 Theoretical estimation of the free energy of the system (G)

As discussed above, thermodynamically expansion of real contact (dewetting effect) occurs if $R > R_c$, and the activation energy $G(R_c/2)$ is needed to achieve the precondition $R > R_c$. The decreasing rate of G at $R > R_c$ is also important for triggering the dewetting effect. In addition, the roughness of the two substrates must be considered. However, considering that the initial real contacts are mainly formed by physical contact, as explained in the Hertz contact theory, and that the potential of the

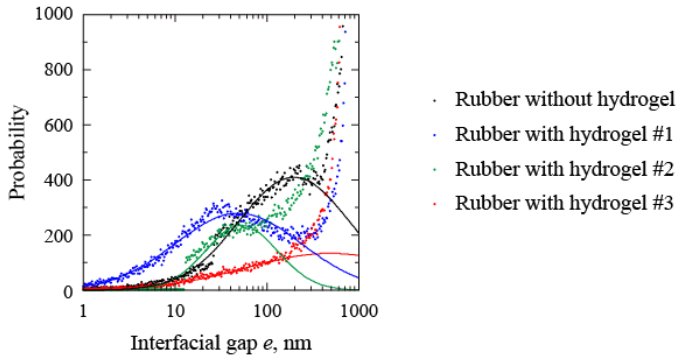

Fig. 5.10 Histograms of the interfacial gap e for all rubbers at d = 5.00 mm. The peak at e = 800 nm corresponded to the interfacial gap around and outside the apparent contact area, and the peak at e < 800 nm corresponded to the mean interfacial gap at the apparent contact area [28].

dewetting effect of each real contact depends on its size (R), more real contacts can be generated as R_c decreases [10,11]. Thus, the dewetting effect is mainly determined by R_c rather than the activation energy and the value of the decreasing rate of G. Fig. 5.12(a) shows G at d = 5.00 mm, which was calculated based on Eqs. (5.4–5.6). A magnified view of Fig. 5.12(a) is shown in Fig 5.12(b). It was confirmed that G = 0 pJ at R = 0 μm for all rubbers and that G increased at $R \leq R_c/2$ and decreased at $R > R_c/2$ for uniform wetting. For the rubber without a hydrogel, the activation energy $G(R_c/2)$ and the decreasing rate of G at $R = R_c$ were higher, but R_c was lower than that of the rubber with hydrogel #3. Due to the smaller value of Rc for the rubber without a hydrogel, A_r at d = 5.00 mm was experimentally higher than the rubber with hydrogel #3. Fig. 5.12 also indicates that G = 0 pJ at $R < R_c = R_H$ for the rubbers with hydrogels #1 and #2 (nonuniform wetting), which explains activation energy is not needed to trigger the dewetting effect for these conditions. Although the size of the hydrogel patch can change during contact and sliding, we assumed that the sizes of hydrogels #1 and #2 were constant. Here, experimentally and theoretically, real contacts between the hydrogel patch and glass were not formed, which corresponded to no activation energy in G–R curves for these nonuniform wetting situations. Thus, all real contacts initially formed between two substrates can be thermodynamically enlarged by the dewetting effect. In addition, the decreasing rate of G at $R = R_c$ was larger than that for uniform wetting, which also promoted the dewetting effect. In other words, by

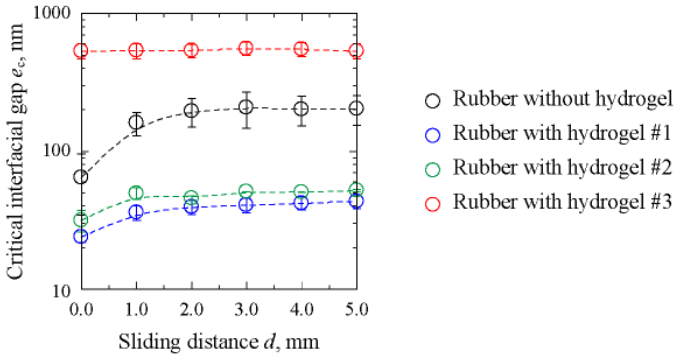

Fig. 5.11 Critical interfacial gap e_c plotted against the sliding distance d. The error bars indicate standard deviations. [28].

adding a small hydrogel patch on the rubber surface, real contact can be formed around the hydrogel in the shape of a ring without requiring activation energy.

Because there were no real contacts between the hydrogel patch and glass for rubbers with hydrogels #1 and #2, it is reasonable to compare the dewetting effect using G–A_r curves rather than G–R curves. Fig. 5.13(a) shows the G–A_r curves at d = 5.00 mm for all rubbers, where A_r was defined as R^2 for uniform wetting and $(R–R_H)^2$ for nonuniform wetting. Fig. 5.13(b) shows the magnified view of Fig. 5.13(a) for uniform wetting. In the case of uniform wetting (rubbers without a hydrogel and with hydrogel #3), G–A_r curves also had a positive peak, as well as G–R curves in Fig. 5.12, due to the activation energy of dewetting, and G got negative at $A_r > R_c^2$. For nonuniform wetting (rubbers with hydrogel #1 and #2), G was constantly negative, and the decreasing rates of G were higher than those

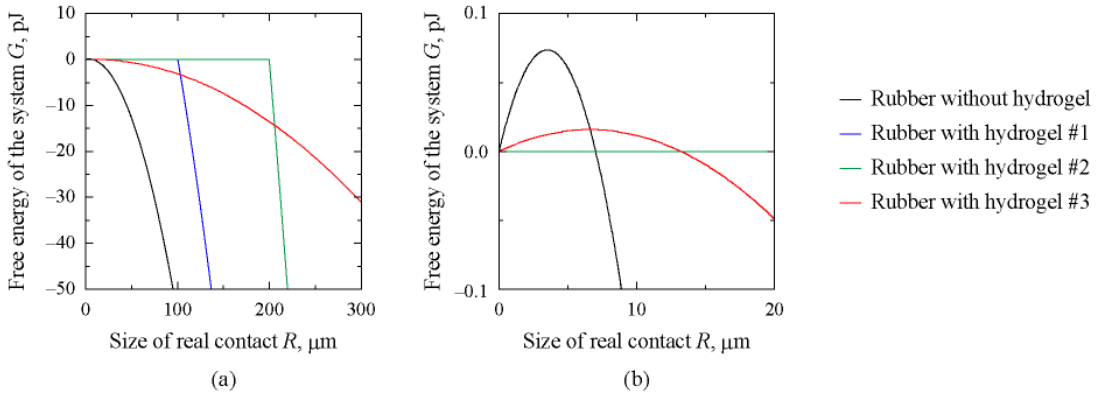

Fig. 5.12 Estimated G–R curves at d = 5.00 mm during dewetting: (b) a magnified view of (a) [28].

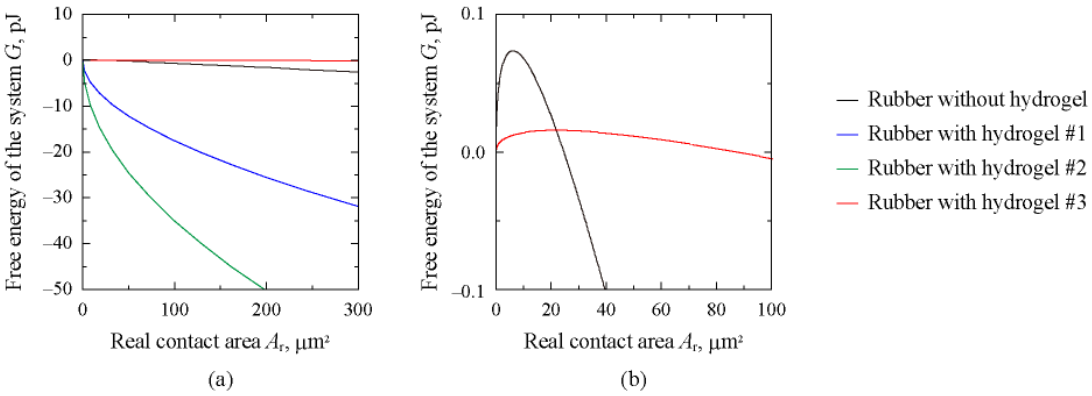

Fig. 5.13 Estimated G plotted against the real contact area A_r for all rubbers at d = 5.00 mm: (b) a magnified view of (a) [28].

for uniform wetting, especially for the rubber with hydrogel #2. These results also indicate that the real contact formation is promoted for nonuniform wetting. However, as the hydrogel patch size increases, the influence of roughness and periodicity on real contact formation dominates. In addition, the hydrogel area cannot contribute to the enlargement of A_r due to the poor dewetting effect between the hydrogel patch and glass. Thus, an optimum hydrogel size exists to maximize A_r and μ. Considering the elastohydrodynamic lubrication theory [27], e_c may also be sensitive to the normal force, sliding velocity, curvature radius, and surface roughness. Therefore, the optimum hydrogel size to achieve high friction depends on these parameters.

5.5 Conclusions

SR hemispheres without a hydrogel and with various sizes of chemically cross-linked PVA hydrogel patches were prepared. By measuring their contact conditions and friction behaviors on a glass plate in a water-lubricated condition, the following conclusions were drawn:

The addition of the 100-μm hydrogel patch increased A_r and μ by 19.9% ± 2.8% and 23.2% ± 3.5%, respectively, at d = 5.00 mm. However, with the addition of the 200-μm hydrogel patch, A_r and μ decreased by 10.0% ± 0.6% and 7.8% ± 2.4%, respectively, at d = 5.00 mm. In addition, when the contact area was completely covered with the hydrogel patch, A_r and μ decreased by 75.2% ± 6.4% and 82.8% ± 1.2%, respectively. The adhesion term was dominant due to the potential relationship between μ and A_r. To understand the effect of the hydrogel patch on friction, we developed a theory of the dewetting effect for uniform wetting and showed that adding a hydrogel patch on the rubber surface promoted real contact formation and led to high friction. As confirmed by the experimental results, our theory also indicated that an optimal size of the hydrogel patch can be used to maximize A_r and μ.

Due to the low friction of hydrogels in water [1-4], the larger hydrogel patch produces lower friction. In this work, however, the experimental and theoretical results suggest that high-friction rubber in water can be achieved by optimizing the hydrogel size on the rubber surface. These findings

provide new insights into designing soft materials with high slip resistance.

References

[1] Ratner B.D., and Hoffman A.S., Synthetic Hydrogels for Biomedical Applications. Hydrogels Med. Relat. Appl., vol. 31, AMERICAN CHEMICAL SOCIETY, 1976, p. 1.

[2] Murakami T., Sawae Y., Higaki H., Ohtsuki N., and Moriyama S., The Adaptive Multimode Lubrication in Knee Prostheses with Artificial Cartilage during Walking. In: Dowson D, Taylor CM, Childs THC, Dalmaz G, Berthier Y, Flamand L, et al., editors. Elastohydrodyn. - '96 Fundam. Appl. Lubr. Tract., vol. 32, Elsevier, 1997, p. 371–82.

[3] Sardinha V.M., Lima L.L., Belangero W.D., Zavaglia C.A., Bavaresco V.P., and Gomes J.R., "Tribological Characterization of Polyvinyl Alcohol Hydrogel as Substitute of Articular Cartilage," Wear, 301, 1–2, 2013, 218–25.

[4] Murakami T., Sakai N., Yamaguchi T., Yarimitsu S., Nakashima K., Sawae Y., et al., "Evaluation of a Superior Lubrication Mechanism with Biphasic Hydrogels for Artificial Cartilage," Tribology International, 89, 2015, 19–26.

[5] Nishi T., "Effects of Wettability on Tribology of Soft Matter," Toraibarojisuto/Journal of Japanese Society of Tribologists, 64, 10, 2019, 588–93 (in Japanese).

[6] de Gennes P.-G., Brochard-Wyart F., and Quéré D., Special Interfaces. Capillarity Wetting Phenom. Drops, Bubbles, Pearls, Waves, New York, NY, Springer New York, 2004, p. 215–59.

[7] Roberts A.D., "Squeeze Films between Rubber and Glass," Journal of Physics D: Applied Physics, 4, 3, 1971, 423–32.

[8] Roberts A.D., and Tabor D., "The Extrusion of Liquids between Highly Elastic Solids," Proceedings of the Royal Society of London Series A, Mathematical and Physical Sciences, 325, 1562, 1971, 323–45.

[9] Brochard-Wyart F., and De Gennes P.G., "Dewetting of a Water Film between a Solid and a Rubber," Journal of Physics Condensed Matter, 4, 10, 1994, 1727–35.

[10] Martin P., Silberzan P., and Brochard-Wyart F., “Sessile Droplets at a Solid/Elastomer Interface,” Langmuir, 13, 18, 1997, 4910–4.

[11] Martin P., and Brochard-Wyart F., “Dewetting at Soft Interfaces,” Physical Review Letters, 80, 15, 1998, 3296–9.

[12] Martin A., Buguin A., and Brochard-Wyart F., “Dewetting Nucleation Centers at Soft Interfaces,” Langmuir, 17, 21, 2001, 6553–9.

[13] Martin A., Clain J., Buguin A., and Brochard-Wyart F., “Wetting Transitions at Soft, Sliding Interfaces,” Physical Review E - Statistical, Nonlinear, and Soft Matter Physics, 65, 3, 2002, 031605/1-031605/4.

[14] Martin A., Buguin A., and Brochard-Wyart F., “‘Čerenkov’ Dewetting at Soft Interfaces,” Europhysics Letters, 57, 4, 2002, 604–10.

[15] Momozono S., Iguchi Y., Oshikiri K., Nakamura K., and Kyogoku K., Effects of interfacial free energy on adhesive friction behavior of elastomer surfaces under wet conditions. 5th World Tribol. Congr., vol. 4, 2013, p. 3208–11.

[16] Nishi T., “Influence of Lubricant Properties and Contacting Velocity on Real Contact Formation between Rubber and Glass in a Contact Process,” Tribology International, 127, 2018, 240–4.

[17] Nishi T., “Influence of Curvature Radius, Elastic Modulus, and Contact Velocity on Real Contact Formation between Rubber Hemisphere and Glass Plate during Contact Process under a Water-Lubricated Condition,” Tribology International, 130, 2019, 284–8.

[18] Nishi T., Moriyasu K., Harano K., and Nishiwaki T., “Influence of Surface Free Energy on Rubber Friction Properties under Water/Ethanol Lubrilated Conditions,” Tribologists, 59, 11, 2014, 41–7 (in Japanese).

[19] Nishi T., Moriyasu K., Harano K., and Nishiwaki T., Influence of dewettability on rubber friction properties with different surface roughness under water/ethanol/glycerol lubricated

conditions. Tribol. Online, vol. 11, Japanese Society of Tribologists, 2016, p. 601–7.

[20] Nishi T., Yamaguchi T., Shibata K., and Hokkirigawa K., "Influence of Unforced Dewetting and Enforced Wetting on Real Contact Formation and Friction Behavior between Rubber Hemisphere and Glass Plate during Contacting and Sliding Processes," Tribology International, 141, 2020, 105921.

[21] Chudak M., Kwaks J.S., Snoeijer J.H., and Darhuber A.A., "Non-Axisymmetric Elastohydrodynamic Solid-Liquid-Solid Dewetting: Experiments and Numerical Modelling," European Physical Journal E, 43, 1, 2020, 1–11.

[22] Kaelble D.H., "Dispersion-Polar Surface Tension Properties of Organic Solids," Journal of Adhesion, 2, 2, 1970, 66–81.

[23] Eguchi M., Shibamiya T., and Yamamoto T., "Measurement of Real Contact Area and Analysis of Stick/Slip Region," Tribology International, 42, 11–12, 2009, 1781–91.

[24] Eguchi M., "Statistical Measurement of Real Contact Area on the Basis of Image Intensity Histograms (Part 1) -Using Gaussian Distribution of Light Interference Image-," Toraibarojisuto/Journal of Japanese Society of Tribologists, 57, 5, 2012, 345–52 (in Japanese).

[25] Eguchi M., Hirayanagi T., and Miyoshi T., "Statistical Measurement of Real Contact Area on the Basis of Image Intensity Histograms (Part 2) -Application to Paper-Based Wet Friction Materials-," Toraibarojisuto/Journal of Japanese Society of Tribologists, 57, 5, 2012, 353–60 (in Japanese).

[26] Nishi T., Moriyasu K., and Nishiwaki T., "Precise Measurement of Clearance between Two Substrates Using Evanescent Waves," Tribology Online, 12, 5, 2017, 251–6.

[27] Hamrock B.J., and Dowson D., "Ball Bearing Lubrication: The Elastohydrodynamics of Elliptical Contacts," Wiley, 1981.

[28] Nishi T., Yamaguchi T., Shibata K., and Hokkirigawa K., "Optimizing the Frictional Behavior of Partially Wetting Soft Contacts as Measured with Hydrogel Covered Silicones," Tribology

International, 153, 2021, 106586.

Chapter 6

Rubber friction with nonuniform wetting states: air bubbles in water and water droplets in air

6.1 Introduction

Real contacts between two substrates are formed due to physical contact, as explained in the Hertz contact theory. However, when a soft material such as rubber contacts the floor, real contacts are formed and thermodynamically expanded, while the lubricant is dewetted [1–3]. Real contact formation in contact [3–11] and sliding processes [12–17] and the friction behavior [12–21] are related to the dewetting effect, which is theoretically explained based on wettability. Additionally, as mentioned in Chapter 5, the dewetting effect can be promoted using a hydrophilic patch (PVA hydrogel) on silicone rubber to form a nonuniform wetting state, which leads to a large real contact area and high friction.

As air and water are hydrophobic and hydrophilic materials, respectively, if they coexist between the two substrates (interface containing water droplets in air or air bubbles in water), they form an extremely nonuniform wetting state, and thus, high friction is expected. The purpose of this chapter was to investigate the influence of nonuniform wetting on real contact formation and the friction behavior at the interface between a silicone rubber hemisphere and a glass plate. To ensure such an extreme nonuniform wetting state in air and water, a piece of moist PVA hydrogel particle (patch) or a cavity filled with air was located at the bottom of the rubber hemisphere. The distributions of the real contact, water, and air between the substrates were optically measured under unlubricated and water-lubricated conditions at different sliding velocities (v).

6.2 Experimental methods

6.2.1 Preparation of silicone rubber hemispheres

Fig. 6.1 shows the three types of rubber hemispheres used in this chapter: untreated rubber, rubber with a hydrogel, and rubber with an air pocket. To prepare the untreated rubber, silicone rubber (polydimethylsiloxane, Sylgard 184, Dow Corning Toray Co., Ltd., Tokyo, Japan) containing 10 vol.% titanium oxide (A150, Sakai Chemical Industry Co., Ltd., Osaka, Japan) and 20 wt.% inorganic fluorescent powder (fluorescent black light powder blue, GP-PRO Co., Ltd., Kanagawa, Japan) were molded in a concave lens (S-SLB-10-15 N, SIGMAKOKI Co., Ltd., Saitama, Japan) at 80°C for 90 min. By adding titanium oxide, highly reflected light in the total reflection method and light interferometry was ensured (Fig. 6.2(a)). By adding the inorganic fluorescent powder, which absorbs

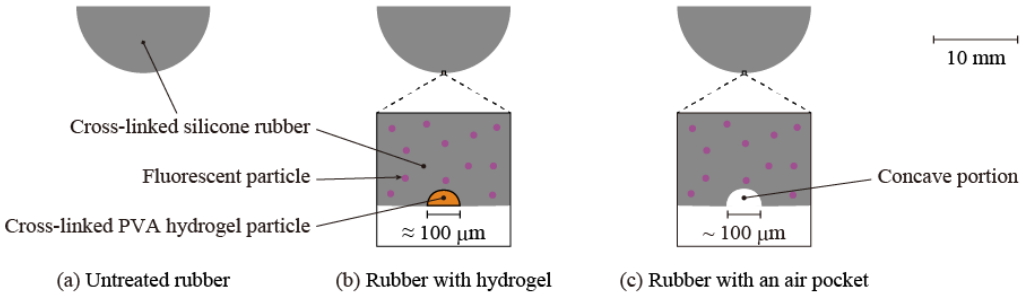

Fig. 6.1 Schematic of the cross sections of rubber hemispheres [30].

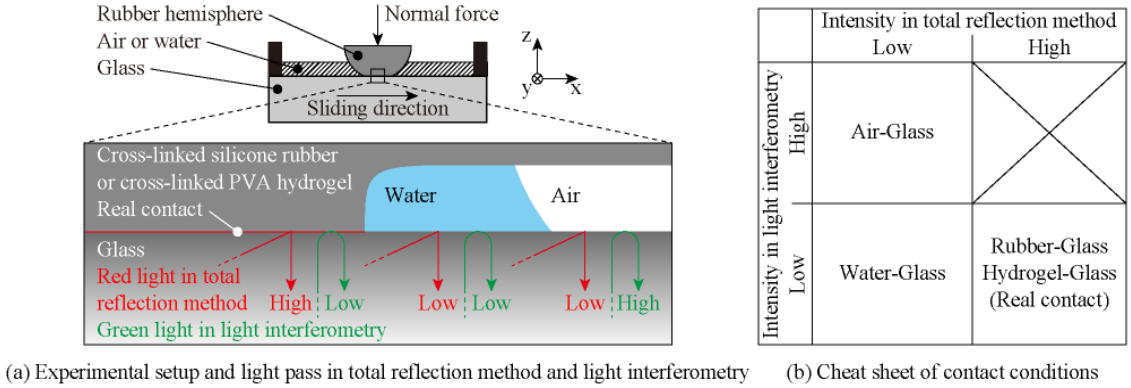

Fig. 6.2 Light paths in the experimental system for observing contact in the total reflection method and light interferometry, and a diagram for determining contact based on intensities in the total reflection method and light interferometry [30].

ultraviolet (UV) light and emits blue light, the rubber region was visualized. As shown in Fig. 6.1(b), for the rubber with a hydrogel hemisphere, a piece of PVA hydrogel was set at the bottom of the rubber hemisphere, as reported previously [17]. A cavity at the bottom of the rubber with an air pocket hemisphere was prepared by setting a cube of sodium chloride (Nakuru M, Naikai Salt Industries Co., Ltd., Okayama, Japan) with dimensions 100 μm × 100 μm × 100 μm at the bottom of the concave lens in the cross-linking process (Fig. 6.1(c)). The inflow of non-cross-linked silicone rubber into the interface between the sodium chloride block and the concave lens was prevented using a small amount of ethylene glycol (Wako special grade, FUJIFILM Wako Pure Chemical Corporation, Osaka, Japan). Sodium chloride and ethylene glycol were removed by immersion in ion-exchanged water at 25°C for more than 10 min after the completion of the cross-linking reaction in silicone rubber.

Table 6.1 shows the geometric properties of the rubber hemispheres measured by a one-shot 3D measuring macroscope (VR3000, Keyence Corporation, Osaka, Japan). To ensure that the hydrogel contained water at an equilibrium state, the rubber with the hydrogel hemisphere was placed in ion-exchanged water for an extended period prior to measurement. Based on the sectional view including the bottom of the hemisphere, the curvature radius was determined. The arithmetical mean height (S_a) was quantified by extracting an area of 1.000 mm^2. Here S_a for the rubber with an air pocket was determined from the 1.000 mm^2 geometry without the cavity. Table 6.1 shows that the values of the curvature radius and S_a were similar for all the rubber hemispheres.

Table 6.1 Geometrical parameters of rubber hemispheres [30]

Rubber	Untreated rubber	Rubber with hydrogel	Rubber with an air pocket
Curvature radius, mm	7.84	7.76	7.77
Arithmetical mean height S_a, μm	0.37	0.32	0.28
Horizontal size of PVA hydrogel R_H or air pocket R_A, μm	-	~100	~100

6.2.2 Friction testing

In this chapter, each rubber specimen was perpendicularly approached to a BK7 glass plate (084.4L100-45DEG-6P-4SH3.5, SIGMAKOKI Co., Ltd., Saitama, Japan) at 0.10 mm/s, and within 0.01 s after completion of contact, the normal force (deadweight) was set at 0.0981 N, and the glass plate horizontally slid at a sliding velocity v = 0.10, 1.00, or 10.00 mm/s. This friction test was conducted for unlubricated and water-lubricated (with 5.0 mL ion-exchanged water on the glass surface) conditions. For the rubber with a hydrogel patch in the unlubricated condition, the friction behavior is expected to depend on water inclusion in the hydrogel. Thus, the friction test for the rubber with a hydrogel patch in the unlubricated condition was conducted for two situations: immediately after immersing the hemisphere in ion-exchanged water (water on the rubber surface was wiped with paper (PROWIPE Soft Micro Wiper SS250, Daio Paper Corporation, Tokyo, Japan) before the friction test) and after drying in air at 25 °C for 1 day. The friction force was measured using a tribometer (TL201Ts, Trinity-Lab Inc., Tokyo, Japan), and the sliding distance (d), sampling number, temperature, and humidity were set at 10.0 mm, three times per condition, 24.3–25.5°C, and 68%–76% relative humidity, respectively.

6.2.3 Contact condition observation

The distributions of real contact and interfacial gap (e) were quantified using the total reflection method and light interferometry [10,11,16,17,22]. Red and green light were used in the total reflection method and light interferometry, respectively. The inorganic fluorescent powder in silicone rubber was excited by UV radiation, and the area where blue fluorescence was low was determined as the region of the hydrogel patch [17]. All light was observed at d = 0.00–5.00 mm using a charge-coupled device camera (AT-030MCL, JAI Ltd., Copenhagen, Denmark), whose pixel format, pixel size, and shutter speed were set at 12 bit, 3.6 μm × 3.6 μm, and 100 fps, respectively. Fig. 6.2(a) shows the light paths for real contact (rubber–glass or hydrogel–glass interfaces) and non-real contact (water–glass and air–glass interfaces) in the total reflection method and light interferometry. The light intensity in the

total reflection method (I_R) is high at real contacts (rubber–and hydrogel–glass interfaces) and decreases with e based on the decay behavior of the evanescent field [22,23]. Further, the light intensity in light interferometry (I_G) is the lowest at real contacts, gets slightly higher at water–glass interfaces, and gets substantially higher at air–glass interfaces [24–26]. The reorganization of the I_G gap between real and non-real contacts (water–glass interfaces) is technologically difficult [26], but these contact conditions can be identified, considering that I_R is high for a real contact and low for a non-real contact [22]. Fig. 6.3 shows the observed images and spectra of I_R, I_G, and the fluorescence intensity (I_B) for the rubber with a hydrogel hemisphere (moist) under the unlubricated condition at v = 1.00 mm/s and d = 5.00 mm. In this chapter, the regions where $I_R > I_{R0} - 3\sigma_{R0}$ and $I_G < I_{G0} + 3\sigma_{G0}$ were defined as real contacts [22]. Because the peak with low intensity in fluorescence (I_{B0}) in Fig. 6.3(c) corresponded to the hydrogel region, the region where $I_B < I_{B0} + 3\sigma_{B0}$ was defined as the hydrogel region. Here, σ_{R0}, σ_{G0}, and σ_{B0} indicate the standard deviations of the peaks. As shown in Fig. 6.2(b), the regions where $I_R \leq I_{R0} - 3\sigma_{R0}$ were categorized into water–glass and air–glass interfaces if I_G was lower and higher than $I_{G0} + 3\sigma_{G0}$, respectively.

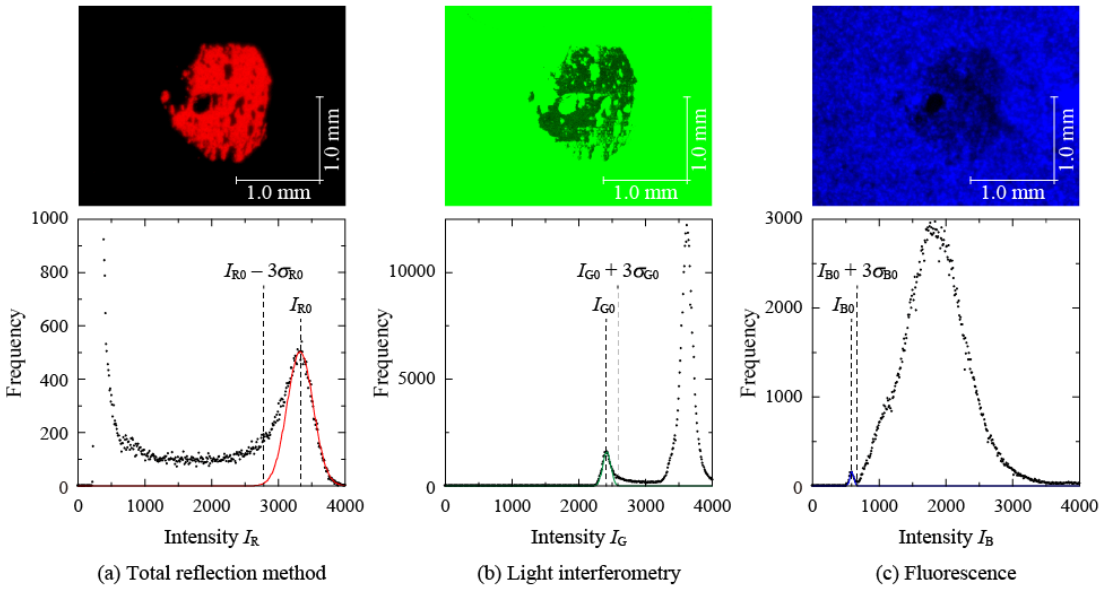

Fig. 6.3 Intensity spectra at the interface between the rubber with a hydrogel hemisphere (moist) and the glass plate at v = 1.00 mm and d = 5.00 mm: (a) red light in the total reflection method, (b) green light in light interferometry, and (c) blue light in fluorescence [30].

6.3 Results

6.3.1 Contact conditions

Fig. 6.4 shows the distributions of the real contact, water, and air under the unlubricated condition for the untreated rubber, rubber with a hydrogel patch (moist and dried), and rubber with an

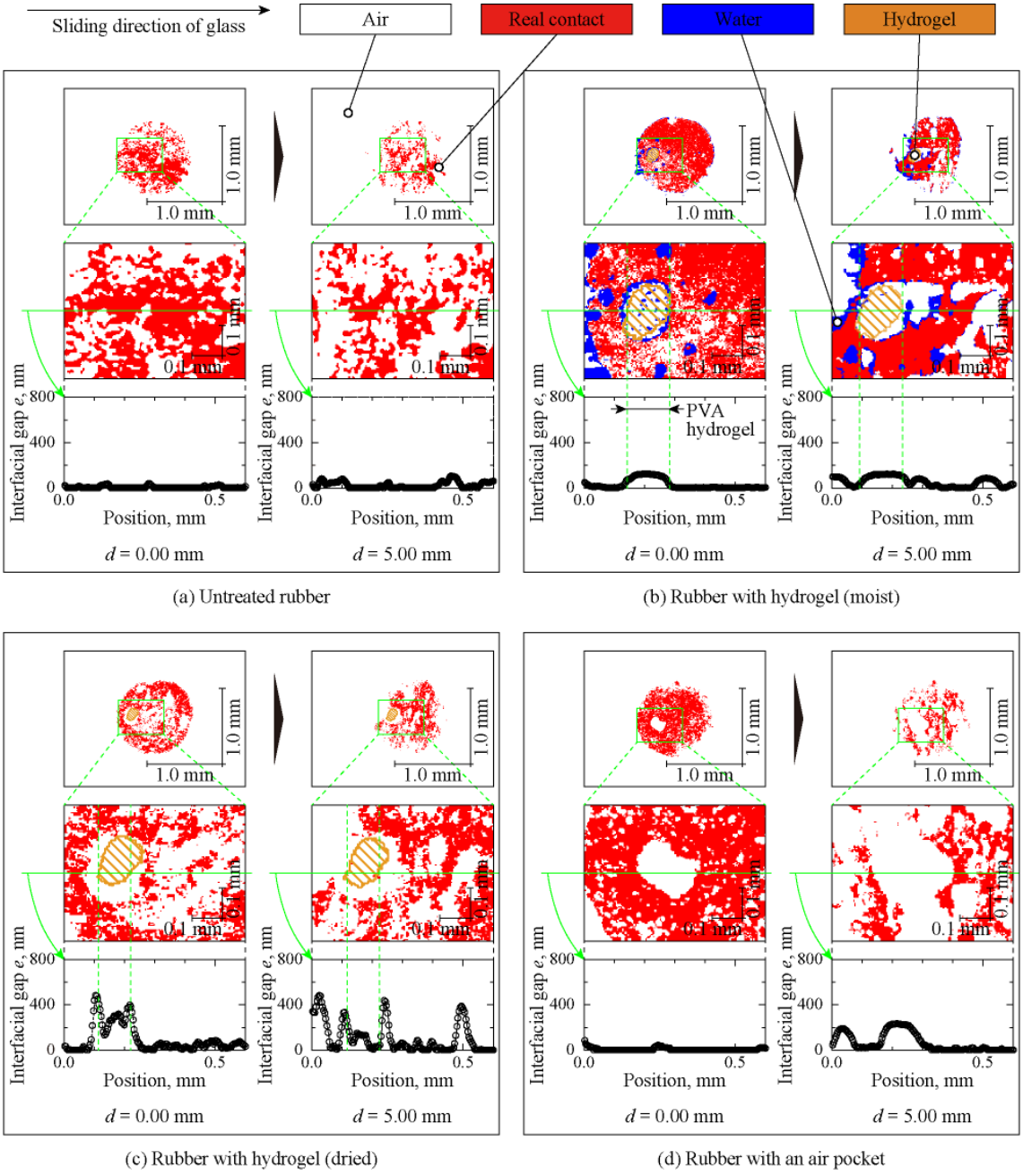

Fig. 6.4 Distributions of the real contact, air, and water between each rubber hemisphere and the glass plate at d = 0.00 and 5.00 mm and v = 1.00 mm/s in the unlubricated condition [30].

air pocket at v = 1.00 mm/s and d = 0.00 and 5.00 mm. The magnified view of the contact condition and the distribution of e on the equator line in the magnified view parallel to the sliding direction are shown for each case. Red, white, and blue regions indicate real contacts (rubber–glass or hydrogel–glass interface), the air–glass interface, and the water–glass interface, respectively. The shaded areas (orange) in Fig. 6.4(b) and (c) indicate the area of the hydrogel patch. For all specimens, many real contacts were formed because each specimen surface was not extremely smooth and that the apparent real contact region was elongated in the direction perpendicular to the sliding direction in the sliding process. A similar dependency has been reported in the literature [25,26]. For the rubber with (moist and dried) hydrogel hemispheres, especially for the rubber with a (dried) hydrogel hemisphere at d = 0.00 mm, the hydrogel region was present on the apparent real contact, and e on the hydrogel patch tended to be higher than that on the other region. Interestingly, Fig. 6.4(b) indicates that the real contact was surrounded by water droplets even in the unlubricated condition. In contrast, as shown in Fig. 6.4(c), no water droplets were observed for the rubber with a (dried) hydrogel hemisphere. These results suggest that a small amount of water was bled from the moist hydrogel. Fig. 6.4(d) shows that, for the rubber with an air pocket hemisphere, an air–glass interface with a size of about 100 μm was observed, and this region corresponded to the air pocket. The real contact distribution, excluding the air pocket region, was similar to the untreated rubber.

Fig. 6.5 shows the contact conditions in the water-lubricated condition. Regarding the rubber with a (moist) hydrogel hemisphere (Fig. 6.5(b)), while few real contacts on the hydrogel patch were formed, real contacts formed around the hydrogel patch. The hydrogel patch induces nonuniform wetting, which promotes real contact formation around the hydrogel patch, but the front edge of real contacts during sliding would be peeled due to water flow [17,27,28]. Fig. 6.5(c) shows the air–glass interface in the apparent contact area at d = 0.00 mm corresponding to the air pocket. In contrast, air bubbles observed in the apparent contact area at d = 5.00 mm indicate that the air trapped in the air pocket leaked out during sliding. Here, the real contacts were surrounded by water instead of air.

Interestingly, the real contacts were surrounded by a water meniscus for both the rubber with a (moist) hydrogel hemisphere in the unlubricated condition (Fig. 6.4(b)) and the rubber with an air pocket hemisphere in the water-lubricated condition (Fig. 6.5(c)).

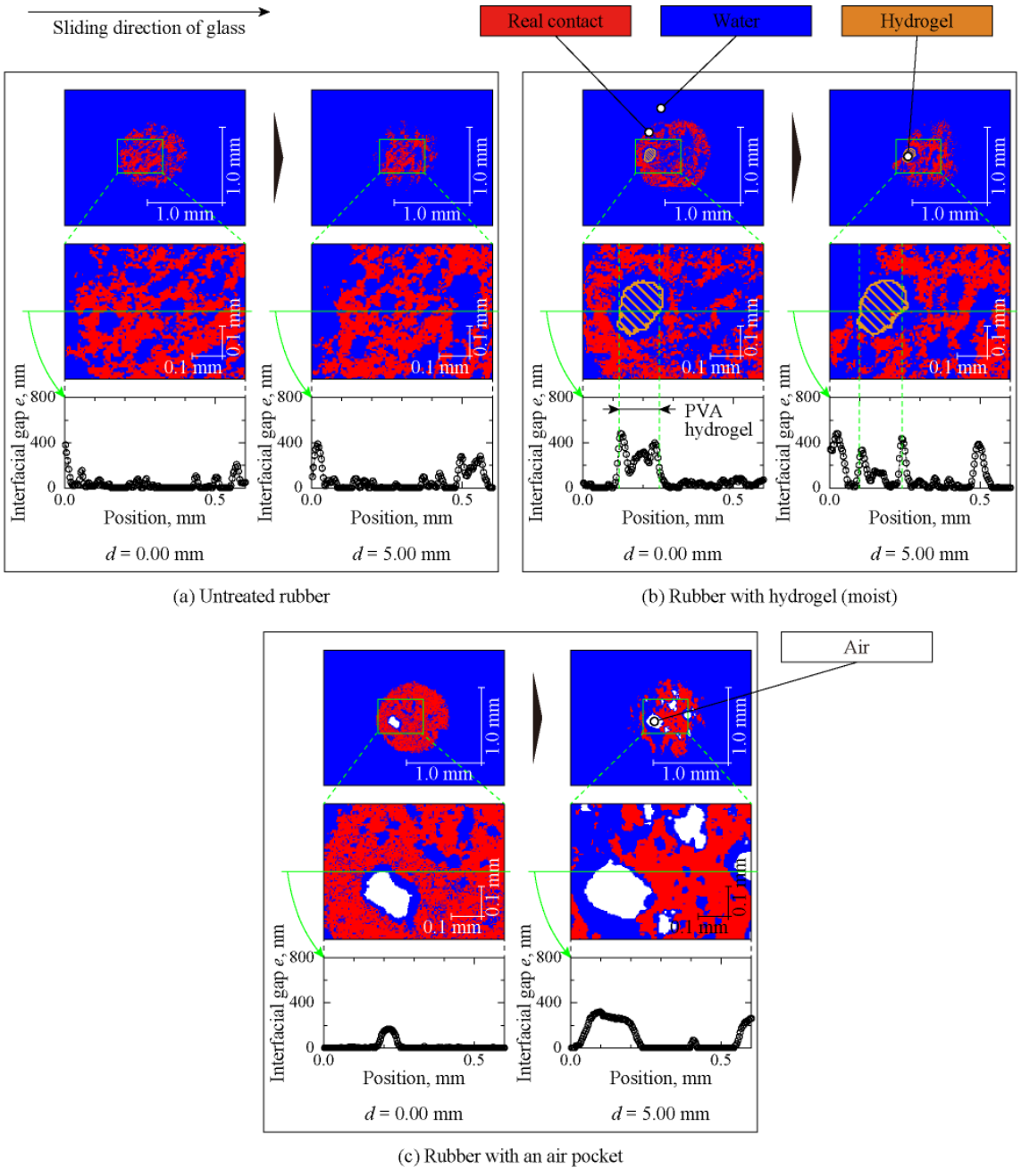

Fig. 6.5 Distributions of the real contact, air, and water between each rubber hemisphere and the glass plate at d = 0.00 and 5.00 mm and v = 1.00 mm/s in the water-lubricated condition [30].

6.3.2 Real contact formation and friction behavior

Fig. 6.6 shows A_r and μ plotted against d at v = 1.00 mm/s in unlubricated and water-lubricated conditions. In the unlubricated condition, A_r increased and decreased before sliding, and got saturated after a decrease at d < 3 mm. This dependency was similar to that reported by Sahli et al. [27,28]. μ was also un stable at d < 3 mm but became stable at d > 3 mm. Only the rubber with a (moist) hydrogel hemisphere under the unlubricated condition demonstrated the stick–slip behavior at d < 3 mm. Fig. 6.6(b) indicates that A_r and μ in the water-lubricated condition initially decreased and got saturated at d > 2 mm.

In Fig. 6.7, the mean and standard deviation of A_r and μ at d = 5.00 mm/s for all the rubbers are plotted against v. In the unlubricated condition, A_r and μ were constant against v, but in the

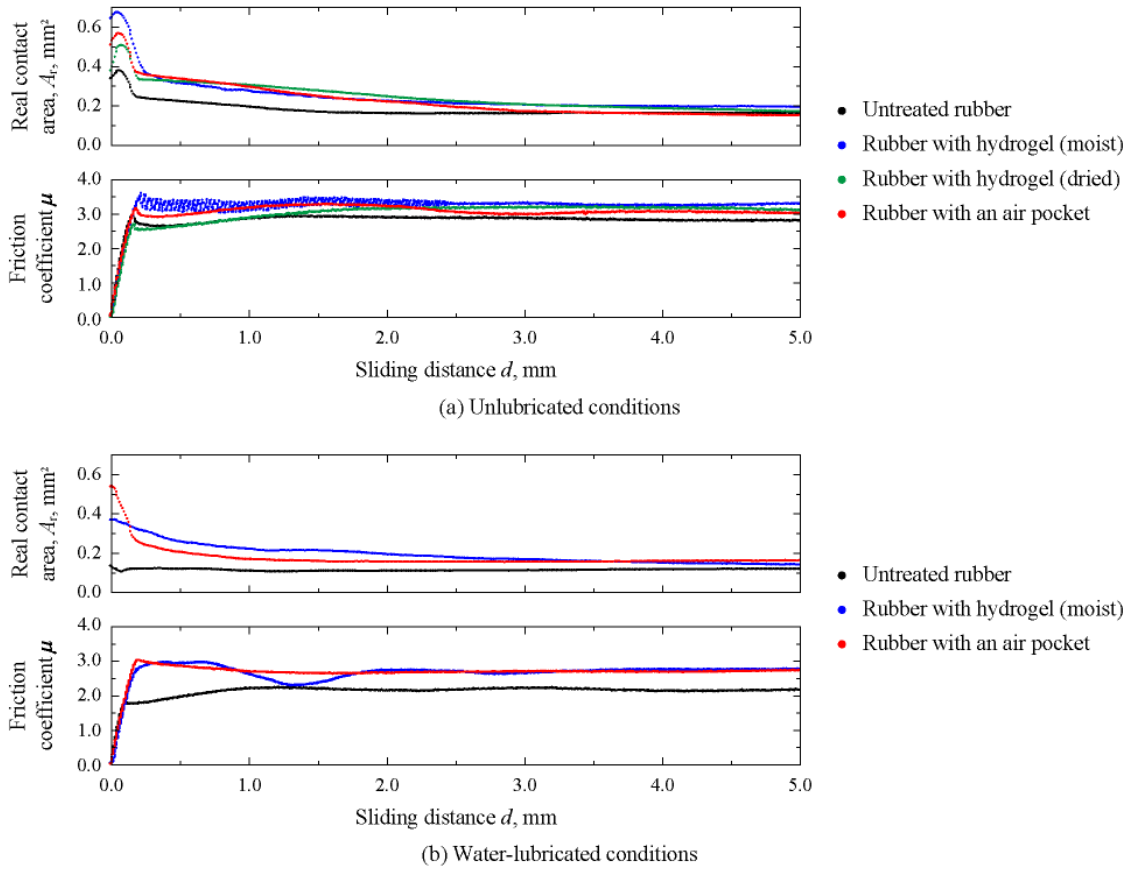

Fig. 6.6 Influence of the sliding distance (d) on the real contact area (A_r) and friction coefficient (μ) at sliding velocity v = 1.00 mm/s: (a) unlubricated condition and (b) water-lubricated condition [30].

water-lubricated condition, these parameters decreased with v. Fig. 6.8 shows μ plotted against A_r for all the conditions at d = 5.00 mm and indicates a proportional relation between them. This proportional relation indicates that the adhesion term was dominant [29]. Based on the differences among the rubber specimens in the unlubricated condition, A_r and μ increased in the order untreated

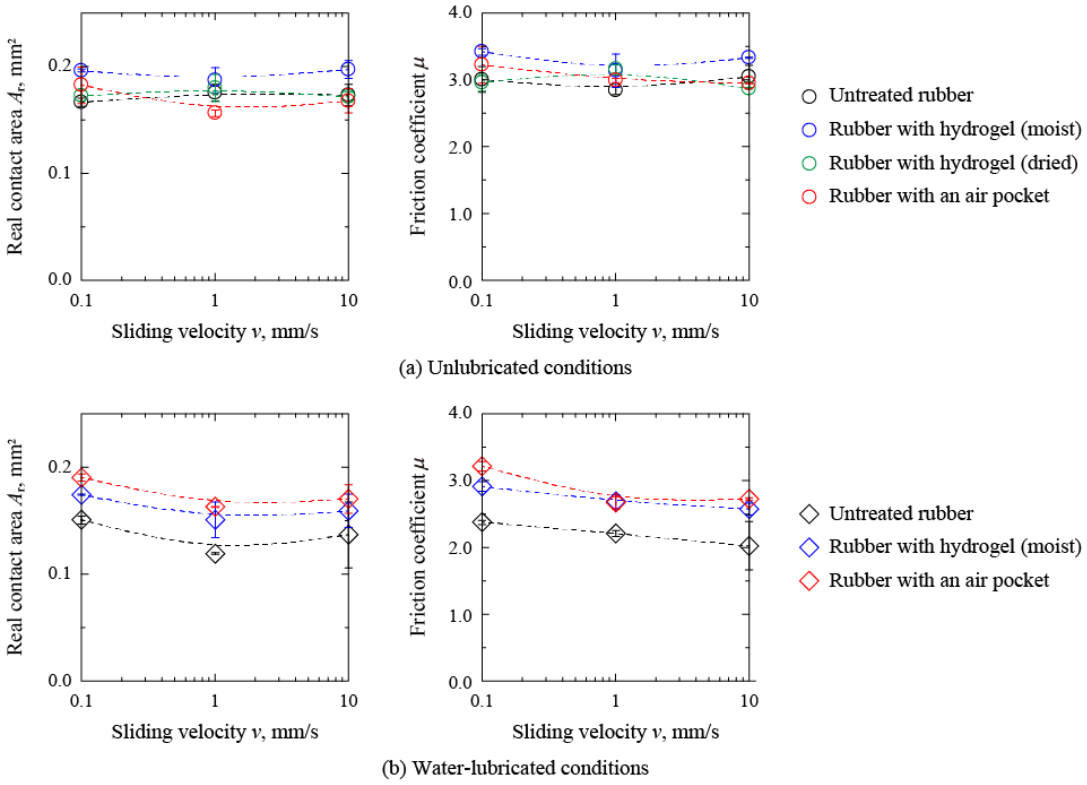

Fig. 6.7 Real contact area (A_r) and friction coefficient (μ) plotted against the sliding velocity (v) at d = 5.00 mm: (a) unlubricated condition and (b) water-lubricated condition [30].

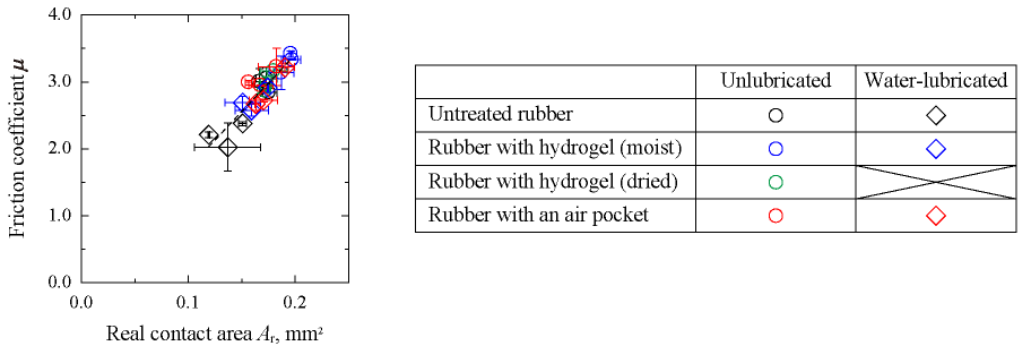

Fig. 6.8 Friction coefficient (μ) plotted against the real contact area (A_r) at d = 5.00 mm [30].

rubber ≈ rubber with a hydrogel (dried) ≈ rubber with an air pocket < rubber with a hydrogel (moist), regardless of v. In the water-lubricated condition, A_r and μ increased in the order untreated rubber << rubber with a hydrogel (moist) < rubber with an air pocket. These results suggest that real contact formation is promoted in a nonuniform wetting state, which induces high friction.

6.4 Discussion

6.4.1 Wettability evaluation

The work of adhesion (W) and spreading coefficient (S) correspond to the parameter to quantify wettability between the rubber and floor under unlubricated and lubricated conditions, respectively, and they are calculated from the following equations [2,3,18]:

$$W = (\gamma_R + \gamma_G) - \gamma_{RG} \tag{6.1}$$

$$S = \gamma_{RG} - (\gamma_{RW} + \gamma_{GW}) \tag{6.2}$$

where the subscripts R, G, and W correspond to rubber, glass, and water, respectively, γ_i is the surface free energy of material i, and γ_{ij} is the interfacial free energy between materials i and j. W between the solid material i (rubber or glass) and water can also be calculated from γ_W and the contact angle of water on the solid material i (θ_i) in the following Eq. [2]:

$$W_i = (\gamma_i + \gamma_W) - \gamma_{iW} = \gamma_W(1 + \cos\theta_i) \tag{6.3}$$

Kaelble and Uy theory explains that γ_i is the sum of the dispersion term, γ_i^d, and polar term, γ_i^p ($\gamma_i = \gamma_i^d + \gamma_i^p$), and that γ_{ij} is obtained by the following equation [3,30]:

$$\gamma_{ij} = \left(\sqrt{\gamma_i^d} - \sqrt{\gamma_j^d}\right)^2 + \left(\sqrt{\gamma_i^p} - \sqrt{\gamma_j^p}\right)^2 \tag{6.4}$$

Table 6.2 shows the measured parameters among the silicone rubber (containing 10 vol.% titanium oxide and 20 wt.% inorganic fluorescent powder), moist PVA hydrogel (containing 10 vol.%

titanium oxide), and BK7 glass: the elastic modulus (E), θ, and γ, and the calculated values of W and S in contact with the glass in air and water based on Eqs. (1)–(3). E was measured using a dynamic viscoelastic measurement device (Reogel E4000, UBM Co., Ltd., Kyoto, Japan), and θ with a 1.0-μL drop of ion-exchanged water and diiodomethane (Wako 1st grade, FUJIFILM Wako Pure Chemical Corporation, Osaka, Japan) was measured using a contact angle meter (DMs-401, Kyowa Interface Science Co., Ltd., Saitama, Japan).

Table 6.2 Elastic moduli and wettability parameters of the silicone rubber, PVA hydrogel, and glass

Material		Silicone rubber	Moist PVA hydrogel	Glass
Elastic modulus E, MPa		2.04	0.0333	-
Contact angle θ, deg.	Water	108.6	18.7	50.3
	Diiodomethane	90.7	45.0	44.3
Surface free energy γ, mJ/m^2	Dispersion	11.0	22.5	26.8
	Polar	1.7	46.6	24.7
	Total	12.7	69.1	51.5
Work of adhesion W contacting with the glass plate in air, mJ/m^2		47.3	117.0	-
Spreading coefficient S contacting with the glass plate in water, mJ/m^2		−24.0	−1.4	-

6.4.2 Theoretical modeling of dewetting

When a real contact exists between the rubber and floor (glass) and S has a negative value, as shown in Fig. 6.9, the real contact can be expanded by the dewetting effect [7,8]. The dewetting effect is explained based on the free energy of the system (G), which a is a convex quadratic function of the real contact size R in the following equation [7,8]:

$$G \sim -|S|R^2 + Ee^2R \tag{6.5}$$

Here, G corresponds to the sum of the changes in the surface free energy and strain energy during dewetting. Considering the real contact formation, Eq. (6.5) explains that an activation energy (= $G(Ee^2/2|S|) = G(R_c/2)$) is required to form a real contact with $R \geq R_c = Ee^2/|S|$ and that the real contact

with $R \geq R_c$ can thermodynamically expand because the value of G and the increasing rate of G are negative at $R > R_c$ [7,8].

The theory of dewetting for uniform wetting has been developed to apply the dewetting effect for nonuniform wetting [17]. The friction behavior of rubber hemispheres with a PVA hydrogel patch was investigated on a glass plate under the water-lubricated condition, and the dewetting effect was promoted by adding a hydrogel patch because $G = 0$ at $R \leq R_c$; however, the hydrogel patch size that could achieve high friction was limited [17]. To clarify the theory of dewetting for nonuniform wetting, the real contact surrounded by a water meniscus (Fig. 6.9) has been studied. Because the water around real contacts was in a narrow gap, the pressure in this water was negative (Laplace pressure) [2]. In the theory of dewetting for uniform wetting, only the strain energy in rubber was considered, but, during real contact expansion in nonuniform wetting (where real contacts were surrounded by a water meniscus), as shown in Fig. 6.9, the negative pressure would lead negative work on the side face of the rubber around the real contact and the bottom face of the rubber. As shown in Fig. 6.9, assuming that a real contact was a square with a size of R, the side face of the rubber around the real contact moves in

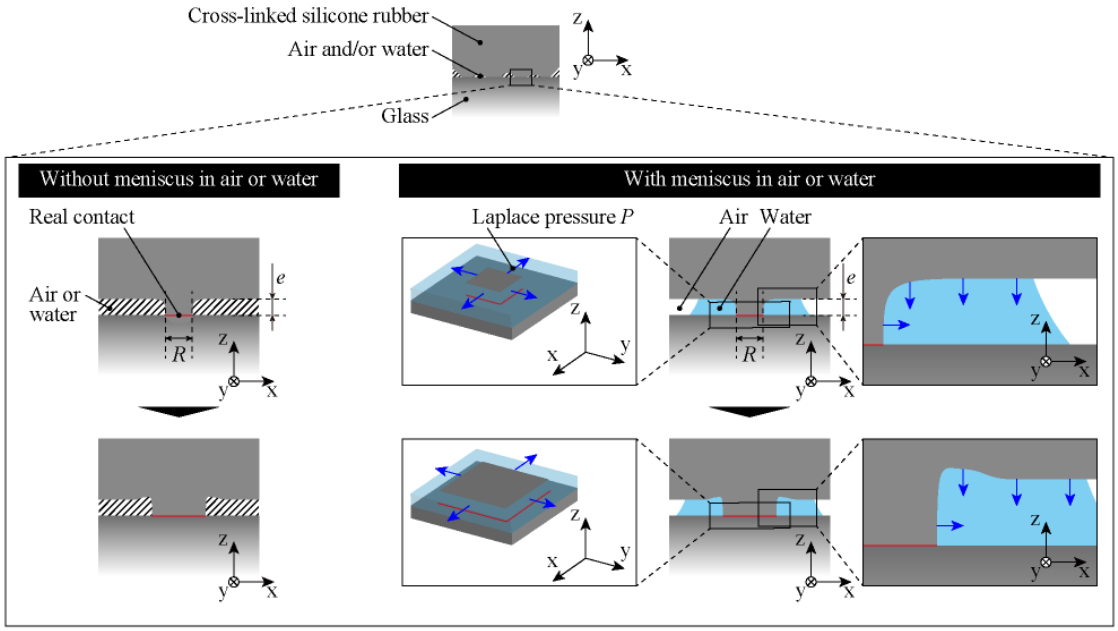

Fig. 6.9 Schematic of real contact formation caused by the dewetting effect of a real contact without/with a meniscus [30].

the positive and negative directions in the *x* and *y* axes, and the bottom face of the rubber moves in the negative direction in the *z* axis in real contact formation. Thus, *G* for real contact surrounded by a water meniscus is obtained in the following equation:

$$G \sim -|S|R^2 + Ee^2R + \left(\int_0^{\frac{R}{2}} 2exP\,dx \times 2 + \int_0^{\frac{R}{2}} 2eyP\,dy \times 2 + \int_0^{e} R^2P\,dz \right)$$

$$= (-|S| + 2eP)R^2 + Ee^2R \tag{6.6}$$

where *P* is the pressure in the meniscus and can be calculated from γ_W and the curvature radius of the meniscus *r* [2]:

$$P = -\gamma_W \frac{1}{r} \tag{6.7}$$

As shown in Fig. 6.10, *r* was geometrically calculated from *e* and the water contact angles on rubber (θ_R) and glass (θ_G). In detail, comparing the triangles OAD and OBC, OA = $r\sin(\theta_R - 90°)$ and OB = $r\sin(90° - \theta_G)$. Considering OA + AB = OB and AB = *e*,

$$r\sin(\theta_R - 90°) + e = r\sin(90° - \theta_G) \tag{6.8}$$

Hence,

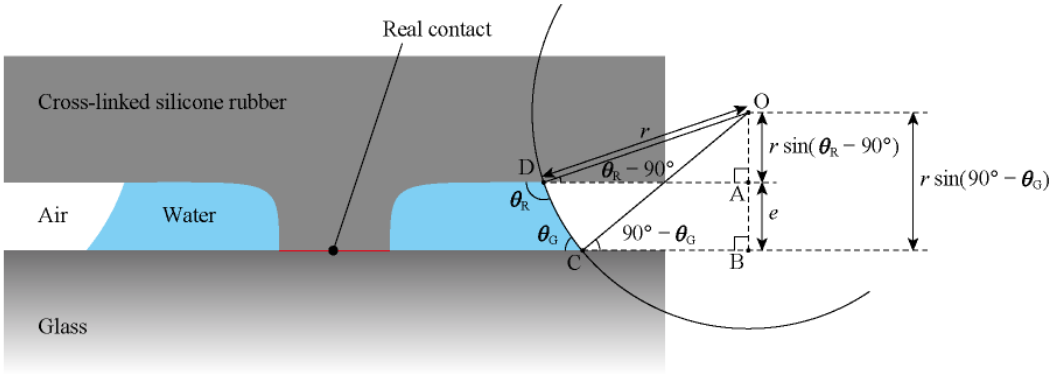

Fig. 6.10 Schematic of the cross section of a real contact surrounded by a meniscus [30].

$$r = \frac{e}{\cos\theta_R + \cos\theta_G} \tag{6.9}$$

Substituting Eq. (9) into Eq. (7),

$$P = -\frac{\gamma_W(\cos\theta_R + \cos\theta_G)}{e} \tag{6.10}$$

Therefore,

$$G \sim -\left(|S| + 2\gamma_W(\cos\theta_R + \cos\theta_G)\right)R^2 + Ee^2R \tag{6.11}$$

Considering Eqs. (6.2) and (6.3),

$$\begin{aligned} & |S| + 2\gamma_W(\cos\theta_R + \cos\theta_G) \\ =& -\left(\gamma_{RG} - (\gamma_{RW} + \gamma_{GW})\right) + 2\gamma_W\left(\frac{(\gamma_R + \gamma_W) - \gamma_{RW}}{\gamma_W} - 1 + \frac{(\gamma_G + \gamma_W) - \gamma_{GW}}{\gamma_W} - 1\right) \\ =& \ 2\left((\gamma_R + \gamma_G) - \gamma_{RG}\right) + \left(\gamma_{RG} - (\gamma_{RW} + \gamma_{GW})\right) \\ =& \ 2W + S \end{aligned} \tag{6.12}$$

Substituting Eq. (6.12) into Eq. (6.11),

$$G \sim -(2W + S)R^2 + Ee^2R \tag{6.13}$$

According to Eq. (6.13), R_c for a real contact surrounded by a meniscus is obtained by the following equation:

$$R_c = \frac{Ee^2}{2W + S} \tag{6.14}$$

Interestingly, not only S but also W determines the value of R_c. Additionally, Eq. 6.14 shows that R_c can be decreased by adding a water meniscus around real contacts, considering $R_c = Ee^2/|S|$ for uniform wetting.

6.4.3 Estimation of the free energy of the system

Eqs. (6.5) and (6.13) show that e also determines the value of G in addition to W and S. According to the previous studies, e on the apparent contact is almost constant in dewetting [8,12], leading to a peak corresponding to the mean interfacial gap on the apparent contact in the histogram of

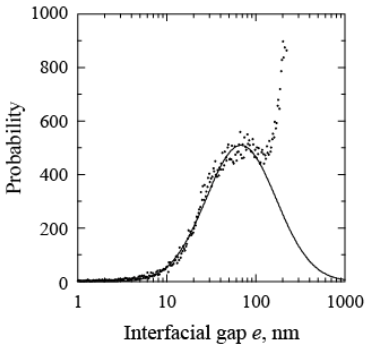

Fig. 6.11 Histogram of the interfacial gap (e) between the untreated rubber hemisphere and glass in the unlubricated condition at v = 1.00 mm/s and d = 5.00 mm [30].

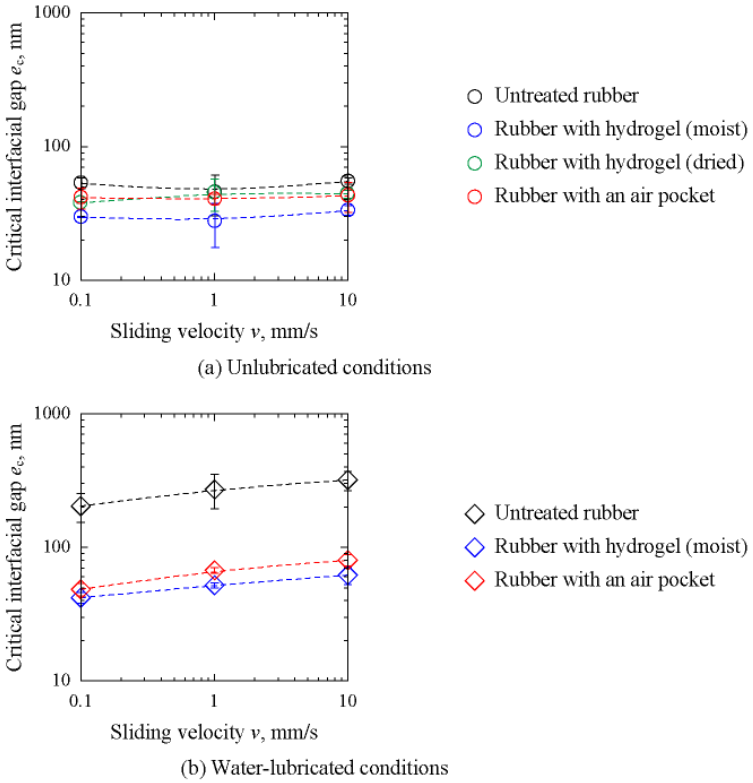

Fig. 6.12 Influence of the sliding velocity (v) on the critical interfacial gap (e_c): (a) unlubricated condition and (b) water-lubricated condition [30].

e [17]. Fig. 6.11 shows the bimodal histogram of e for the untreated rubber under the unlubricated condition at v = 1.00 mm/s and d = 5.00 mm. Because Nishi et al. reported that the most frequent value of e at the peak with lower probability corresponds to the mean value of e within the apparent contact area [17], its value in the histogram for each condition was defined as the critical interfacial, e_c. Fig. 6.12 shows the influence of v on e_c for all the rubbers in unlubricated and water-lubricated conditions. While e_c had almost constant values in the unlubricated condition, e_c increased with v in the water-lubricated condition. Here, the increase in e_c with v was induced by water inflow to the interface. In unlubricated and water-lubricated conditions, e_c increased in the order rubber with a hydrogel (moist) < untreated rubber ≈ rubber with a hydrogel (dried) ≈ rubber with an air pocket, and rubber with a hydrogel (moist) ≈ rubber with an air pocket < untreated rubber, respectively. Regarding the influence of the lubricant (water), adding the lubricant led to high e_c for all conditions, but the amount of increase in e_c for the rubber with a hydrogel (moist) and the rubber with an air pocket was smaller than that for the untreated rubber. These results indicate that nonuniform wetting leads to low e_c.

Fig. 6.13 shows the calculated G–R curves at d = 5.00 mm for all conditions, except for the rubber with a hydrogel (moist) under the water-lubricated condition. The G–R curve for the rubber with a hydrogel (moist) under the water-lubricated condition is not plotted in Fig. 6.13 because the G–R curve in this situation is calculated based on a different definition as explained in Chapter 5 [17].

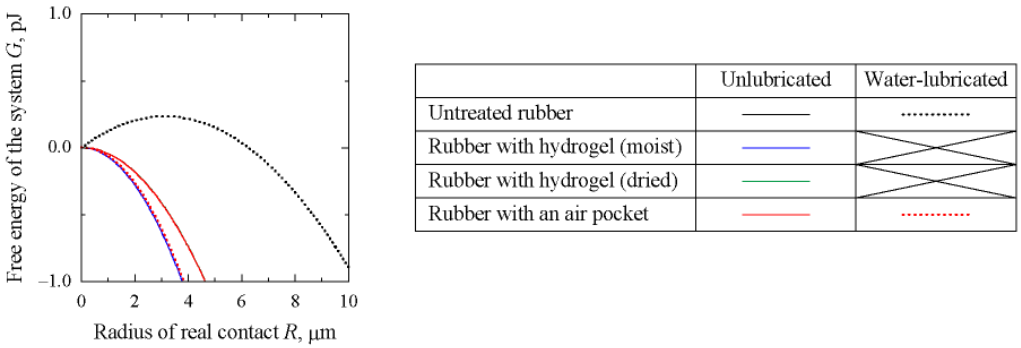

Fig. 6.13 Free energy of the system G as a function of the size of real contact R [30].

In the calculation of *G*–*R* curves in Fig. 6.13, $e = e_c$ was substituted into Eq. (6.13). A previous study

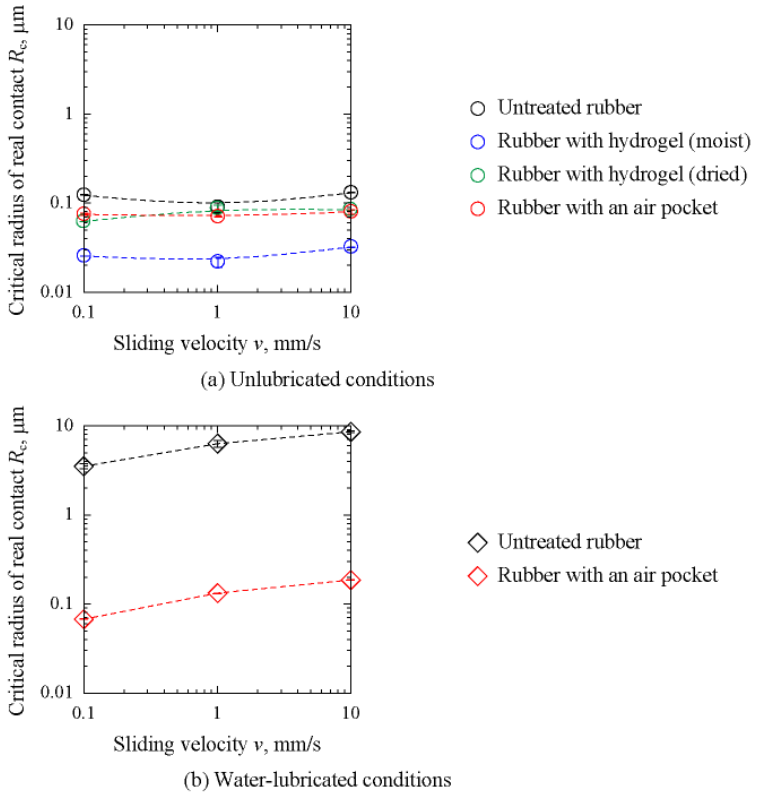

Fig. 6.14 Critical size of the real contact (R_c) plotted against the sliding velocity (v): (a) unlubricated condition and (b) water-lubricated condition [30].

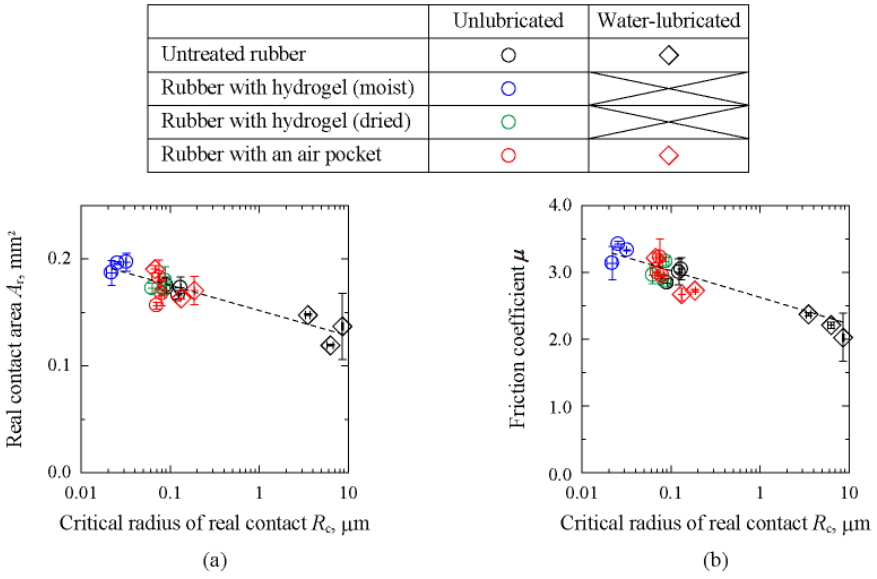

Fig. 6.15 Influence of the critical size of the real contact (R_c) on the real contact area (A_r) and friction coefficient (μ) [30].

showed that the dewetting effect can be correlated with the value R_c [17]. R_c was calculated from Eq. (6.14), and the results were plotted against v for each lubrication condition (Fig. 6.14). R_c was constant in the unlubricated condition but positively correlated with v in the water-lubricated condition. R_c in unlubricated and water-lubricated conditions increased in the order rubber with a hydrogel (moist) < untreated rubber ≈ rubber with a hydrogel (dried) ≈ rubber with an air pocket, and rubber with an air pocket < untreated rubber, respectively.

Fig. 6.15 shows the influence of R_c on A_r and μ and indicates that A_r and μ decreased with R_c, regardless of the wetting uniformity, v, and lubricant conditions. These negative correlations suggest that a decrease in R_c would promote real contact formation. Therefore, controlling R_c with E, e, W, S, and wetting uniformity is reasonable to achieve rubber with high friction.

6.5 Conclusions

By conducting friction tests using silicone rubber hemispheres with a PVA hydrogel patch or a cavity, the influence of wetting uniformity on the contact condition and friction behavior of rubber in unlubricated and water-lubricated conditions was investigated, and the following conclusions were obtained:

The observation of contact conditions indicated that real contacts were surrounded by water droplets during the friction test for the rubber with a moist hydrogel patch in the unlubricated condition and the rubber with an air pocket hemisphere in the water-lubricated condition. While A_r and μ in the unlubricated condition remained unchanged with an increase in v, they decreased with v in the water-lubricated condition. Nonuniform wetting (coexistence of air and water) induced high A_r and μ. Because the adhesion term was dominant due to the proportional relationship between μ and A_r, we focused on real contact formation and developed a dewetting theory for nonuniform wetting. Our theory explains that nonuniform wetting (real contact surrounded by a water meniscus) can promote real contact formation and increase μ. Therefore, forming water menisci around real contacts to add nonuniform wetting can achieve high slip resistance in soft materials, such as rubber.

References

[1] Lengiewicz J., de Souza M., Lahmar M.A., Courbon C., Dalmas D., Stupkiewicz S., et al., "Finite Deformations Govern the Anisotropic Shear-Induced Area Reduction of Soft Elastic Contacts," Journal of the Mechanics and Physics of Solids, 143, 2020, 104056.

[2] de Gennes P.-G., Brochard-Wyart F., and Quéré D., Special Interfaces. Capillarity Wetting Phenom. Drops, Bubbles, Pearls, Waves, New York, NY, Springer New York, 2004, p. 215–59.

[3] Nishi T., "Effects of Wettability on Tribology of Soft Matter," Toraibarojisuto/Journal of Japanese Society of Tribologists, 64, 10, 2019, 588–93.

[4] Roberts A.D., "Squeeze Films between Rubber and Glass," Journal of Physics D: Applied Physics, 4, 3, 1971, 423–32.

[5] Roberts A.D., and Tabor D., "The Extrusion of Liquids between Highly Elastic Solids," Proceedings of the Royal Society of London Series A, Mathematical and Physical Sciences, 325, 1562, 1971, 323–45.

[6] Brochard-Wyart F., and De Gennes P.G., "Dewetting of a Water Film between a Solid and a Rubber," Journal of Physics Condensed Matter, 4, 10, 1994, 1727–35.

[7] Martin P., Silberzan P., and Brochard-Wyart F., "Sessile Droplets at a Solid/Elastomer Interface," Langmuir, 13, 18, 1997, 4910–4.

[8] Martin P., and Brochard-Wyart F., "Dewetting at Soft Interfaces," Physical Review Letters, 80, 15, 1998, 3296–9.

[9] Martin A., Buguin A., and Brochard-Wyart F., "Dewetting Nucleation Centers at Soft Interfaces," Langmuir, 17, 21, 2001, 6553–9.

[10] Nishi T., "Influence of Lubricant Properties and Contacting Velocity on Real Contact Formation between Rubber and Glass in a Contact Process," Tribology International,

127, 2018, 240–4.

[11] Nishi T., “Influence of Curvature Radius, Elastic Modulus, and Contact Velocity on Real Contact Formation between Rubber Hemisphere and Glass Plate during Contact Process under a Water-Lubricated Condition,” Tribology International, 130, 2019, 284–8.

[12] Chudak M., Kwaks J.S., Snoeijer J.H., and Darhuber A.A., “Non-Axisymmetric Elastohydrodynamic Solid-Liquid-Solid Dewetting: Experiments and Numerical Modelling,” European Physical Journal E, 43, 1, 2020, 1–11.

[13] Martin A., Clain J., Buguin A., and Brochard-Wyart F., “Wetting Transitions at Soft, Sliding Interfaces,” Physical Review E - Statistical, Nonlinear, and Soft Matter Physics, 65, 3, 2002, 031605/1-031605/4.

[14] Martin A., Buguin A., and Brochard-Wyart F., “‘Čerenkov’ Dewetting at Soft Interfaces,” Europhysics Letters, 57, 4, 2002, 604–10.

[15] Momozono S., Iguchi Y., Oshikiri K., Nakamura K., and Kyogoku K., Effects of interfacial free energy on adhesive friction behavior of elastomer surfaces under wet conditions. 5th World Tribol. Congr., vol. 4, 2013, p. 3208–11.

[16] Nishi T., Yamaguchi T., Shibata K., and Hokkirigawa K., “Influence of Unforced Dewetting and Enforced Wetting on Real Contact Formation and Friction Behavior between Rubber Hemisphere and Glass Plate during Contacting and Sliding Processes,” Tribology International, 141, 2020, 105921.

[17] Nishi T., Yamaguchi T., Shibata K., and Hokkirigawa K., “Optimizing the Frictional Behavior of Partially Wetting Soft Contacts as Measured with Hydrogel Covered Silicones,” Tribology International, 153, 2021, 106586.

[18] Nishi T., Moriyasu K., Harano K., and Nishiwaki T., “Influence of Surface Free Energy on Rubber Friction Properties under Water/Ethanol Lubrilated Conditions,”

Toraibarojisuto/Journal of Japanese Society of Tribologists, 59, 11, 2014, 717–23.

[19] Nishi T., Moriyasu K., Harano K., and Nishiwaki T., Influence of dewettability on rubber friction properties with different surface roughness under water/ethanol/glycerol lubricated conditions. Tribol. Online, vol. 11, Japanese Society of Tribologists, 2016, p. 601–7.

[20] Kawasaki S., Tada T., and Persson B.N.J., "Adhesion and Friction between Glass and Rubber in the Dry State and in Water : Role of Contact Hydrophobicity," Soft Matter, 2018, 5428–41.

[21] Defante A.P., Nyarko A., Kaur S., Burai T.N., and Dhinojwala A., "Interstitial Water Enhances Sliding Friction," Langmuir, 34, 13, 2018, 4084–94.

[22] Nishi T., Moriyasu K., and Nishiwaki T., "Precise Measurement of Clearance between Two Substrates Using Evanescent Waves," Tribology Online, 12, 5, 2017, 251–6.

[23] Axelrod D., Burghardt T.P., and Thompson N.L., "Total Internal Reflection Fluorescence," Annual Review of Biophysics and Bioengineering, 13, 1, 1984, 247–68.

[24] Eguchi M., Shibamiya T., and Yamamoto T., "Measurement of Real Contact Area and Analysis of Stick/Slip Region," Tribology International, 42, 11–12, 2009, 1781–91.

[25] Eguchi M., "Statistical Measurement of Real Contact Area on the Basis of Image Intensity Histograms (Part 1) -Using Gaussian Distribution of Light Interference Image-," Toraibarojisuto/Journal of Japanese Society of Tribologists, 57, 5, 2012, 345–52.

[26] Eguchi M., Hirayanagi T., and Miyoshi T., "Statistical Measurement of Real Contact Area on the Basis of Image Intensity Histograms (Part 2) -Application to Paper-Based Wet Friction Materials-," Toraibarojisuto/Journal of Japanese Society of Tribologists, 57, 5, 2012, 353–60.

[27] Sahli R., Pallares G., Ducottet C., Ben Ali I.E., Al Akhrass S., Guibert M., et al.,

"Evolution of Real Contact Area under Shear and the Value of Static Friction of Soft Materials," Proceedings of the National Academy of Sciences of the United States of America, 115, 3, 2018, 471–6.

[28] Sahli R., Pallares G., Papangelo A., Ciavarella M., Ducottet C., Ponthus N., et al., "Shear-Induced Anisotropy in Rough Elastomer Contact," Physical Review Letters, 122, 21, 2019, 214301.

[29] Bowden F.P., and Tabor D., "The Friction and Lubrication of Solids Part II," Physics Today, 17, 6, 1964, 72.

[30] Nishi T., Yamaguchi T., Shibata K., and Hokkirigawa K., "Friction Behavior of Silicone Rubber Hemisphere under Non-Uniform Wetting States: With Water Droplets in Air or Air Bubbles in Water," Tribology International, 155, 2021, 106769.

Chapter 7

Development of slip-resistant shoe outer soles using rubbers without/with activated carbon or sodium chloride

7.1 Introduction

As mentioned in Chapters 5 and 6, to increase friction of rubber on wet and smooth floor, it would be important to make a wetting state between two surfaces nonuniform because nonuniform wetting promotes real contact formation, which enlarges the friction coefficient μ [1,2]. Here, nonuniform wetting is formed by a heterogeneous interface such as between the rubber (hydrophobic) with a hydrogel patch (hydrophilic) and the floor [1] and the rubber and the floor with air bubbles (hydrophobic) in water (hydrophilic) [2].

To apply rubbers with nonuniform wetting characteristics to shoe outer soles, durability (tensile strength, tear strength, wear resistance, weather resistance, and so on) in a practical use must be considered. Diene rubbers such as natural rubber (NR), isoprene rubber (IR), butadiene rubber (BR), and styrene-butadiene rubber (SBR) are generally used for shoe outer soles owing to their high durability in a practical use. However, it is technologically challenging to ensure enough durability for diene rubbers with hydrogel such as polyvinyl alcohol (PVA) hydrogel particles because diene rubbers (hydrophobic) and hydrogels (hydrophilic) have extremely different wetting properties and their adhesion to each other is very poor. In general, when the diameter of pores on the hydrophobic material is <10–100 μm, water cannot penetrate the pores [3]. Thus, nonuniform wetting can be realistically achieved by adding air pockets (small pores) to the diene rubber surface. Considering the wear of the rubber surface, including the air pockets in practical use, adding small cavities, or something that would convert into air pockets via exposure to the atmosphere would be more appropriate. Herein we used activated carbon (AC) and sodium chloride (SC) particles as additives to

obtain diene rubbers with air pockets. AC is a carbon-based porous material, and it is expected that the surface of diene rubbers with AC can form pores. By contrast, because water-soluble SC on the diene rubber surface can be removed upon water exposure, air pockets can be formed on the diene rubber surface, although the surface is worn out. Additionally, it is assumed that both AC and SC are chemically and thermally stable and do not affect the vulcanization process. Therefore, diene rubbers with AC or SC can be useful as shoe outer-sole materials.

So far, the friction behavior of rubbers with AC or SC has not been reported. Thus, the aim of this Chapter is to develop the rubbers with AC or SC and clarify their real contact formation and friction behavior between these rubbers and floor and their slip resistance. Rubber hemispheres and outer soles of vulcanized IR without/with AC or SC were prepared, and by controlling the elastic modulus E and additive content, friction tests using rubber hemispheres and outer soles and slip resistance test using outer soles in stepping motion were conducted.

7.2 Experimental methods

7.2.1 Material preparation

Considering practical applications of shoe outer soles, diene rubber was prepared in this Chapter, instead of silicone rubber used in Chapters 3–6. Diene rubbers were prepared in three steps, i.e., mixing at 100 °C–130 °C for 5.5 min (first mixing process) using a kneader (DS3–10MWB, Nihon Spindle Manufacturing Co., Ltd., Amagasaki, Japan), mixing at 30 °C–50 °C (second mixing process) using open roll (KD-M2-8, Kneader Machinery Co., Ltd., Taiwan, China), and pressing at 160 °C for 10 min (molding process) using three types of molds: sheet (215 mm × 130 mm × 2.0 mm), hemisphere (radius of curvature: 5.0 mm), and outer-sole molds. As shown in Table 7.1, five rubber compositions were prepared in the first mixing process using IR (Nipol IR2200, Zeon Corporation, Tokyo, Japan), silica (Nipsil VN3, Tosoh Silica Corporation, Tokyo, Japan), oil (P200, Sineikako Co., Ltd., Kobe, Japan), bis(triethoxysilylpropyl)tetrasulfide (Si69, Evonik Industries Japan, Osaka, Japan), stearic acid (50S, New Japan Chemical Co., Ltd., Osaka, Japan), and zinc oxide (activated zinc oxide

No.2, Honjo Chemical Corporation, Osaka, Japan). The content of silica was varied to change elastic modulus (*E*). Tables 7.2–7.4 show the rubber compositions in the second mixing process for rubbers without AC or SC (R1–5), rubbers with AC (AC1–8), and rubbers with SC (SC1–9), respectively. In the second process, surfer (#200, Hosoi Chemical Co., Ltd., Oita, Japan), benzothiazolyl disulfide (Nocceler DM, Ouchi Shinko Chemical Industrial Co., Ltd., Tokyo, Japan), tetramethylthiuram monosulfide (Nocceler TS, Ouchi Shinko Chemical Industrial Co., Ltd., Tokyo, Japan), titanium oxide (A150, Sakai Chemical Industry Co., Ltd., Osaka, Japan), AC (Shirosagi C SS, Osaka Gas Chemicals Co., Ltd., Osaka, Japan), and SC (Nakuru UM-10, Naikai Salt Industries Co., Ltd., Okayama, Japan) were added to the composites (masterbatches) obtained in the first mixing process. While titanium oxide was added to each rubber to ensure the high intensity of reflected light in friction tests using hemisphere specimens, titanium oxide was not added for outer-sole preparation. To control the pore size, we used SC grade with a size of ~10 μm. Tables 7.2–7.4 show the physical and geometric properties of each rubber. The specific gravity was measured using a liquid weighing method (JIS K 6268:1998) using a hydrometer (MD300S, Alfa Mirage Co., Ltd., Osaka, Japan). The tensile strength, breaking elongation, and tear strength were measured based on JIS K7311. The elastic modulus (*E*) was defined as the average elastic modulus when the strain was less than 5.0% in tensile strength measurements. For hemisphere specimens, the radius of curvature and arithmetical mean height (S_a) were measured using a one-shot 3D measuring macroscope (VR3000, Keyence Corporation, Osaka, Japan). S_a was quantified based on the 1.000-μm^2 area within the bottom top of hemisphere specimens, where plane correction was applied in the accompanying software (VR-H1A, Keyence Corporation, Japan). The surface free energy of each rubber was quantified by contact angle measurements with 1.0-μL ion-exchanged water and diiodomethane (Wako 1st grade, FUJIFILM Wako Pure Chemical Corporation, Osaka, Japan) using a contact angle meter (DMs-401, Kyowa Interface Science Co., Ltd., Saitama, Japan) [4]. According to the geometrical properties and surface free energies listed in Table 7.1, the differences in these parameters were so small that their effects on the real contact formation

and friction behavior were negligible. Fig. 7.1(a) indicates the overall images of hemisphere specimens (R3, AC5, and SC5) and their images obtained by scanning electron microscopy (SEM; JSM-6390A, JEOL Ltd., Tokyo, Japan). Here, for hemisphere specimens and outer soles with SC, the SC particles on the rubber surface were removed by washing in water and drying at room temperature before surface observation and friction tests. SEM images in Fig. 7.1(a) explain that air pockets were formed by adding AC and SC and that the air pocket size was about 0.1 μm and 5 μm, respectively. Using outer soles of all rubbers, shoes (TMM800, size: 27.0 cm, ASICS Corporation, Kobe, Japan) were prepared in a shoemaker (Sanin ASICS Industry Corporation, Sakaiminato, Japan). Fig. 7.1(b) shows a shoe with an outer sole of R3.

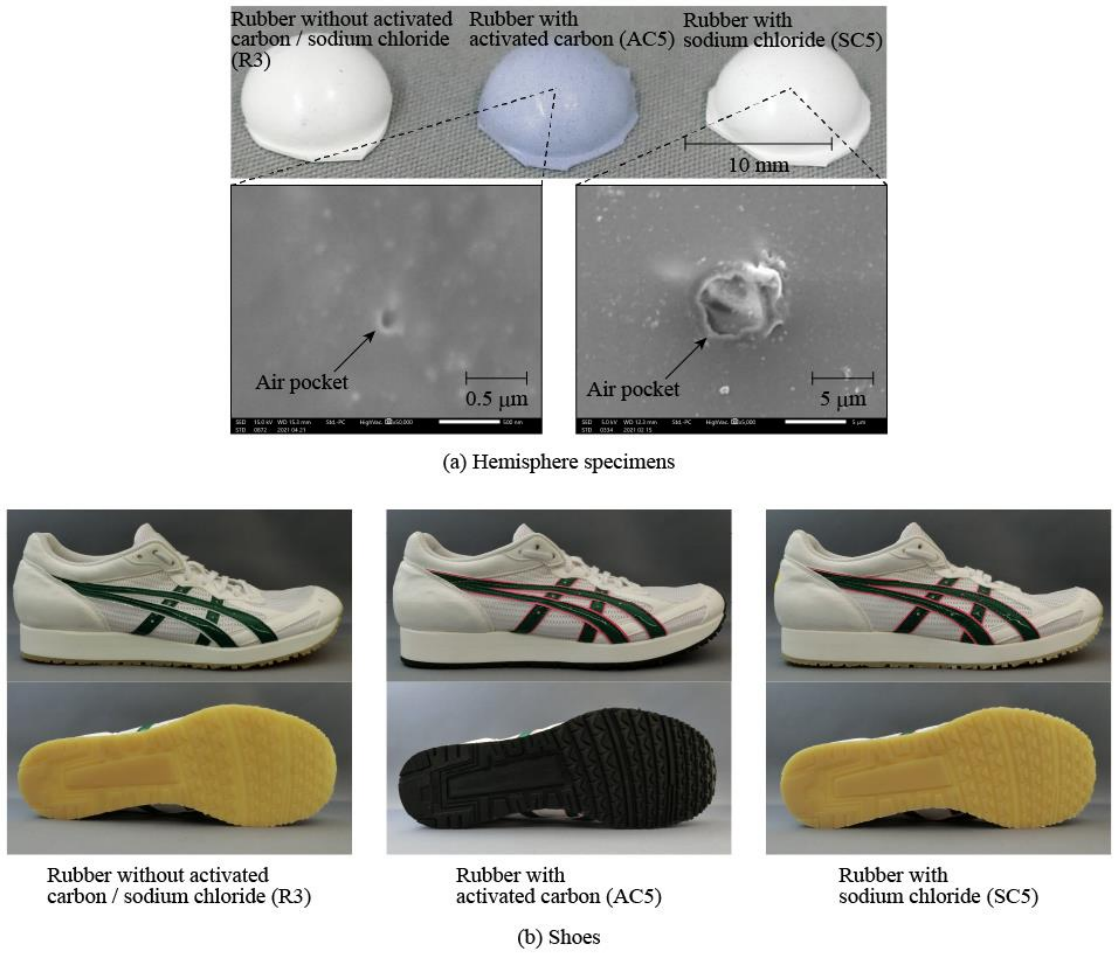

Fig. 7.1 Images of hemisphere specimens and shoes (R3, AC5, and SC5).

Table 7.1 Rubber compositions in the first mixing process. (unit: phr).

		MB1	MB2	MB3	MB4	MB5
Polymer	Isoprene rubber	100	100	100	100	100
Reinforcing filler	Silica	44	51	60	69	80
Plasticizing agent	Oil	20	20	20	20	20
Silane coupling agent	Bis(triethoxysilylpropyl) tetrasulfide	4.4	5.1	6.0	6.9	8.0
Processing aid	Stearic acid	2.0	2.0	2.0	2.0	2.0
	zinc oxide	5.0	5.0	5.0	5.0	5.0
Others (antioxidant and vulcanization accelerator)		3.5	3.5	3.5	3.5	3.5
Total		178.9	186.6	196.5	206.4	218.5

Table 7.2 Rubber composition in the second mixing process (unit: phr) and physical properties of rubbers without AC or SC

		R1	R2	R3	R4	R5
Masterbatch	MB1	178.9				
	MB2		186.6			
	MB3			196.5		
	MB4				206.4	
	MB5					218.5
Vulcanizing agent	Surfer	2.0	2.0	2.0	2.0	2.0
Vulcanization accelerator	Benzothiazolyl disulfide	1.0	1.0	1.0	1.0	1.0
	Tetramethylthiuram monosulfide	0.1	0.1	0.1	0.1	0.1
Pigment	Titanium oxide	35.0	36.1	37.2	38.3	39.7
Total		217.0	225.8	236.8	247.8	261.3
Elastic modulus E, MPa		5.6	8.7	9.9	12.5	15.4
Specific gravity		1.219	1.246	1.273	1.315	1.337
Tensile strength, MPa		14.0	14.4	17.9	19.9	16.7
Breaking elongation, %		504.8	458.1	545.4	594.6	495.2
Tear strength, N/mm		75.9	77.3	78.0	85.5	72.3
Radius of curvature for hemisphere specimen, mm		5.28	5.29	5.24	5.24	5.22
Arithmetical mean height S_a for hemisphere specimen, μm		1.41	1.43	1.52	1.42	1.22
Dispersion term of surface free energy γ^d, mJ/m^2		24.1	24.6	25.9	24.8	26.0
Dispersion term of surface free energy γ^p, mJ/m^2		0.1	0.1	0.0	0.1	0.0
Surface free energy γ, mJ/m^2		24.2	24.7	25.9	24.9	26.0
Spreading coefficient contacting with glass in water S, mJ/m^2		−29.9	−29.9	−31.4	−30.0	−31.5

Table 7.3 Rubber composition in the second mixing process (unit: phr) and physical properties of rubbers with AC

		AC1	AC2	AC3	AC4	AC5	AC6	AC7	AC8
Masterbatch	MB1			178.9					
	MB2				186.6				
	MB3	196.5	196.5			196.5			196.5
	MB4						206.4		
	MB5							218.5	
Vulcanizing agent	Surfer	2.0	2.0	2.0	2.0	2.0	2.0	2.0	2.0
Vulcanization accelerator	Benzothiazolyl disulfide	1.0	1.0	1.0	1.0	1.0	1.0	1.0	1.0
	Tetramethylthiuram monosulfide	0.1	0.1	0.1	0.1	0.1	0.1	0.1	0.1
Pigment	Titanium oxide	37.5	37.8	35.9	37.0	38.1	39.2	40.6	38.3
Other	Activated carbon	2.0	4.1	5.6	5.9	6.2	6.5	6.9	8.3
Total		239.2	241.5	223.5	232.6	243.9	255.1	269.0	246.3
Activated carbon content, vol%		0.83	1.5	2.4	2.5	2.3	2.2	2.3	2.9
Elastic modulus *E*, MPa		6.6	6.6	4.2	5.4	6.8	8.6	14.3	6.9
Specific gravity									
Tensile strength, MPa		20.0	16.3	14.2	14.7	14.6	14.5	15.6	12.4
Breaking elongation, %		670.8	621.6	611.7	606.1	573.5	552.8	473.2	536.7
Tear strength, N/mm		70.9	69.0	36.4	43.1	57.9	68.8	74.8	39.7
Radius of curvature for hemisphere specimen, mm		5.21	5.21	5.24	5.22	5.24	5.22	5.24	5.29
Arithmetical mean height S_a for hemisphere specimen, μm		1.32	1.42	1.31	1.27	1.22	1.52	1.22	1.25
Dispersion term of surface free energy γ^d, mJ/m^2		24.1	24.7	25.7	24.1	26.0	25.7	25.8	25.8
Dispersion term of surface free energy γ^p, mJ/m^2		0.1	0.1	0.0	0.1	0.0	0.0	0.0	0.0
Surface free energy γ, mJ/m^2		24.2	24.8	25.7	24.2	26.0	25.7	25.8	25.8
Spreading coefficient contacting with glass in water *S*, mJ/m^2		−29.9	−29.9	−31.4	−29.9	−31.5	−31.4	−31.4	−31.4

Table 7.4 Rubber composition in the second mixing process (unit: phr) and physical properties of rubbers with SC

		SC1	SC2	SC3	SC4	SC5	SC6	SC7	SC8	SC9
Masterbatch	MB1			178.9						
	MB2				186.6					
	MB3	196.5	196.5			196.5			196.5	196.5
	MB4						206.4			
	MB5							218.5		
Vulcanizing agent	Surfer	2.0	2.0	2.0	2.0	2.0	2.0	2.0	2.0	2.0
Vulcanization accelerator	Benzothiazolyl disulfide	1.0	1.0	1.0	1.0	1.0	1.0	1.0	1.0	1.0
	Tetramethylthiuram monosulfide	0.1	0.1	0.1	0.1	0.1	0.1	0.1	0.1	0.1
Pigment	Titanium oxide	37.6	38.0	36.2	37.3	38.4	39.5	41.0	38.9	39.3
Other	Sodium chloride	4.1	8.2	11.7	12.1	12.5	12.8	13.3	16.8	21.2
Total		241.3	245.8	229.9	239.1	250.5	261.8	275.8	255.2	260.1
Sodium chloride content, vol%		1.0	2.0	3.0	3.0	3.0	3.0	3.0	4.0	5.0
Elastic modulus E, MPa		10.9	10.2	6.4	8.9	10.8	13.2	17.4	10.8	11.3
Specific gravity		1.307	1.319	1.271	1.293	1.323	1.323	1.343	1.320	1.328
Tensile strength, MPa		17.0	18.1	18.3	16.5	16.8	16.5	14.4	16.0	14.0
Breaking elongation, %		576.9	590.6	644.0	578.1	581.3	545.6	458.1	547.5	504.8
Tear strength, N/mm		75.7	74.5	77.2	71.3	77.0	70.9	75.5	71.7	67.9
Radius of curvature for hemisphere specimen, mm		5.24	5.22	5.23	5.21	5.25	5.27	5.25	5.24	5.23
Arithmetical mean height S_a for hemisphere specimen, μm		1.25	1.38	1.22	1.29	1.30	1.21	1.41	1.21	1.33
Dispersion term of surface free energy γ^d, mJ/m^2		25.2	24.5	24.5	24.4	24.9	24.7	25.1	24.4	24.1
Dispersion term of surface free energy γ^p, mJ/m^2		0.1	0.1	0.1	0.1	0.0	0.1	0.0	0.1	0.1
Surface free energy γ, mJ/m^2		25.3	24.6	24.6	24.5	24.9	24.8	25.1	24.5	24.2
Spreading coefficient contacting with glass in water S, mJ/m^2		−30.0	−29.9	−29.9	−29.9	−31.3	−29.9	−31.4	−29.9	−29.9

7.2.2 Friction test using hemisphere specimens

Using all hemisphere specimens (R1–5, AC1–8, and SC1–9), a friction test was conducted and contact condition was observed during the friction test. Fig. 7.2(a) shows a schematic of the experimental system. Each hemisphere specimen was perpendicularly approached to a water-covered glass surface (084.4L100-45DEG-6P-4SH3.5, SIGMAKOKI Co., Ltd., Saitama, Japan) at 1.00 mm/s using an electric cylinder (EASM4NXD010AZMC, Oriental Motor Co., Ltd., Japan), and within 0.01 s after the completion of contacting, the glass was slid horizontally and linearly at 1.00 mm/s using

another electric cylinder (EACM4D30AZAC, Oriental Motor Co., Ltd., Japan). The normal force was set at 0.196 N using dead weight, as shown in Fig. 7.2(a), and friction force was measured using a load cell (TL201Ts, Trinity-Lab Inc., Tokyo, Japan) at 1 kHz. Distributions of water, air, and real contacts were measured based on the intensity in the total reflection method and light interferometry [2], and the distribution of clearance between rubber and glass was quantified based on the intensity in the total reflection method [5]. As shown in Fig. 7.2(a), in the total reflection method, red light from a light-emitting diode (LED, HLV2-22RD-3W, CCS Inc., Kyoto, Japan) penetrated the glass and was totally reflected in the glass (reflect angle was set at 65°) using a light guide (LE-OPT-24, OPTEC FA Co., Ltd., Kyoto, Japan) and a mirror (RPB3-20-550, SIGMAKOKI Co., Ltd., Saitama, Japan). In light interferometry, blue light from the LED (HLV2-22BL-3W, CCS Inc., Kyoto, Japan) was perpendicularly inserted to the interface between the hemisphere specimen and glass plate through a

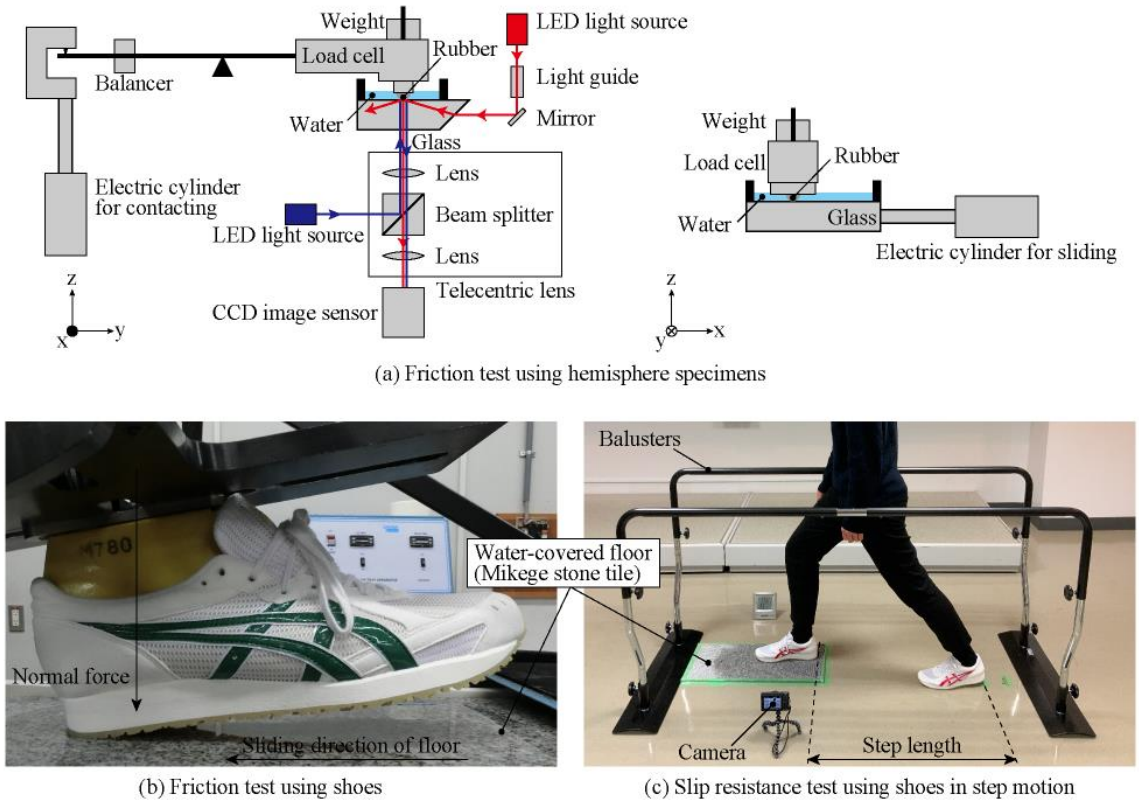

Fig. 7.2 Schematic of the experimental system: (a) friction test using hemisphere specimens; (b) friction test using shoes with a slip meter; (c) slip resistance test using shoes under stepping motion.

telecentric lens (TV-2F-110, OPTART Co., Ltd., Tokyo, Japan). The reflected light in both the total reflection method and light interferometry was observed by a charge-coupled device camera (AT-030MCL, JAI Ltd., Yokohama, Japan) at 12 bit and 100 fps. The pixel size corresponded to 3.6 μm × 3.6 μm. In this Chapter, friction and observation tests for each condition were conducted 5 times. The friction force and contact condition were measured at d = 0–10.00 mm, and the mean values and the standard deviation of each parameter were obtained from the results measured at d = 5.00–10.00 mm. The atmospheric temperature and relative humidity were set at 21.8 °C and 68%, respectively.

7.2.3 Friction test using shoes with a slip meter

Using the right shoes with all rubbers, as shown in Fig. 7.2(b), a friction test was conducted with a slip meter (SATRA TM144, SATRA Technology Centre Ltd., Kettering, UK) based on the ISO standard [6]. As the toe of the shoe did not contact the water-covered smooth Mikage stone tile (G603 White, Sakae shokai Co., Ltd., Tajimi, Japan), the angle between the outer sole and floor was set at 7°. The surface roughness of the floor was measured by a roughness meter (SV-3000S4, Mitutoyo Corporation, Kawasaki, Japan), and S_a = 0.070 μm. The normal force, sliding velocity, and sliding distance (d) were set at 500 N, 300 mm/s, and 200 mm, respectively. Based on ISO 13287, the friction test for each outer sole was conducted 10 times, and the mean values and the standard deviations of friction coefficient (μ) were calculated from the results in the 6^{th}–10^{th} trials at d = 100–200 mm. The atmospheric temperature and relative humidity were 22.6 °C and 37 %, respectively.

7.2.4 Slip resistance test using shoes under a stepping motion

Using right shoes with outer soles of R1, 3, 5, AC3, 5, 7, and SC3, 5, 7, the slip resistance under stepping motion was measured, as shown in Fig. 7.2(c). The water-covered smooth Mikage tile was used as the floor in the friction test. 11 healthy young male adults (age: 22–36 years, height: 1.65–1.91 m, body mass: 52–76 kg, dominant foot: right or left) participated in this trial. All experiments were performed in accordance with relevant guidelines and regulations. The participants were informed of the protocol, and informed consent was obtained from each participant before the experiment. The

protocol was approved by the Institutional Review Board of Tohoku University. The participants were asked to wear each shoe and stood still; then, they were asked to step forward with a step length of 0.60, 0.70, and 0.80 m. Here, subjects were instructed to make heel contact with the floor in the stepping motion. While the stepping motions were conducted continuously 20 times for each outer-sole step length, the order of the trial condition was randomized. The contact between the shoe and floor in the stepping motion was observed by a digital camera (PowerShot SX700 HS, Sony, Tokyo, Japan) at 60 fps. In this Chapter, whether a slip occurred or not was defined as whether the slipping distance was more than 0.03 m or not, based on a previous study [7]. To easily judge the slipping distance by a movie during the stepping motion, parallel lines orthogonal to the stepping direction were printed every 0.010 m on the floor. The mean value and standard division of the slip rate for each condition (9 outer soles and 3 step lengths) were quantified based on the results of 220 steps (11 subjects × 20 steps). To avoid slip-and-fall accidents during the test, balusters (P-2, Mutsumi Medical Co., Ltd., Osaka, Japan) were set on both sides of the subjects, but they were asked to not touch the balusters before making heel contacts. The temperature and relative humidity were 17.0 °C and 33 %, respectively.

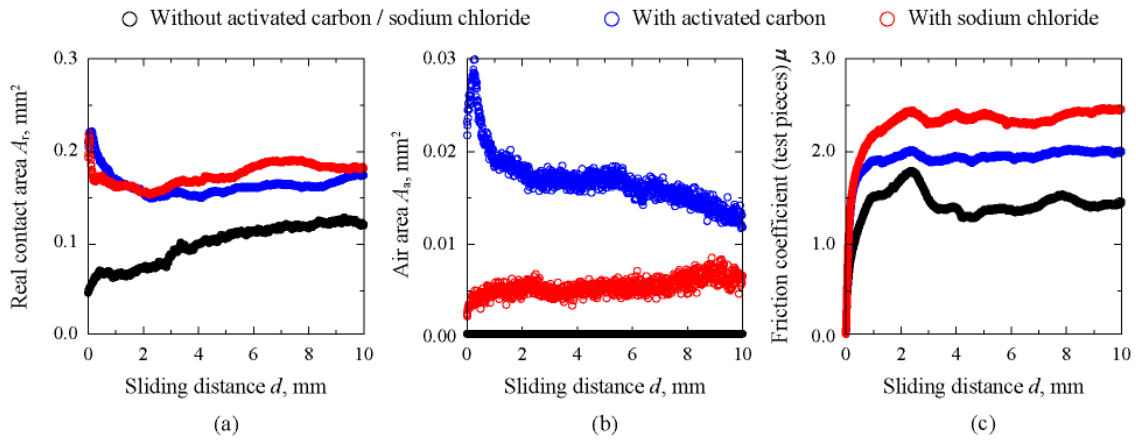

Fig. 7.3 Changes in the real contact area (A_r), air area (A_a), and friction coefficient (μ) in the friction test using hemisphere specimens for R1, AC3, and SC3.

7.3 Results and discussion

7.3.1 Friction behaviors of hemisphere specimens

Fig. 7.3 shows the changes in real contact area (A_r), air area or air-covered area (A_a), and friction coefficient (μ) during the friction test using hemisphere specimens for R1, AC3, and SC3. Focusing on the rubber without AC or SC, A_r for R1 increased during the friction test, but the increasing rate of A_r slightly decreased at d = 5.00–10.00 mm. μ for R1 was relatively unstable at d = 0.00–5.00 mm and became stable at d = 5.00–10.00 mm, and A_a = 0.00 mm^2 at d = 0.00–10.00 mm. Moreover, the rubbers with AC or SC and A_r for AC3 and SC3 decreased at d = 0.00–1.00 mm and slightly increased at d = 1.00–10.00 mm, whereas μ was stable during the friction test at d = 2.00–10.00 mm. Interestingly, A_a values for these rubbers were nonzero during the friction test. Fig. 7.4 shows the distribution of real contacts (red), air-covered area (white), and water-covered area (blue) for R1, AC3, and SC3 at d = 5.00 mm. For all rubbers, many real contacts were formed within an elliptic shape, whose minor axis was parallel to the sliding direction. This resulted in the macroscopic strain in each hemisphere specimen, as explained in previous studies [8,9]. Air bubbles were formed only for the rubbers with AC and SC. It is considered that air in each air bubble was leaked from air pockets on the rubber surface. Even in the friction tests using hemisphere specimens, which were continuously conducted 5 times within a few minutes, air bubbles were always observed for the rubbers with AC

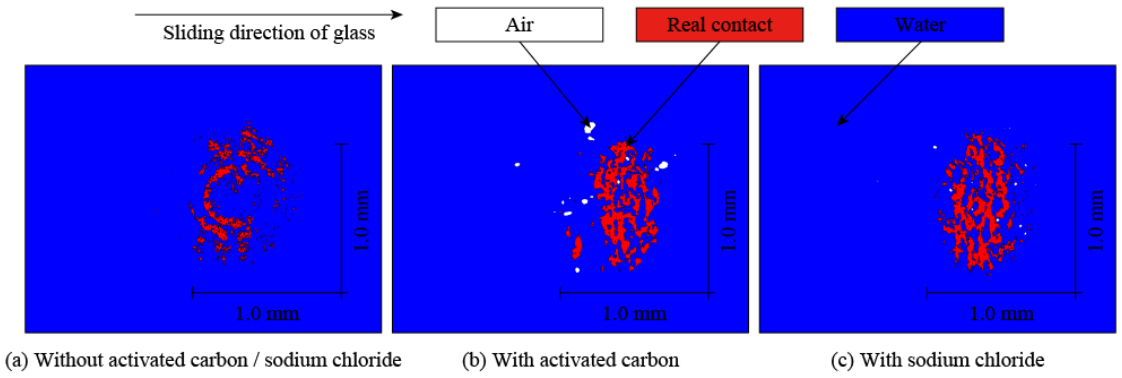

Fig. 7.4 Distribution of real contact, air bubble, and water at d = 5.00 mm in friction tests using hemisphere specimens R1, AC3, and SC3.

and SC. This result explains that the air in the air pockets was not completely replaced with water and that the air pockets continuously supplied air to the interface between the two substrates. In addition, each real contact was surrounded by water, as observed previously [2].

Figs. 7.5(a–c) indicate the mean values and standard distributions of A_r, A_a, and μ, respectively, for R1–5 (rubbers without AC or SC), AC3–7 (rubbers with AC), and SC3–7 (rubbers with SC) versus elastic modulus (E). It was confirmed that A_r for all rubbers decreased with E and that A_r tended to increase with the addition of AC and SC, especially for E < 10 MPa. In addition, while no air bubble was confirmed for rubbers without AC or SC, air bubbles were confirmed for rubbers with AC and SC, and A_a decreased with E. The negative correlations between A_r and E can be explained based on the Hertz contact theory in which low E enlarges the apparent contact area, A_0. The negative correlations between A_a and E for rubbers with AC and SC can also be explained based on the Hertz contact theory because the increase in A_0 enlarges the potential area where air bubbles are formed. In addition to the dependency of A_r on E, Fig. 7.5 shows negative correlations between μ and E, and μ increased by adding AC and SC, especially for E < 10 MPa. Fig. 7.6 shows A_r, A_a, and μ for R3 (rubbers without AC or SC), AC1, AC2, AC5, AC8 (rubbers with AC), SC1, SC2, SC5, SC8, and SC9 (rubbers with SC) plotted against the amount of AC and SC used. Fig. 7.6(b) shows that air bubbles were formed by

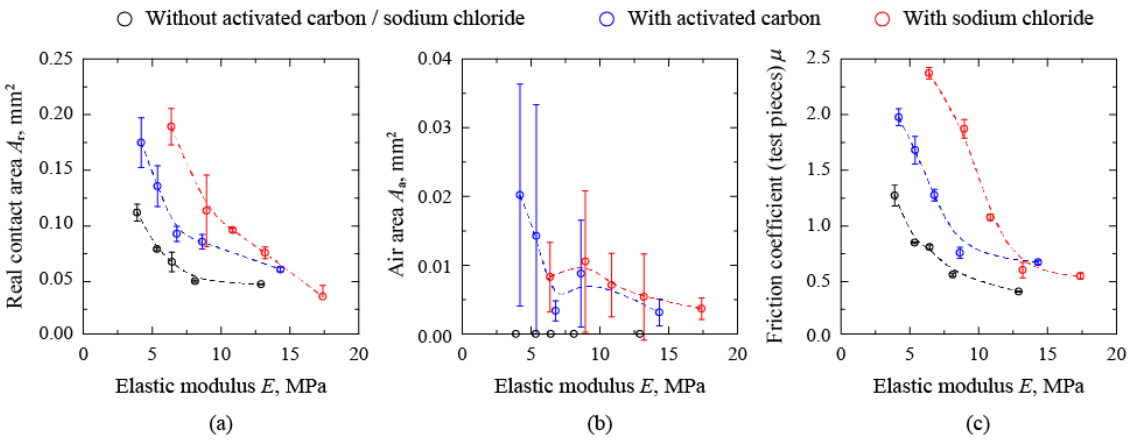

Fig. 7.5 Influence of elastic modulus (E) on the real contact area (A_r), air area (A_a), and friction coefficient (μ) in friction test using hemisphere specimens R1–5, AC3–7, and SC3–7.

adding AC and SC, but A_a did not always increase with AC and SC content. But as explained in Figs. 7.6(a,c), A_r and μ increased with AC and SC content. These results indicate that A_r and μ increased by adding AC and SC, but this effect was not linked to the amount of air between the two substrates. Fig. 7.7 shows the proportional relationship between μ and A_r for all conditions. This result suggests that the adhesion term was dominant in the friction test [10,11]. Thus, the real contact formation was promoted by adding AC and SC, which led to an increase in μ.

7.3.2 Theoretical modeling of dewetting with air bubbles in water

The real contacts of a soft material on a floor, as shown in Fig. 7.8(a), expand thermodynamically when the spreading coefficient (S) has a negative value for lubricated conditions or the work of adhesion (W) has a positive value for unlubricated conditions, and this phenomenon is called the dewetting effect [12–14]. S and W correspond to the parameter to quantify wettability between rubber and floor under unlubricated and lubricated conditions, respectively, and these parameters can be calculated from the following equations [3,15]:

$$W = (\gamma_R + \gamma_G) - \gamma_{RG} \tag{7.1}$$

$$S = \gamma_{RG} - (\gamma_{RW} + \gamma_{GW}) \tag{7.2}$$

where the subscripts R, G, and W correspond to rubber, glass, and water, respectively, γ_i is the surface free energy of material i, and γ_{ij} is the interfacial free energy between materials i and j. According to the Kaelble and Uy theory, γ_i is defined as the sum of the dispersion term γ_i^d and polar term γ_i^p ($\gamma_i = \gamma_i^d + \gamma_i^p$), and γ_{ij} is obtained by the following equation [3,4]:

$$\gamma_{ij} = \left(\sqrt{\gamma_i^d} - \sqrt{\gamma_j^d}\right)^2 + \left(\sqrt{\gamma_i^p} - \sqrt{\gamma_j^p}\right)^2 \tag{7.3}$$

The dewetting effect is explained based on the free energy of the system (G), which is a convex quadratic function of the real contact size R in the following equation [12,13]:

$$G \propto -|S|R^2 + Ee^2R \tag{7.4}$$

where e indicates the clearance between two substrates. This equation explains that the real contact thermodynamically expands once R exceeds $R_c = Ee^2/|S|$ because the value of G and the increasing rate of G gets negative. It has been theoretically and experimentally reported that real contact formation can be promoted as R_c decreases [2]. In addition, this theory has been developed to explain a nonuniform wetting state in the presence of air bubbles between two substrates in water, and the real contacts were surrounded by the water meniscus, as shown in Fig. 7.8(b) [2]. G and R_c for this condition are obtained using the following equations [2]:

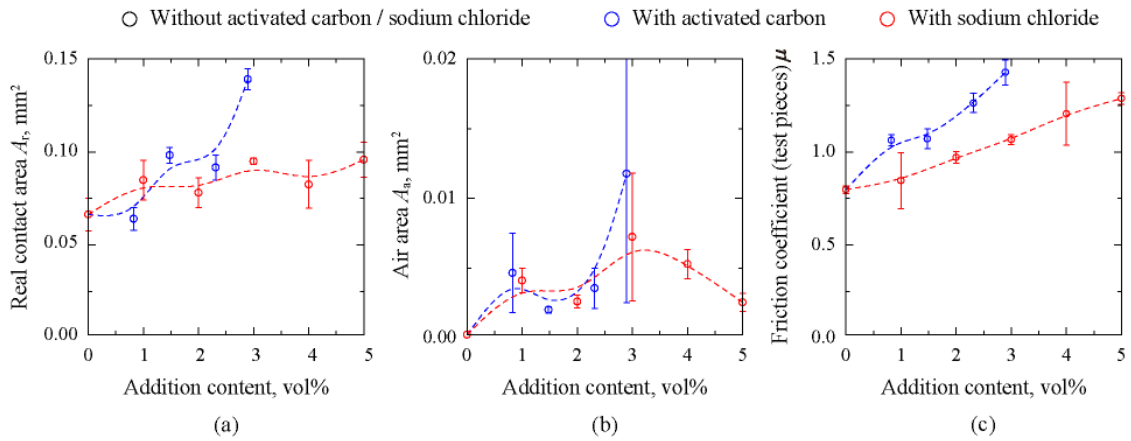

Fig. 7.6 Real contact area (A_r), air area (A_a), and friction coefficient (μ) versus the content of AC and SC in friction tests using hemisphere specimens of R3, AC1, AC2, AC5, AC8, SC1, SC2, SC5, SC8, and SC9.

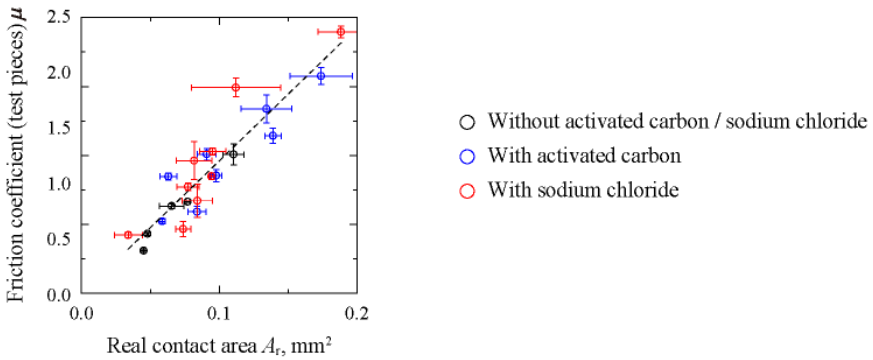

Fig. 7.7 Relationship between the friction coefficient (μ) and real contact area (A_r) in friction tests using hemisphere specimens.

$$G \propto -(2W + S)R^2 + Ee^2R \tag{7.5}$$

$$R_c = \frac{Ee^2}{2W + S} \tag{7.6}$$

If the pressure in the water meniscus is negative, that is, if $\cos\theta_R + \cos\theta_G > 0$, $Ee^2/|S| > Ee^2/(2W + S)$. Thus, if $\cos\theta_R + \cos\theta_G > 0$, R_c is decreased by adding air bubbles between two substrates in water, and the dewetting effect is promoted. Here, θ_i is the contact angle of water on material i. Eqs. (7.5,7.6) also explain that the dewetting effect is sensitive to the value of e. However, as shown in Fig. 7.8(c), e is not always constant, depending on the volume of the water meniscus. Thus, the clearance at the outer edge of the water meniscus (e_{w1}) can be larger than that at the edge of the real contact (e_{w0}). Considering that the pressure in the water meniscus is determined by e_{w1}, the values for G and R_c for $e_{w0} \neq e_{w1}$ can be determined by the following equations:

$$G \propto -\left\{2\frac{e_0}{e_1}W + \left(2\frac{e_0}{e_1} - 1\right)S\right\}R^2 + e_0^2ER \tag{7.7}$$

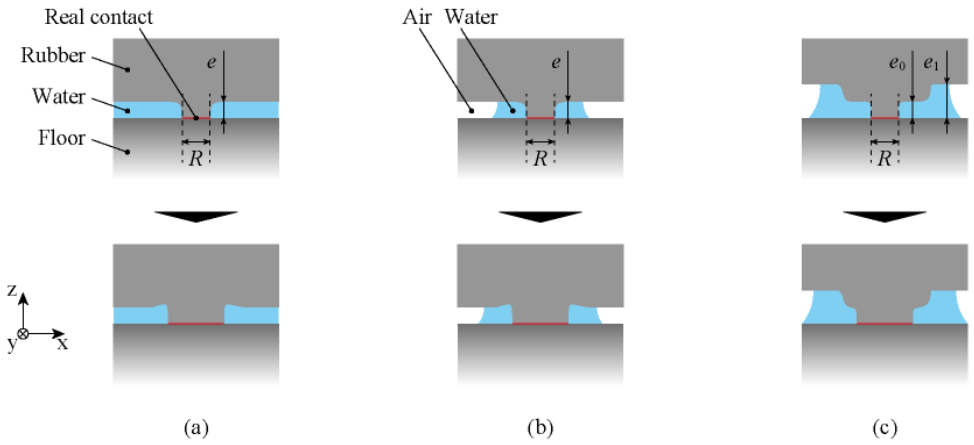

Fig. 7.8 Schematic of real contact formation based on the dewetting effect: (a) uniform wetting; (b) nonuniform wetting but uniform clearance in the water meniscus; (c) nonuniform wetting and nonuniform clearance in the water meniscus.

$$R_c = \frac{e_0^2 E}{2\frac{e_0}{e_1}W + \left(2\frac{e_0}{e_1} - 1\right)S} \tag{7.8}$$

7.3.3 Influence of the dewetting effect on real contact formation and friction behavior

As confirmed in Fig. 7.4, the real contacts were surrounded by a water meniscus for the rubbers with AC and SC. Thus, R_c for the rubbers with AC and SC can be estimated based on Eq. 7.8, while R_c for the rubbers without AC and SC can be defined as $R_c = Ee_0^2/|S|$. Fig. 7.9 shows the histogram of e around real contacts for the hemisphere specimens of R1, AC1, and SC1 and the histogram of e at the outer edge of the water meniscus for the hemisphere specimens of AC1 and SC1. The value of e on each pixel around real contacts and those at the outer edges of the water meniscus were extracted from the measured distribution of e at d = 5.00–10.00 mm using MATLAB software (R2016b, The MathWorks, Inc.). Fig. 7.9 shows that each histogram had a peak. In this Chapter, the peak value for the histogram of clearance around real contacts and that at the outer edges of the water meniscus were defined as e_0 and e_1, respectively. Fig. 7.10 shows the influences of elastic modulus (E) and the addition amount of AC and SC on R_c calculated from S, W, e_0, and e_1. It was confirmed that R_c increased with E and decreased with AC and SC content. Especially for E < 10 MPa and by adding SC, R_c drastically decreased. In Fig. 7.11, A_r and μ are plotted against R_c. Overall, A_r and μ decreased with R_c. Because A_r and μ can

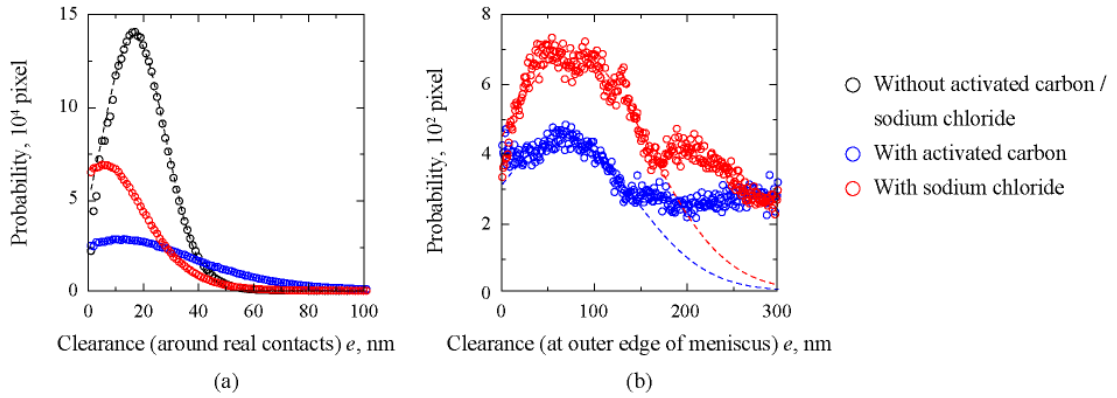

Fig. 7.9 Histograms of clearance around real contacts and at the outer edges of the water meniscus in friction tests using the hemisphere specimens of R1, AC3, and SC3.

increase with the apparent contact area (A_0), which was determined by E in the Hertz contact theory, the real contact ratio, A_r/A_0, and the shear strength, τ (friction force divided by A_0), were calculated and plotted against R_c, as shown in Fig. 7.12. Fig. 7.12 indicates more clear negative correlations in A_r/A_0–R_c and τ–R_c curves in comparison with A_r–R_c and μ–R_c curves in Fig. 7.11. These results suggested that real contact formation based on the dewetting effect was promoted as R_c decreased and that τ increased with the promotion of real contact formation. Therefore, considering that the real contact formation was promoted by adding AC or SC to rubber, especially at E < 10 MPa and that A_0 decreased with E, it is reasonable to add AC or SC to rubber to achieve high friction.

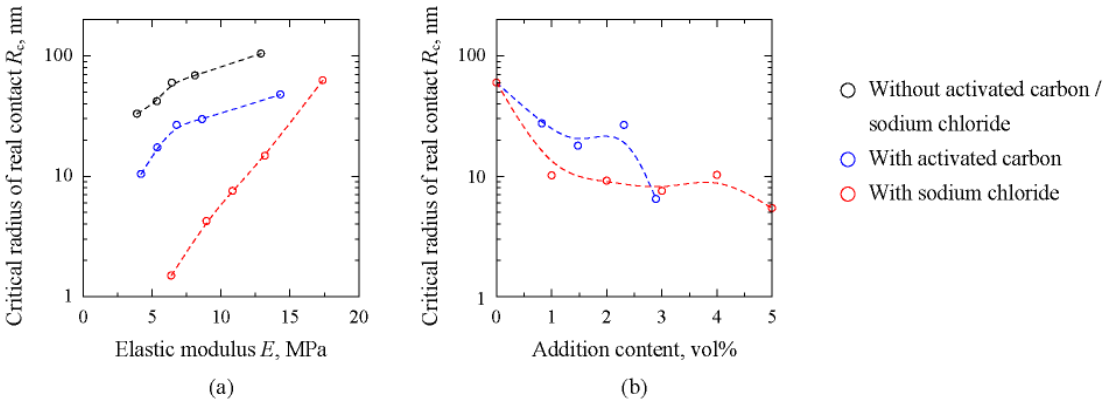

Fig. 7.10 Critical radius of real contact (R_c) versus elastic modulus (E) and content of AC and SC in friction tests using hemisphere specimens: (a) R1–5, AC3–7, and SC3–7; (b) R3, AC1, AC2, AC5, AC8, SC1, SC2, SC5, SC8, and SC9.

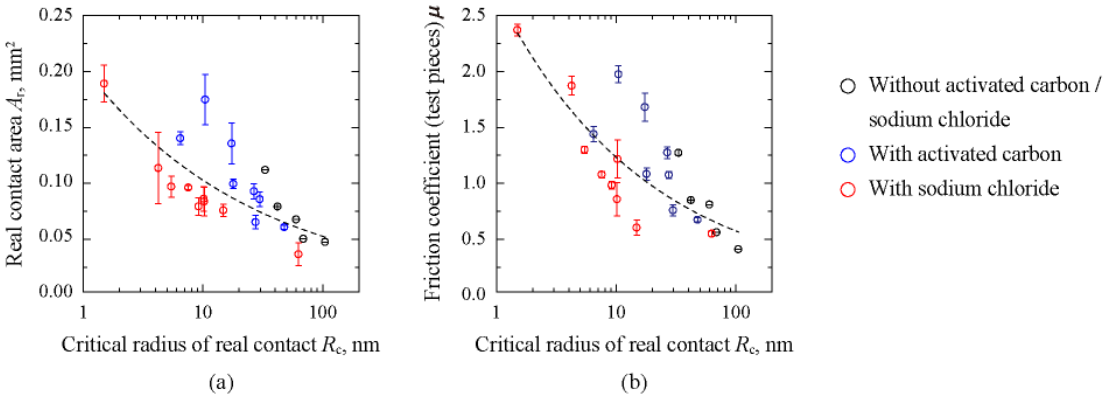

Fig. 7.11 Real contact area (A_r) and friction coefficient (μ) versus critical radius of real contact (R_c) in friction tests using all hemisphere specimens.

7.3.4 Friction behaviors of shoes

Figs. 7.13(a) and (b) show the influences of E and AC and SC content on μ for the shoes with outer soles of R1, R3, E5, AC3, AC5, AC7, SC3, SC5, and SC7. Similar to the friction test results using hemisphere specimens, μ decreased with E, increased with AC and SC content, and the high-friction effect of AC and SC addition was high, especially for E < 10 MPa. For example, focusing on R1, AC3, and SC3 (rubbers of the softest masterbatch, MB1, without/with AC or SC), μ increased by +52.8% and +46.9% by adding AC and SC, respectively. Fig. 13(c) indicates a positive correlation between μ values for shoes and hemisphere specimens, but this correlation was not

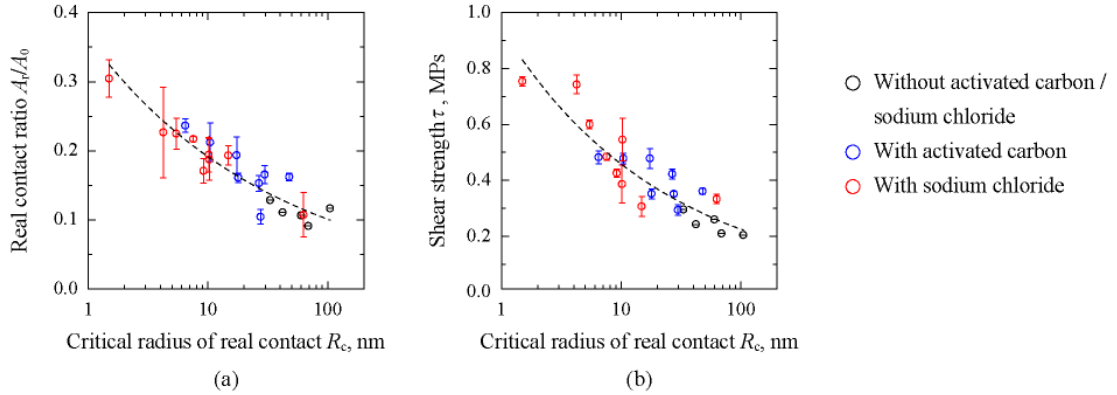

Fig. 7.12 Real contact ratio (A_r/A_0) and shear strength (τ) versus critical radius of real contact (R_c) in friction tests using all hemisphere specimens.

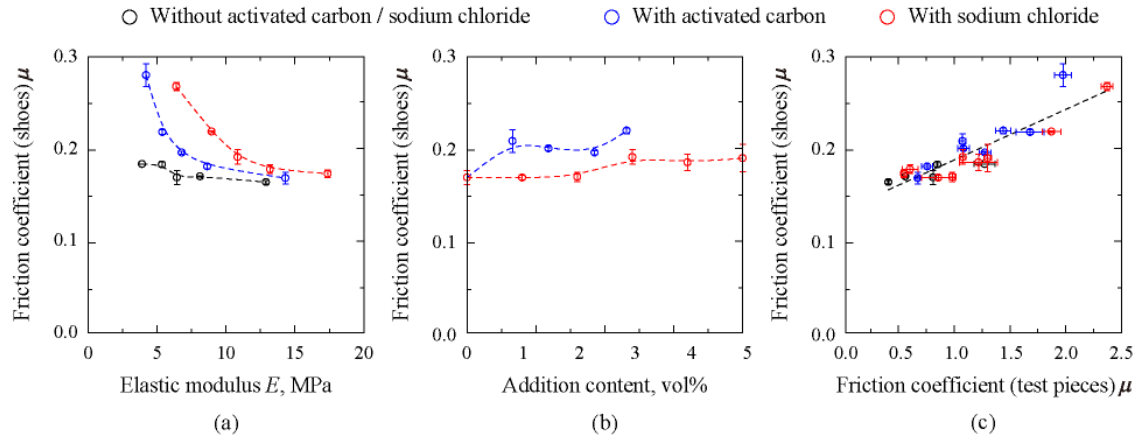

Fig. 7.13 Influences of elastic modulus (E) and AC and SC content on the friction coefficient (μ) in friction tests using shoes and the relationship between friction coefficients (μ) using shoes and hemisphere specimens for all rubbers.

proportional, and the value range of μ for shoes was narrow in comparison with that for hemisphere specimens. These results suggest that AC and SC addition enlarged μ for shoes, especially for E < 10 MPa, but the absolute values of μ for shoes were small because of the differences in the contact pressure, sliding velocity, and macroscopic geometry in comparison with those obtained using hemisphere specimens.

7.3.5 Slip rate of shoes in stepping trial

Figs. 7.14(a–c) show the slipping rate (Φ) in stepping motion using shoes with outer soles of R1, R3, R5, AC3, AC5, AC7, SC3, SC5, and SC7 versus E when the step length was set at 0.60, 0.70, and 0.80 m, respectively, and explain that Φ for all shoes increased with E, and this dependency became more significant with the increased step length, especially for the rubber without AC and SC. In addition, Φ decreased by adding AC and SC. Fig. 7.15 indicates the relationship between Φ and μ for shoes. Φ drastically decreased at μ < 0.19 and got saturated at $\mu \geq 0.19$, regardless of the step length, and the convergence value of Φ at $\mu \geq 0.19$ increased with the step length. These results indicate that the higher the value of μ, the lower the risk of slipping at μ < 0.19, and that the risk of slipping at $\mu \geq 0.19$ was not zero and increased with the step length, likely due to the uncertainties of human motion related to the stepping speed, the angle of heel contact, and the lean angle of the body.

7.3.6 Statistical analysis of the relationship between the slipping rate and friction coefficient

As mentioned in Chapter 7.3.5, Φ drastically decreased with μ. Here, assuming the relationship between Φ and μ for shoes is approximated by a Gaussian function, this relationship can be described by the mean value of the friction coefficient, μ_0, the standard deviation of the friction coefficient, σ, and the convergence value of the slipping rate Φ_0:

$$\Phi = (1 - \Phi_0)\frac{2}{\sqrt{\pi}}\int_{\frac{\mu-\mu_0}{\sigma}}^{\infty} e^{-t^2}\,\mathrm{d}t + \Phi_0 = (1 - \Phi_0)\mathrm{erfc}\left(\frac{\mu - \mu_0}{\sigma}\right) + \Phi_0 \tag{7.9}$$

The values of μ_0, σ, and Φ_0 for each stepping length were determined by fitting the measured and estimated values of Φ based on the least-squares method. The calculated Φ–μ curves are plotted as the dashed lines in Fig 7.15, and the calculated values of μ_0, σ, and Φ_0 are listed in Table 7.5. Fig. 7.15 suggests that measured results were overall plotted on the fitting curves and that this fitting method would be reasonable. Here, it is considered that Φ is constant and minimum at $\mu \geq \mu_0 + 3\sigma$. Since $\mu_0 + 3\sigma$ = 0.181–0.189, as shown in Table 7.5, it is desirable to make μ more than 0.189 to minimize the slipping risk in stepping motion. Fig. 7.13(a) indicates that μ values of shoes were more than 0.189 for

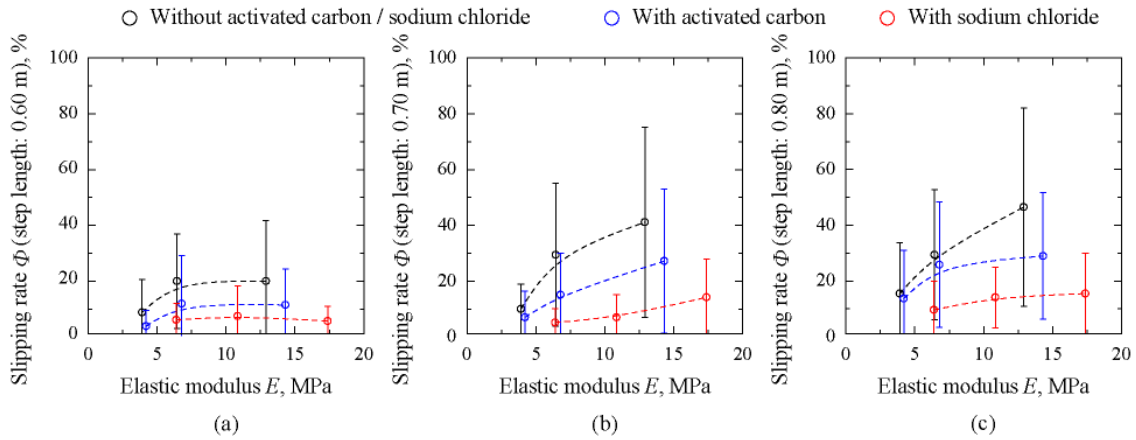

Fig. 7.14 Slipping rate (Φ) versus elastic modulus (E) for R1, R3, R5, AC3, AC5, AC7, SC3, SC5, and SC7.

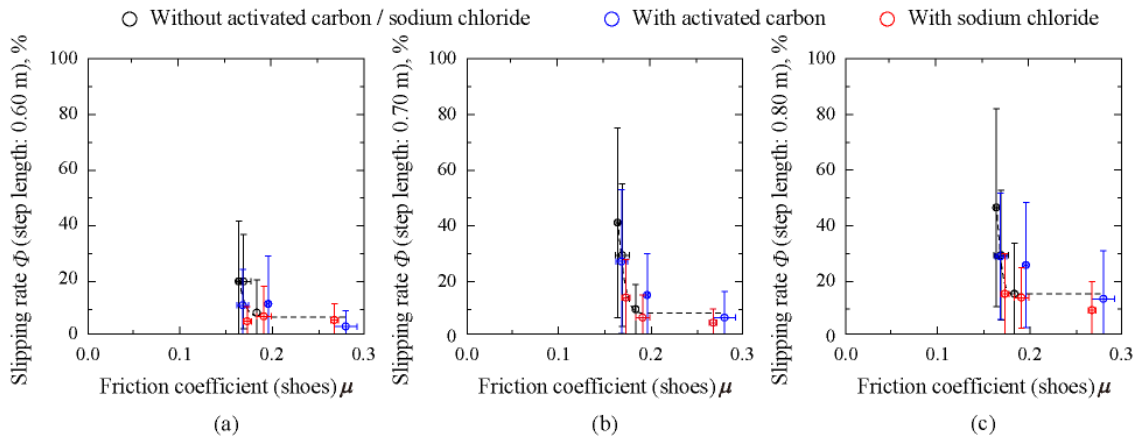

Fig. 7.15 Slipping rate (Φ) versus friction coefficient (μ) using shoes with outer soles of R1, R3, R5, AC3, AC5, AC7, SC3, SC5, and SC7.

the rubbers with AC and SC for E < 10 MPa. For the outer soles containing the same masterbatch MB3 (R3, AC5, and SC5), μ measured using shoes were 0.169, 0.196, and 0.191, respectively. Focusing on the case when the step length was 0.70 m (Fig. 7.15(b)), Φ was 28.6% for R3 and decreased to 14.1 and 5.9% with the addition of AC and SC, respectively. In addition, Φ for AC5 and SC5 further decreased to 5.9 and 4.1%, respectively, by setting E < 10 MPa. Therefore, it is expected that adding AC or SC to rubber (especially for E < 10 MPa) can reduce the slipping risk in practical use.

Table 7.5 Calculated parameters in Φ–μ curves

Stepping length, m	0.6	0.7	0.8
mean value of friction coefficient μ_0	0.152	0.161	0.162
standard deviation of friction coefficient σ	0.0113	0.00945	0.00651
convergence value of slipping rate Φ_0	0.0622	0.0748	0.145
$\mu_0 + 3\sigma$	0.186	0.189	0.181

7.4 Conclusions

To develop high-friction rubber for shoe outer soles that can be safely used even on a wet smooth floor, it is reasonable to form air bubbles between the rubber outer sole and floor. Adding AC or SC to diene rubbers can help since air pockets (small pares) are formed on the rubber surface and can supply air into the interface between the two substrates, forming a nonuniform wetting state. In this Chapter, rubbers without/with AC and SC were prepared, and their friction properties were investigated using hemisphere specimens and shoes. In addition, the slip resistances of the shoes in stepping motion were also investigated. The experimental results using hemisphere specimens indicate that air bubbles were formed between the rubbers and floor by adding AC or SC and that the real contact formation was promoted, and high friction was achieved especially when the elastic modulus (E) was less than 10 MPa. The high-friction effect, especially for E < 10 MPa, was also confirmed for the friction of shoes. In addition, the slipping rate in stepping motion decreased by adding AC and SC, especially for E < 10 MPa. The slip risk in step motion (for 0.70 m) decreased from 28.6% to 14.1 and 5.9% by adding

AC and SC, respectively, and these values further decreased to 5.9 and 4.1%, respectively, by setting E < 10 MPa. In conclusion, using additives such as AC or SC in rubber for shoe outer soles is a viable method to achieve high slip resistance and reduce slip accidents.

References

[1] Nishi T., Yamaguchi T., Shibata K., and Hokkirigawa K., "Optimizing the Frictional Behavior of Partially Wetting Soft Contacts as Measured with Hydrogel Covered Silicones," Tribology International, 153, 2021, 106586.

[2] Nishi T., Yamaguchi T., Shibata K., and Hokkirigawa K., "Friction Behavior of Silicone Rubber Hemisphere under Non-Uniform Wetting States: With Water Droplets in Air or Air Bubbles in Water," Tribology International, 155, 2021, 106769.

[3] de Gennes P.-G., Brochard-Wyart F., and Quéré D., Special Interfaces. Capillarity Wetting Phenom. Drops, Bubbles, Pearls, Waves, New York, NY, Springer New York, 2004, p. 215–59.

[4] Kaelble D.H., "Dispersion-Polar Surface Tension Properties of Organic Solids," Journal of Adhesion, 2, 2, 1970, 66–81.

[5] Nishi T., Moriyasu K., and Nishiwaki T., "Precise Measurement of Clearance between Two Substrates Using Evanescent Waves," Tribology Online, 12, 5, 2017, 251–6.

[6] ISO 13287: 2007 Personal Protective Equipment – Footwear -Test Method for Slip Resistance.

[7] Yamaguchi T., Hsu J., Li Y., and Maki B.E., "Efficacy of a Rubber Outsole with a Hybrid Surface Pattern for Preventing Slips on Icy Surfaces," Applied Ergonomics, 51, 2015, 9–17.

[8] Sahli R., Pallares G., Ducottet C., Ben Ali I.E., Al Akhrass S., Guibert M., et al., "Evolution of Real Contact Area under Shear and the Value of Static Friction of Soft Materials," Proceedings of the National Academy of Sciences of the United States of America, 115, 3, 2018, 471–6.

[9] Sahli R., Pallares G., Papangelo A., Ciavarella M., Ducottet C., Ponthus N., et al., "Shear-Induced Anisotropy in Rough Elastomer Contact," Physical Review Letters,

122, 21, 2019, 214301.

[10] Bowden F.P., and Tabor D., “The Friction and Lubrication of Solids Part II,” Physics Today, 17, 6, 1964, 72.

[11] Moore D.F., and Geyer W., “A Review of Adhesion Theories for Elastomers,” Wear, 22, 2, 1972, 113–41.

[12] Martin P., Silberzan P., and Brochard-Wyart F., “Sessile Droplets at a Solid/Elastomer Interface,” Langmuir, 13, 18, 1997, 4910–4.

[13] Martin P., and Brochard-Wyart F., “Dewetting at Soft Interfaces,” Physical Review Letters, 80, 15, 1998, 3296–9.

[14] Momozono S., Iguchi Y., Oshikiri K., Nakamura K., and Kyogoku K., Effects of interfacial free energy on adhesive friction behavior of elastomer surfaces under wet conditions. 5th World Tribol. Congr., vol. 4, 2013, p. 3208–11.

[15] Nishi T., “Effects of Wettability on Tribology of Soft Matter,” Toraibarojisuto/Journal of Japanese Society of Tribologists, 64, 10, 2019, 588–93.

Chapter 8

Conclusions

In this thesis, to develop rubber materials for outer-soles with high slip resistance even on a smooth wet floor, the friction behavior between rubber and floor was investigated by focusing on the effect of real contact formation caused by the dewetting effect. In addition to the dewetting effect for uniform wetting states (rubber on the floor in lubricant), the dewetting effect for nonuniform wetting states was investigated. The main results and conclusions in Chapters 2–7 are summarized below.

Chapter 2 demonstrates the research to establish a new experimental system for observing the contact condition between rubber and floor: distributions of real contacts and clearance. The optical system for the total reflection method and light interferometry was prepared, and the contact condition of a wedge between polypropylene and glass sheets was observed. It was confirmed that the intensity in the total reflection method drastically decreased with the increase in the clearance between the two substrates, which explains that the intensity of scattered light in the total reflection method was determined by an evanescent field above the glass surface. Thus, clearance could be determined based on the decay behavior in the total reflection method. Fig. 8.1 illustrates the summarized results for Chapter 2.

In Chapter 3, the rubber hemisphere approached the glass plate for lubricated conditions, and the interface between them was optically observed in the total reflection method and light interferometry. The experimental result indicated that each real contact expanded with time, and the real contact ratio increased as the contact time increased, but the increasing rate slowed down. The expansion of each real contact is explained based on the theory of dewetting effect, which indicates that the dewetting effect increased with the product of characteristic dewetting velocity and contact time. Considering that the contact time is inversely proportional to the contacting velocity, the positive correlation between the real contact area and the ratio of characteristic dewetting and contacting velocities was

obtained. Fig. 8.2 illustrates the summarized results for Chapter 3.

In Chapter 4, besides the contact process between a rubber hemisphere and a glass plate, the contact condition and friction behavior between them were also investigated. Real contacts were observed in processes of contacting and sliding. Because the real contacts can thermodynamically expand by a dewetting effect, which is determined by the product of characteristic dewetting velocity and time, the real contact formation was promoted by the increase in the ratio of characteristic dewetting and contacting velocities and the ratio of characteristic dewetting velocity and sliding velocity. Besides, the friction coefficient increased with the real contact area. Fig. 8.3 illustrates the summarized results for Chapter 4.

In Chapter 5, rubber hemispheres with hydrogel patches with/without different sizes were prepared to form nonuniform wetting states between the rubbers and the glass plate because rubber (silicone rubber) and hydrogel (polyvinyl alcohol) are hydrophobic and hydrophilic, respectively. By observing the contact conditions between two substrates, water was localized under a hydrogel patch, and real contacts were formed around the hydrogel during the friction. Experimental results show that the real contact area and friction coefficient were the highest when the hydrogel size was approximately 100 μm, and these parameters decreased with the size of hydrogel. Considering that the real contacts were formed around the hydrogel, the theory of dewetting effect was developed, which can explain such a high friction effect. Fig. 8.4 illustrates the summarized results for Chapter 5.

In Chapter 6, rubber friction for nonuniform wetting between rubber and floor was investigated by setting water droplets in air and air bubbles in the water. To ensure such conditions, rubber hemispheres were prepared with a moist hydrogel patch and an air pocket. The observation of contact conditions indicated that the intended nonuniform wetting states were formed and the water meniscus surrounded real contacts. It is theoretically predicted that the negative pressure in the meniscus would promote the dewetting effect, decreasing the critical radius of real contact. By experimentally measuring the critical radius of real contact, it was confirmed that low critical radii of real contact for

nonuniform wetting states promoted real contact formation and resulted in a high friction coefficient. Fig. 8.5 illustrates the summarized results for Chapter 6.

In Chapter 7, to achieve high friction by forming nonuniform wetting states, rubbers with/without activated carbon or sodium chloride were molded as hemispherical specimens and outer-sloes. As intended, air pockets (small pores) were formed on the rubber surface by adding these additives, and air bubbles were formed between two substrates. It was confirmed that the friction coefficient for both hemispherical specimens and outer-sole increased after adding the additives, especially for soft rubber, and the increase in friction coefficient decreased the slip risk in the step motion. Fig. 8.6 illustrates the summarized results for Chapter 7.

Therefore, in conclusion, adding activated carbon or sodium chloride to rubber would be reasonable to develop it for outer-soles with high slip resistance.

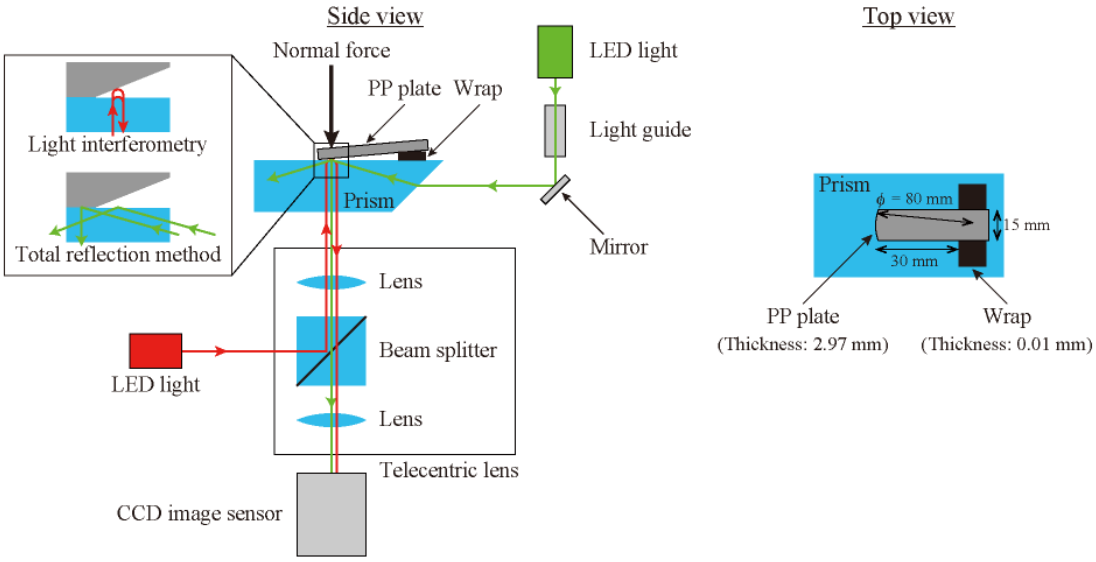

(a) Schematic of the experimental system for ovserving the interfece of a wedge between a polypropylene plate and a glass plate in a total reflection method and light interferomety using light with different wave length.

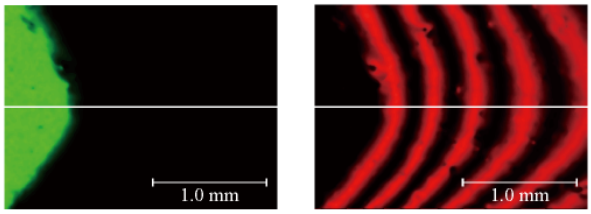

(b) Ovserved images in the total reflection method (green) and the light interferometry (red).

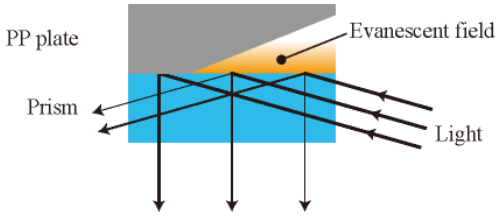

(c) Scematic view of an evanscent field frormed on the glass plate in the total reflectoin method.

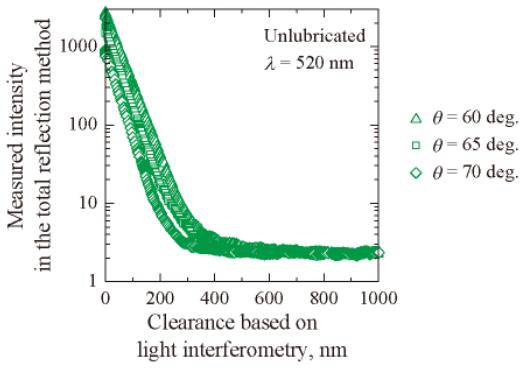

(d) Intensity measured in the total reflection method plotted against sclearance quantified based on lthe ight interferometry for a unlubricated condition

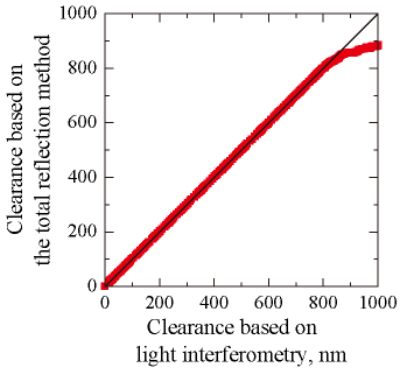

(e) Relationship between clearance calculated from intensity in the total reflection method and the light interferometry.

Fig. 8.1 Summarized results for Chapter 2.

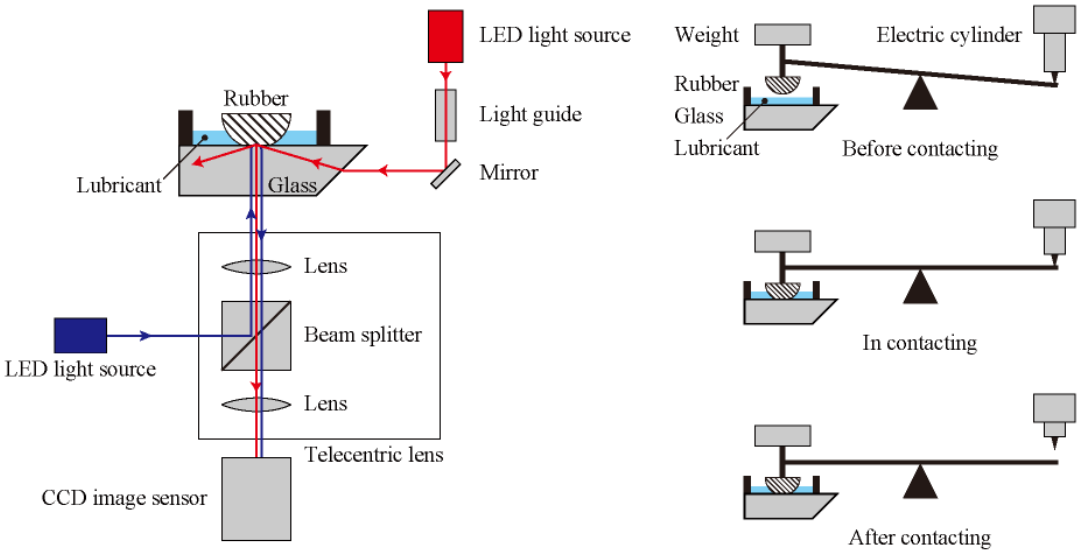

(a) Schematic of the system for ovserving the interfece between a rubber hemisphere and a glass plate and the system for contacting the rubber hemisphere to the glass plate surface.

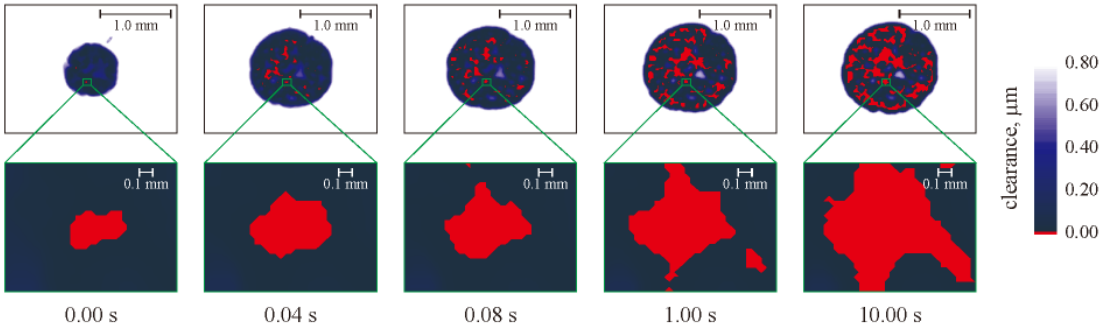

(b) Time dependency of the distributions of real contact and clearance between a rubber hemisphere and a glass plate.

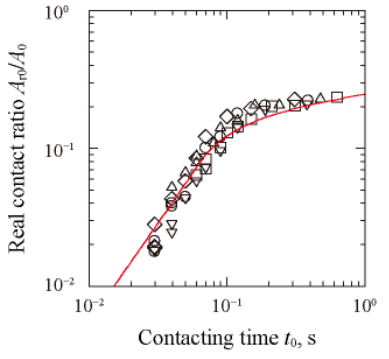

(c) Influence of the contacting time on measured and estimated real contact rate

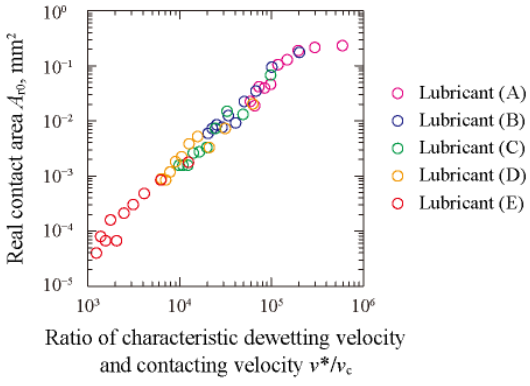

(d) Real contact area plotted against the ratio of characteristic dewetting velocity and contacting velocity,

Fig. 8.2 Summarized results for Chapter 3.

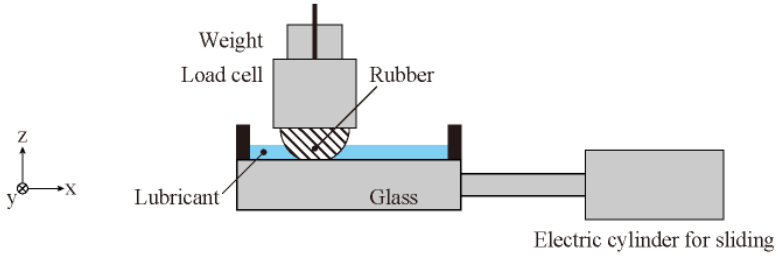

(a) Achematic view of the mechanical system for sliding.

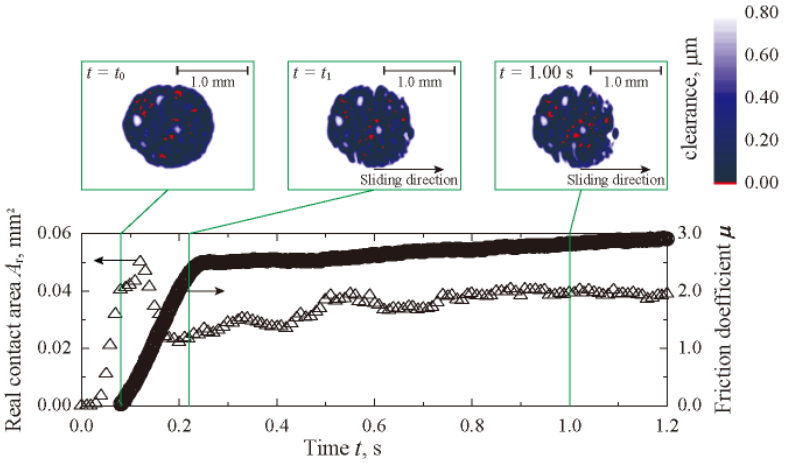

(b) Time dependency of contact condition, real contact area, and friction coefficient during the processes of contacting and sliding between the rubber hemisphere and the glass plate. $t = t_0$ corresponded to the completion time for contacting process, and $t = t_1$ was defined as the phase when the rubber hemisphere was about to slide.

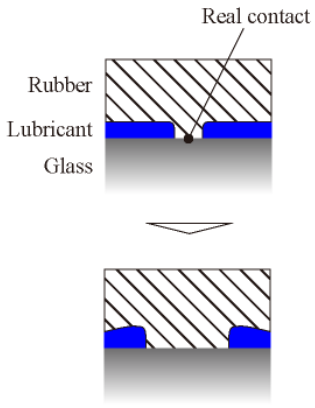

(c) Schematic view of dewetting behavior between rubber and glass associated with increased real contact area.

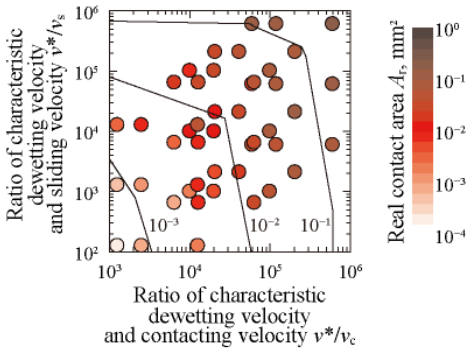

(d) Influence of ratio of characteristic dewetting velocity and sliding velocity and ratio of characteristic dewetting velocity and contacting velocity on real contact area when the rubber hemisphere was about to slide.

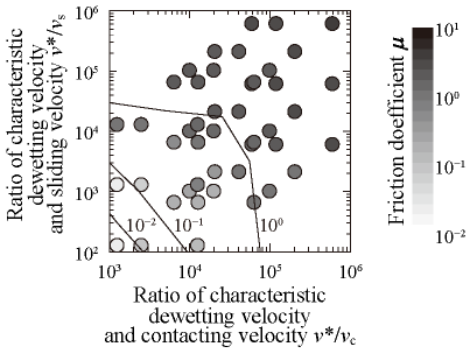

(e) Influence of ratio of characteristic dewetting velocity and sliding velocity and ratio of characteristic dewetting velocity and contacting velocity on friction coefficient when the rubber hemisphere was about to slide.

Fig. 8.3 Summarized results for Chapter 4.

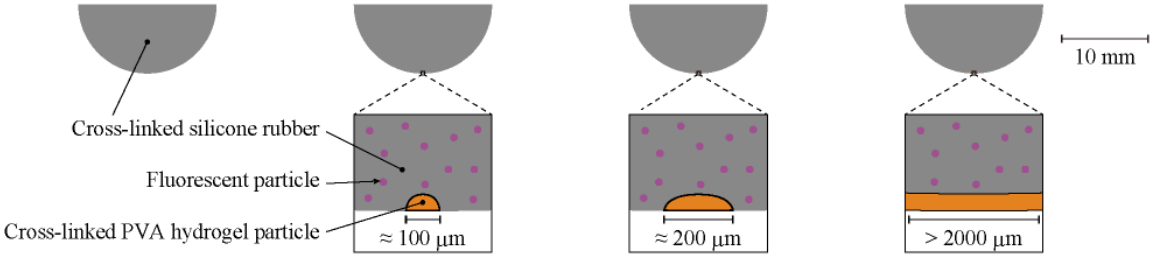

(a) Rubber without hydrogel. (b) Rubber with hydrogel #1. (c) Rubber with hydrogel #2. (d) Rubber with hydrogel #3.

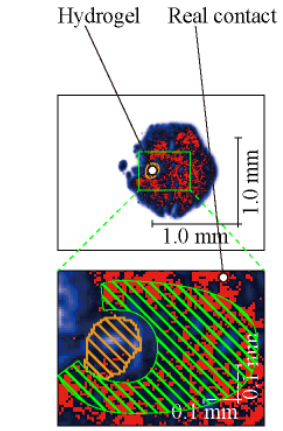

(e) Distributions of real contacts, water, air, and hydrogel in friction of rubber hemisphere with an hydrogel patch #1 for an water-lubricated condition.

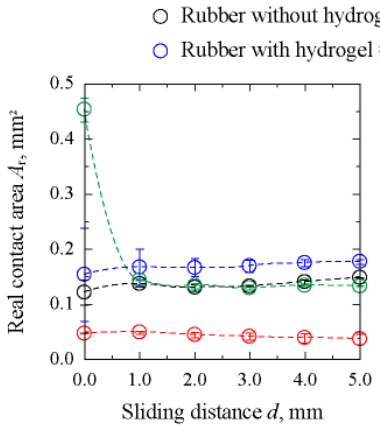

(f) Real contact area during friction of rubber hemispheres for a water-lubricated conditions plotted against sliding distance.

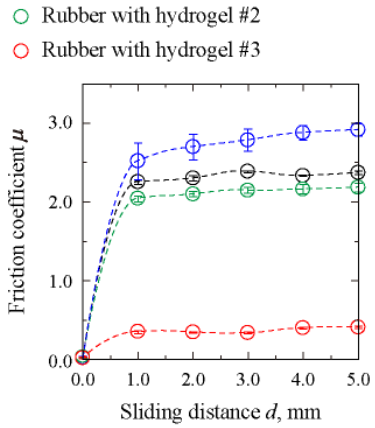

(g) Change in friction coefficient in friction of eubber hemispheres for a water-lubricated condition.

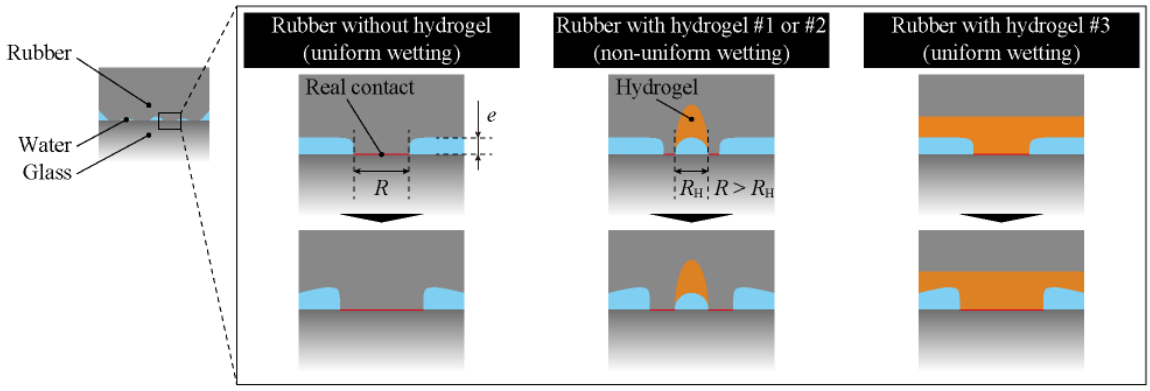

(h) Dewetting behaviors models for uniform and nonuniform wettability distributions. Rubber without a hydrogel and with hydrogel #3 demonstrate uniform wetting, while rubbers withhydrogel #1 and #2, nonunifrom wetting.

Fig. 8.4 Summarized results for Chapter 5.

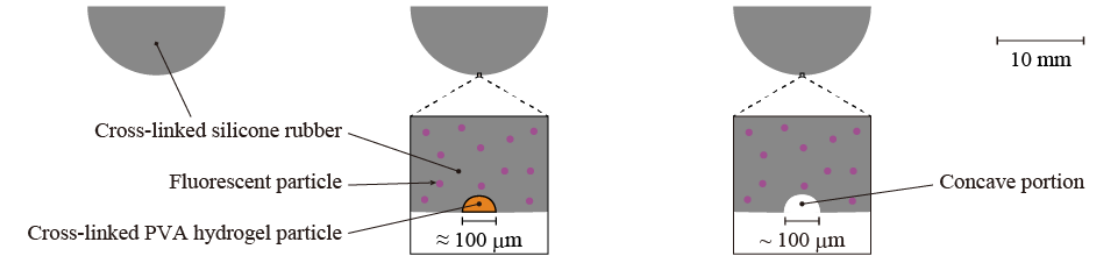

(a) Schematic view of hemisphere of untreasted rubber.

(b) Schematic view of hemisphere of rubber with a hydrogel patch.

(c) Schematic view of hemisphere of rubber with an air pocket.

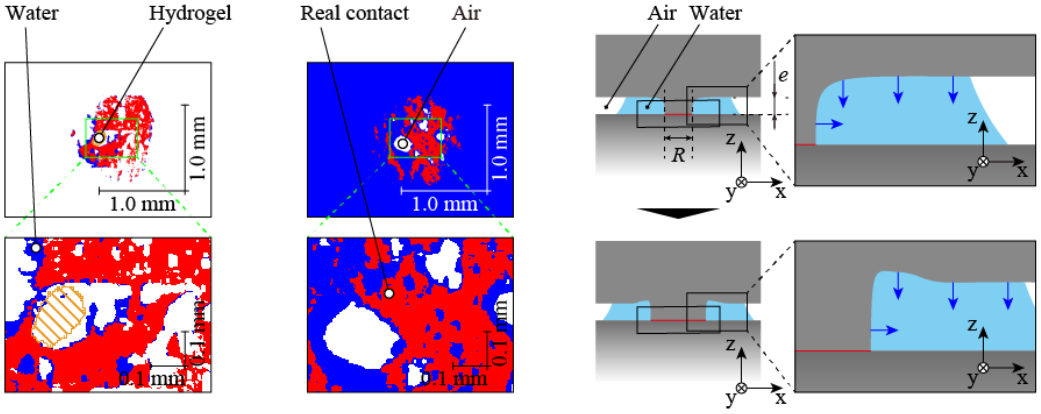

(d) Distributions of real contacts, water, air, and hydrogel in friction of rubber hemisphere with an hydrogel patch (moist) for an unlubricated condition.

(e) Distributions of real contacts, water, and air in friction of rubber hemisphere with an air pocket for a water-libricated condition.

(f) Schematic of real contact formation based on the dewetting behavior for real contact with a water meniscus.

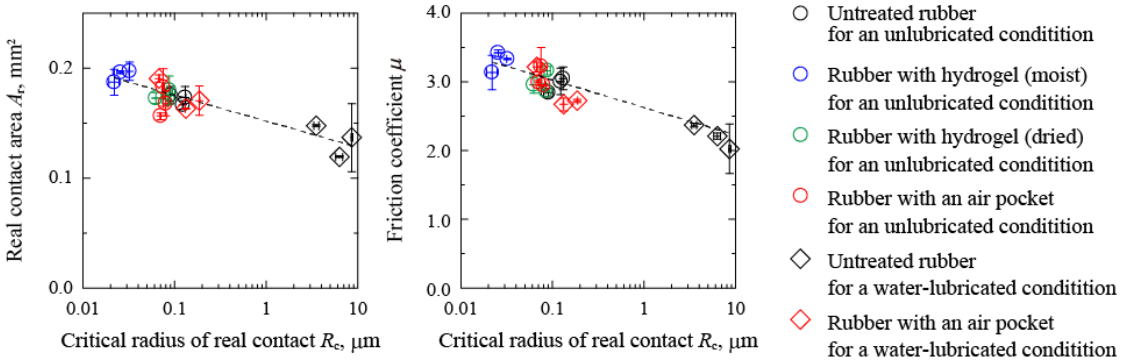

(g) Real contact area during friction of rubber hemisphere for unlubricated and water-lubricated conditions plotted against critical radius of real contact.

(h) Influence of critical radius of real contact on friction coefficient during friction of rubber hemispheres for unlubricated and water-lubricated condition.

Fig. 8.5 Summarized results for Chapter 6.

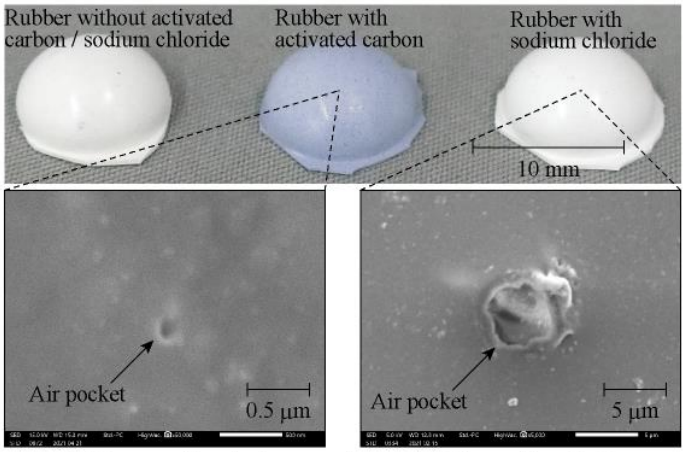

(a) Images of hemisphere specimens of rubbers without/with activated carbon or sodium chloride.

(b) Images of shoes with outer-soles of rubber without activated carbon or sodium chloride.

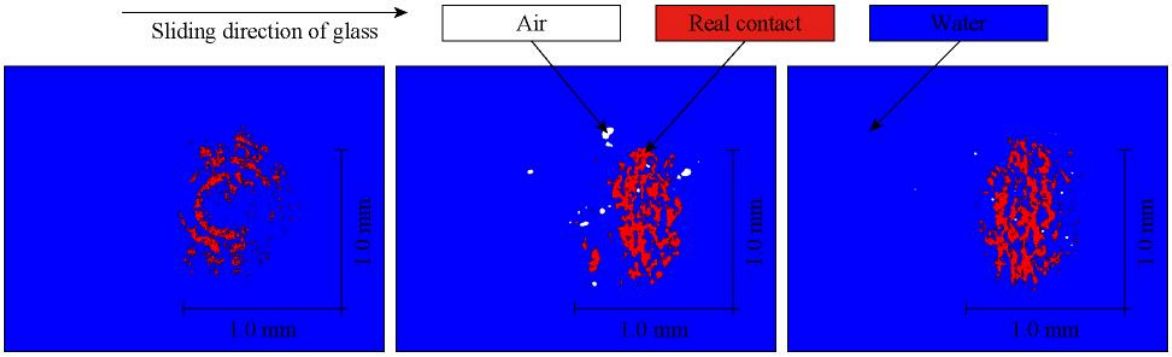

(c) Ditributions of real contacts and water during friction of hemisphere specimen of rubber without activated carbon and sodium chloride.

(d) Ditributions of real contacts, air, and water during friction of hemisphere specimen of rubber with activated carbon.

(e) Ditributions of real contacts, air, and water during friction of hemisphere specimen of rubber with sodium chloride.

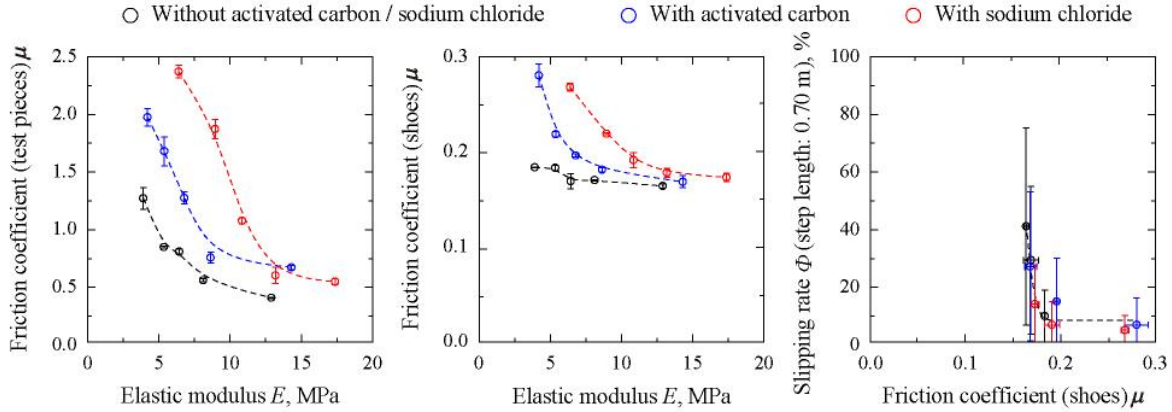

(f) Influence of elastic modulus on friction coefficient of hemisphere specimen of rubber without/with activated carbon and sodium chloride.

(g) Influence of elastic modulus on friction coefficient of outer-soles of rubber without/with activated carbon and sodium chloride.

(h) Relationship between slip rate in step motion for 0.70 m and friction coefficient of outer-soles without/with activated carbon and sodium chloride.

Fig. 8.6 Summarized results for Chapter 7.

Acknowledgements

I would like to express my sincere appreciation to my academic advisor, Prof. Kazuo Hokkirigawa, for his thoughtful kindness, excellent guidance and constant encouragement throughout this work.

I would also like to thank Prof. Hitoshi Soyama, Prof. Tsunemoto Kuriyagawa, and Prof. Kazuhiro Ogawa for their careful review, valuable suggestions and participation in this research work as members of the examination committee.

I would like to gratefully acknowledge the enthusiastic supervision of Associate Prof. Takeshi Yamaguchi during my research work.

I would also like to specially thank Dr. Kei Shibata, for the constant help and tremendous assistance with this work.

This thesis summarizes the research which I have accomplished in ASICS Corporation since 2011 and in Tohoku University since 2019.

This research was supported by ASICS Corporation. I would also like to thank Mr. Kenichi Harano and Dr. Junichiro Tateishi for sufficient supports.

I am grateful to each member of our laboratory with whom I have had the pleasure to study together for their kind assistance.

Finally, I am grateful to my parents for support and understanding, and to my wife, Mai, and my daughters, Yuna and Ayaka, for support, understanding, endless patience and encouragement.